Monte Carlo Simulations of Magnetism in $LiNiPO_4$

by

Kine Ødegård Hanssen

THESIS

for the degree of

MASTER OF SCIENCE

Faculty of Mathematics and Natural Sciences
University of Oslo

December 2017

Abstract

$LiNiPO_4$ belongs to a group of materials that show interesting magnetoelectric properties, among others a commensurate-incommensurate (C-I) magnetic phase transition. To investigate this, we perform Monte Carlo simulations on suggested models of $LiNiPO_4$. In order to identify the phase, the ordering wave vector $\mathbf{q}$ is studied. We do not find the C-I phase transition from the models, but instead observe an antiferromagnetic-paramagnetic (AF-PM) one for two of the models and an incommensurate-paramagnetic one for the other. The critical temperature for the AF-PM phase transition is found using the finite size scaling of Binder cumulant crossings and the location of the peak of the magnetic susceptibility. The critical exponents ν, γ and α will be found through the finite size scaling analysis for one of the models. Through an analytical approach, we find a condition for the incommensurate state to be the ground state. Analyzing our numerical output, we find that models that deviate slightly from the given ones exhibit an incommensurate phase, but none of these possess the commensurate-incommensurate phase transition.

In loving memory of
Dag Magnus Hanssen
1954-1997
Beloved uncle
and the first physicist I ever knew

Acknowledgements

First and foremost, I would like to thank my supervisor Olav Syljuåsen for his guidance and insights.

A special thanks goes to my office mates August Geelmuyden and Ingrid Holm for helpful discussions and good company, and to Birgitte Madsen for her invaluable friendship. I would also like to extend my thanks to the entire theory section for words of encouragement, fun lunch-time conversations and the occasional social event.

Last, but not least, I would like to thank my family for their love and support. They have always been so kind to me, and I could ask of nothing more.

Contents

Chapter 1

Introduction

In recent years, there has been a growing interest in a group of crystals called litium orthophosphates or just lithium phosphates. These crystals have the chemical composition of LiMPO$_4$, where M denotes the transition metals, i.e. Co, Ni, Mn, Fe, Cu. The lithium phosphates belong to a group of materials showing some exceptional magnetic properties. LiNiPO$_4$ and LiFePO$_4$ has gotten particular interest since they have been suggested as cathodes for lithium batteries [12].

The magnetic ions of LiNiPO$_4$ are Ni^{2+}, which have spin one. A reasonable approximation is considering the Ni^{+2}-ions as classical spins of unit length on a particular three-dimensional lattice. At low temperatures, neighbouring spins are shown to be antiparallel, which is a commensurate ordering. As the temperature is increased, however, the system enter the incommensurate phase. The spins are still ordered, but in a rotated pattern. Roughly speaking, there is a general, fixed angle $\theta \neq \pi n$ between each pair of spin neighbours. In a work by Toft-Petersen et. al. [26] LiFePO$_4$ was found not exhibit an incommensurate phase, which is the reason for our sole focus on LiNiPO$_4$.

Figure (1.1) shows the results of a scattering experiment performed by Vaknin et. al.[7]. We will focus on the left-hand side of the figure. The measured intensity is plotted against (0,K,0), where K is connected to the ordering angle θ in the y-direction of the crystal. At low temperature, T$=$ 9.81 K, there is only one peak present, situated at $(0, 1, 0)$ and corresponding to the antiparallel ordering. At higher temperature, two other peaks occur, and these are associated with the incommensurate phase. They appear at T$=$ 20.805 at $(0, 1 \pm \delta, 0)$ and die away in the paramagnetic phase due to thermal fluctuations. The plot informs us that the incommensurate phase only occurs in a small temperature interval. In fact, it is only present for a temperature range of about 1 K[12].

In this thesis, we simulate LiNiPO$_4$ in order to determine its magnetic properties. To do that, we use proposed models of LiNiPO$_4$ from a set of papers[13],[15],[25] and use them in Monte Carlo simulations. From these, we obtain macroscopic variables such as the energy and the magnetization. We will make extended use of the spin correlation function and the Binder cumulant, which will be introduced in Chapter 2. Using the Bootstrap method, described in Appendix A.3, we obtain critical exponents and error estimates for the model of [13] and compare to 3D Ising and Heisenberg models.

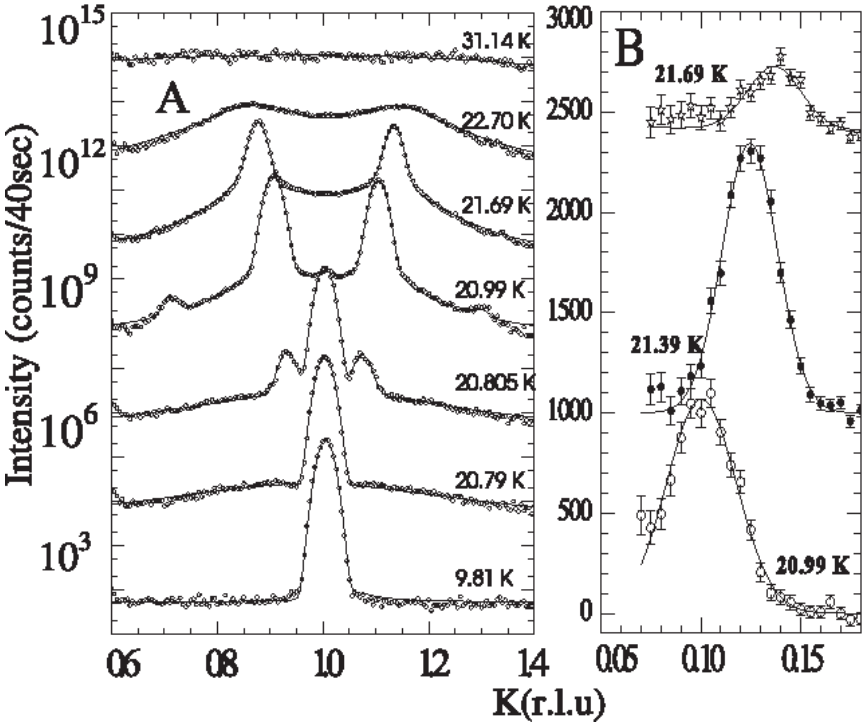

Figure 1.1: A figure from [7], showing the result of their scattering experiment. The intensity is plotted against (0,*K*,0), where *K* signifies the order in the y-direction of the crystal. The plot to the left shows a peak at (0,1,0) for temperatures up to 20.805 K. At 20.805 K, two additional peaks appear. They move further and further away from (0,1,0) before they die away at about 22.7 K. The intensity of the scans are shifted for clarity.

1.1 Outline

Chapter 2 provides the essential background information to understand this thesis. It starts off by introducing phase transitions, order parameters and finite size scaling in general. Later on, it states the order parameters specific to our thesis. Useful quantities such as the Binder cumulant will also be introduced. Chapter 3 will give the couplings of the models by [13], [15] and [25].

Chapter 4 provides a neccessary background to the rest of the thesis, that is based more heavily on calculations than the theory in Chapter 2. It briefly states the effect of the different terms, as derived by use of the spiralization condition on a chain in Appendix C. Moving on, it gives the ordering wave vector signaling antiferromagnetic ordering for the chain and the fcc.

Chapter 5 shows the plots of the spin correlation function. This chapter provides useful information on the phases present in the system. Plots of a few modified versions of [13] are also included.

In chapter 6, we find the ground state of the face-centered cubic lattice with ordering in the y-direction. Thus, we find a condition for the system to be in the incommensurate phase, though only strictly valid at zero temperature. We test the models against this condition.

Chapter 7 gives the result of the finite size scaling method. The finite size scaling of crossing points is derived in Appendix F, but left out of the main part of the thesis for readability. Through the finite size scaling, we find critical exponents, the critical temperatures and the critical Binder cumulant. We compare with known results and try to pinpoint the universality class of [13].

Chapter 8 presents a modification of the model of Jensen et. al. that should have an incommensurate-paramagnetic phase transition at 21.8 K. The detailed derivation is left to Appendix G.

In Chapter 9, we discuss the models. Chapter 10 contains the conclusion and outlook.

Chapter 2

General theoretical background

2.1 Classical spins

We mentioned in the introduction that the Ni^{2+}-ions have spin one. Spins of length one are obviously quantized, and one could wonder if such a small spin shouldn't be modeled as such. Quantum Monte Carlo algorithms have been developed, but these are pretty specialized and not applicable to all problems of quantum statistical mechanics[14], such as ours. Working with classical spins simplifies our calculations considerably, and though there are quantum fluctuations at play, we expect them to be small.

2.2 Concepts from statistical mechanics

2.2.1 Thermodynamic potentials and ensembles

We remind that the first law of thermodynamics for a fixed particle number reads

$$dU = TdS - PdV \tag{2.1}$$

where U is the internal energy of the system and is called a thermodynamic potential. It is constant at fixed entropy S and volume V. When S, V and the particle number N are fixed, our system is in the **microcanonical ensemble**.

We do not keep the entropy fixed, however, but rather the temperature. We can perform a Legendre transformation to obtain another thermodynamic potential, namely the Helmholtz free energy $F = U - TS$

$$dF = -SdT - PdV \tag{2.2}$$

From Eq. (2.2) we see that F is constant for fixed T and V. When we keep T, V and N fixed, as we do in our simulations, our system is in the **canonical ensemble**.

2.2.2 The partition function

The discrete canonical partition function is defined as

$$Z(\beta) = \sum_i e^{-\beta E_i} \tag{2.3}$$

Where E_i is the energy of state i. The partition function is a measure of the number of possible configurations of the system, with each possible state being weighted by its Boltzmann factor, $\exp(-\beta E_i)$, which is proportional to its probability p_i[20]

$$p_i = \frac{1}{Z} e^{-\beta E_i} \tag{2.4}$$

which is also called the Boltzmann probability. A set of states obeying Eq. (2.4) are said to obey the Boltzmann distribution. In a way, the partition function is a normalization constant of the states. The partition function is useful when deriving macroscopic observables. Since we are considering a system of continuous spins, we must use the continuous version

$$Z = \int d\mathbf{S}_0 \cdots d\mathbf{S}_f e^{-\beta H(\mathbf{S}_0, \cdots \mathbf{S}_f)} \tag{2.5}$$

which is set up to a normalization constant. The partition function is related to the free energy by $Z = e^{\beta F}$. In this thesis, the partition function will mainly be used to verify the code, like in Appendix B.

Any average of A may be expressed as

$$\langle A \rangle = \frac{1}{Z} \sum_i A_i e^{-\beta E_i} \tag{2.6}$$

with discrete variables or

$$\langle A \rangle = \frac{1}{Z} \int d\mathbf{S}_0 \cdots d\mathbf{S}_f A(\mathbf{S}_0, \cdots \mathbf{S}_f) e^{-\beta H(\mathbf{S}_0, \cdots \mathbf{S}_f)} \tag{2.7}$$

with our continuous ones. Actually using Eq. (2.7) to find $\langle A \rangle$ would be ridiculously time-consuming, which is why we apply the Metropolis algorithm instead. Monte Carlo methods and the Metropolis algorithm are discussed in Appendix A.1.

From either version of $\langle A \rangle$, it follows that the average energy of the system is related to the partition function by

$$\langle E \rangle = -\frac{1}{Z} \frac{\partial Z}{\partial \beta} \qquad \text{or} \qquad \langle E \rangle = -\frac{\partial}{\partial \beta} \ln(Z) \tag{2.8}$$

The heat capacity at constant volume is in turn related to the energy by

$$C_V = -k\beta^2 \frac{\partial}{\partial \beta} \langle E \rangle \tag{2.9}$$

which can also be expressed as

$$C_V = k_B\beta^2\left(\langle E^2\rangle - \langle E\rangle^2\right) \tag{2.10}$$

We often look at the heat capacity per particle, $c_V = C_V/N$, which is also called the specific heat capacity or just the specific heat. The heat capacity is related to F by [6]

$$C_V = -T\left(\frac{\partial^F}{\partial T}\right)_V \tag{2.11}$$

Of course, there are quantities of interest other than those derived from the energy. The uniform magnetization per spin in a given direction $\alpha = x, y, z$ is

$$m_\alpha = \frac{1}{N}\sum_i S_i^\alpha \tag{2.12}$$

So it measures the average spin component in direction α. It is related to the Helmholtz free energy by

$$m_\alpha = \left(\frac{\partial F}{\partial B_\alpha}\right) \tag{2.13}$$

From the magnetization we find the magnetic susceptibility per spin by [17]

$$\chi_\alpha = \beta N\left(\langle m_\alpha^2\rangle - \langle m_\alpha\rangle^2\right) \tag{2.14}$$

which is related to the Helmholtz free energy by

$$\chi_\alpha = \beta N\left(\frac{\partial M_\alpha}{\partial B_\alpha}\right)_T = -N\left(\frac{\partial^2 F}{\partial B_\alpha^2}\right)_T \tag{2.15}$$

as can easily be shown.

2.2.3 Para-, ferro- and antiferromagnetism

Ferro- and antiferromagnetic phases are characterized by long-range order of the magnetic moments. In the ground state of a ferromagnet, spin neighbours are parallel, and the uniform magnetization per spin will be maximal. In the antiferromagnetic ground state, all spin neighbours are antiparallel. Therefore, the spin components cancel and lead to zero macroscopic magnetization. Of course, as soon as the temperature is non-zero, thermal fluctuations will appear, and the spin neighbours will no longer be purely parallel or antiparallel. At sufficiently high temperature, the preferred order is lost, and the magnetization will be zero. The system is then said to be in the paramagnetic phase. Like the ferro- and antiferromagnetic phases, the paramagnetic phase has a positive susceptibility. This can be used to distinguish it from the diamagnetic phase, which has negative susceptibility [18].

2.2.4 Hamiltonians for ferro- and antiferromagnetism

The Ising Hamiltonian reads

$$H_{Ising} = J \sum_{\langle ij \rangle} S_i S_j \tag{2.16}$$

Where $S_i = \pm 1$ and $\langle ij \rangle$ denotes pairs of nearest neighbours i and j. The continuous, anisotropic Heisenberg model takes a similar form

$$H_{Heisenberg} = \sum_{\langle ij \rangle} J_{ij} \mathbf{S}_i \cdot \mathbf{S}_j \tag{2.17}$$

$J, J_{ij} > 0$ describes an antiferromagnetic system while $J, J_{ij} < 0$ describes a ferromagnetic one. If the Hamiltonians were to be defined with a minus sign, the opposite would be the case.

2.2.5 Phase transitions and finite size scaling

Phase transitions

A quantity A of a system may vary with the temperature in different ways. For a lot of systems, there is an A that is zero above some temperature T_c and non-zero below it. The system is then said to exhibit a **phase transition**. When A behaves the way we just described, it is called an **order parameter** of the system[6]. A phase might have several order parameters, and we are fairly free to choose one. Apart from the change in the order parameter, there might be diverging quantities at the phase transition. For a lot of magnetic phase transitions, such as the ferromagnetic-paramagnetic one, the magnetic susceptibility and specific heat diverge [17].

A phase transition can be further separated into continuous phase transitions and discontinuous or first order phase transitions. The order parameter A changes discontinuously at T_c for **discontinuous phase transitions**, while it changes continuously at T_c for a **continuous phase transition** [27]. For discontinuous phase transitions, the first derivatives of the free energy, such as m, are discontinuous at T_c , hence the term[6]. For continuous phase transitions, the first derivatives of the free energy are continuous, while second derivatives such as χ and c_V diverge at T_c [27]. The ferromagnetic-paramagnetic phase transition is continuous [17], while the C-I phase transition is discontinuous for $LiNiPO_4$ [15].

The **critical exponents** of a system dictates how quantities such as c_V and χ behave as we approach the continuous transition[6]. It turns out that the critical exponents are not sensitive to details such as the lattice structure and the magnitudes of the couplings, but they do depend on the dimensionality of the lattice and the symmetry of the order parameter. We say that models that share the same critical exponents belong to the same **universality class** [17].

Finite size scaling

When we do simulations, our system will always have a limited size. This will dampen the effects described in the previous subchapter, such as the abrupt change in the order parameter or the diverging magnetic susceptibility and specific heat at continuous transitions. Instead, χ and c_V will have peaks of finite size near the critical value[17]. Of course, the larger the system, the closer we should get to the behaviour in the thermodynamic limit. For that reason, we would expect the diverging quantities to scale with the system size L, and that is indeed the case. This scaling is usually through a power law, i.e. $\Gamma \propto L^{-p}$, where Γ is the diverging quantity and p is an exponent unique to Γ [6].

Finite size scaling is not limited to diverging quantities, however. There are quantites that do not have a peak when plotted against temperature, but still change shape as we increase the system size L. For some of them, we can obtain an estimate of the critical temperature by finding the crossing-points of graphs of different L's.

2.3 Frustration

Frustration occurs when the bonds of a system favour different orderings. This can happen due to competing interactions, periodic boundary conditions or the structure of the lattice.

2.4 Commensurate and incommensurate phases

Commensurate and incommensurate phases are both ordered phases. To take a chain of continuous spins as an example, moving from site to site, the spins rotate with a fixed angle θ for both phases. In the commensurate phase, θ/π is a rational number, so that it takes a sites for the spins to have rotated b whole periods. For the incommensurate phase, θ/π is an irrational number, so that there is no number of sites a for which the spins have rotated a whole number of periods. The magnetic ordering wave vector is related to the angle θ, so we can tell whether or not the system is in the incommensurate phase by looking at the magnetic ordering vector and the order parameter, like we did with figure (1.1). The concept of commensurability and incomensurability generalize to multidimensional systems and quantities other than the spin, such as charge density or electric polarization [21].

In experiments, it might be difficult to distinguish between incommensurate phases and commensurate phases with long periods due to limited resolution of the measurements [21]. Simulations being a sort of experiment, this is something we ourselves must take into account. We have limited resolution on our $\mathbf{q}$-vectors and thus cannot say with certainty that the phase we have detected is truly incommensurate. We can, however, determine if the angle of rotation is somewhere in between ferromagnetic ($\theta = 0$) and antiferromagnetic ($\theta = \pi$). If θ/π is a fraction, we will say that the system is in the incommensurate phase, even though that may not be strictly true.

Incommensurate phases typically arise in models with competing interactions [3]. If these interactions favour different commensurate orderings, an incommensurate ordering might be energetically preferable, depending on the couplings. We might consider a chain of rotating spins with a nearest neighbour Heisenberg coupling J_1 and a next-nearest Heisenberg coupling J_2. With periodic boundary conditions, its energy is

$$E = J_1 \sum_i \mathbf{S}_i \cdot \mathbf{S}_{i+1} + J_2 \sum_i \mathbf{S}_i \cdot \mathbf{S}_{i+2} = N\left[J_1 \cos\theta + J_2 \cos\left(2\theta\right)\right] \tag{2.18}$$

which is minimized for the incommensurate ordering

$$\theta = \arccos\left(-\frac{J_1}{4J_2}\right) \qquad \text{when} \quad 4\left|J_1\right| < J_2, \quad J_2 > 0 \tag{2.19}$$

We prove that this is indeed the minima in Appendix E. Evidently, we can model incommensurate phases for $LiNiPO_4$ by generalizing this simple model to the face-centered cubic lattice, which we will discuss in section 2.9. All our proposed models [13], [15] and [25] actually include competing nearest- and next-nearest neigbour interactions.

2.5 Microscopic origin of the interactions

This section is meant as a motivation for the different terms in the Hamiltonians of [13], [15], [25]. The microscopic interactions that cause the different terms are briefly stated, and then the Hamiltonian for that interaction is given.

2.5.1 Heisenberg interactions

There are two mechanisms that may to Heisenberg terms: direct exchange and superexchange[12]. In $LiNiPO_4$, the **direct exchange** can be found by considering the potential energy between two magnetic Ni^{2+}-ions. Massaging the expression for the potential energy, one ends up with an ordinary Coulomb term and a term that accounts for Pauli's exclusion principle, the latter of which leads to a ferromagnetic interaction for this material[12].

The mechanism of **superexchange** occurs when an electron is transferred from one magnetic ion, A, to another, B, through a non-magnetic ion situated somewhere in between them. After the transfer, an electron moves from B to A[12]. Using perturbation theory, one can show that the superexchange accounts for both ferromagnetic and antiferromagnetic interactions.

For these two kinds of exchange interaction, we end up with terms on the form

$$H_{nn} = \sum_{\langle ij \rangle} J_{\langle ij \rangle} \mathbf{S}_i \cdot \mathbf{S}_j \tag{2.20}$$

where $\langle ij \rangle$ denotes nearest neighbours i, j and the sign of $J_{\langle ij \rangle}$ determines whether the system is ferromagnetic or antiferromagnetic. This is exactly the Hamiltonian we

listed in section 2.2.3. Jensen states that the Heisenberg terms for $LiNiPO_4$ are due to superexchange[12].

2.5.2 Single-ion anisotropy

The single-ion anisotropy arises from the spin-orbit coupling

$$H_{SO} = \lambda \mathbf{L} \cdot \mathbf{S} \tag{2.21}$$

where λ is a constant, $\mathbf{L}$ is the angular momentum and $\mathbf{S}$ is the spin[12]. The first-order term in perturbation theory vanishes, while the second-order term couples a spin to itself. For $LiNiPO_4$, we obtain the single-ion anisotropy [12]

$$H_{s.i.an.} = \sum_i \left[D^x_{\text{an}} \left(S^x_i\right)^2 + D^y_{\text{an}} \left(S^y_i\right)^2 + D^z_{\text{an}} \left(S^z_i\right)^2 \right] \tag{2.22}$$

2.5.3 The Dzyaloshinskii-Moriya interaction

The Dzyaloshinskii-Moriya interaction is sometimes referred to as **antisymmetric exchange**. Microscopically, it originates from an interplay between the spin-orbit coupling and the exchange interaction[12]. As with the single-ion anisotropy, it arises from second-order perturbation theory. It takes the form of

$$H_{DM} = \sum_{\langle ij \rangle} \mathbf{D}_{DM} \cdot \left(\mathbf{S}_i \times \mathbf{S}_j\right) \tag{2.23}$$

The Dzyaloshinskii-Moriya interaction is associated with spin canting, which is the rotation of spins with an angle θ away from the parallel or antiparallel ordering[25]. Spin canting has been observed in $LiNiPO_4$, which motivates the inclusion of the Dzyaloshinskii-Moriya term in the Hamiltonian[25].

2.5.4 The Hamiltonian

Including the next-nearest neighbour Heisenberg interaction proposed in [Ref to last chapter]

$$H_{nnn} = \sum_{\langle\langle ij \rangle\rangle} J_{\langle\langle ij \rangle\rangle} \mathbf{S}_i \cdot \mathbf{S}_j \tag{2.24}$$

The total Hamiltonian becomes

$$\begin{aligned} H = &\sum_{\langle ij \rangle} J_{\langle ij \rangle} \mathbf{S}_i \cdot \mathbf{S}_j + \sum_{\langle\langle ij \rangle\rangle} J_{\langle\langle ij \rangle\rangle} \mathbf{S}_i \cdot \mathbf{S}_j \\ &+ \sum_{\langle ij \rangle} \mathbf{D}_{DM} \cdot \left(\mathbf{S}_i \times \mathbf{S}_j\right) + \sum_i \left[D^x_{\text{an}} \left(S^x_i\right)^2 + D^y_{\text{an}} \left(S^y_i\right)^2 + D^z_{\text{an}} \left(S^z_i\right)^2 \right] \end{aligned} \tag{2.25}$$

2.6 Bravais lattices

Bravais lattices are grid structures where all points are equivalent, i.e. if we move from one point to another on the lattice, the surroundings will look the same. Any site on the Bravais lattice can be found by a linear combination of what is called the **primitive unit vectors** $\mathbf{a}_i$ of the lattice. These are neither parallel nor residing in the same plane. In three dimensions, the position of a site is given by [11]

$$\mathbf{R} = n_1\mathbf{a}_1 + n_2\mathbf{a}_2 + n_3\mathbf{a}_3 \tag{2.26}$$

where the indices n_1, n_2 and n_3 are integers. The exact form of the $\mathbf{a}_i$'s depends on the lattice. There are several types of Bravais lattices. They can be sorted according to their primitive unit cell, i.e. the cell which only have sites at its corners. For instance, the primitive cubic unit cell is exactly that, a cube. The primitive orthorhombic unit cell also have corners of 90°, but the length of the sides are all different [11].

There are three kinds of cubic Bravais lattices: The primitive, the body-centered and the face-centered cubic lattice. The body-centered lattice has a site in the middle of the unit cell, while the face-centered unit cell has one site at the middle of each face. Orthorhombic systems can also have body-centered and phase-centered unit cells. The magnetic unit cell of $LiNiPO_4$ is in fact face-centered orthorhombic, but we chose to consider the face-centered cubic lattice and adjust the couplings instead.

2.6.1 The reciprocal lattice

Each Bravais lattice has a reciprocal lattice, which resides in momentum space rather than in real space. The sites of the reciprocal lattice can also be given by a vector, which we will denote by $\mathbf{q}$. The $\mathbf{q}$'s are the wave vectors of a planar wave $e^{i\mathbf{q}\cdot\mathbf{r}}$ with the same periodicity as the lattice. We can use this to find the primitive unit vectors $\mathbf{b}_i$ of the reciprocal lattice [11]. Enforcing said periodicity yields a constraint

$$e^{i\mathbf{q}\cdot(\mathbf{R}+\mathbf{r})} = e^{i\mathbf{q}\cdot\mathbf{r}} \quad \forall \quad \mathbf{r},\ \mathbf{R} \qquad \rightarrow \qquad e^{i\mathbf{q}\cdot\mathbf{R}} = 1 \tag{2.27}$$

where $\mathbf{R}$ is given by Eq. (2.26). Consequently, $\mathbf{q}$ must be orthogonal to $\mathbf{R}$. This offers a way to find the $\mathbf{b}_i$'s of the reciprocal lattice: We take the cross product between the primitive unit vectors $\mathbf{a}_i$ to get orthogonal vectors, and multiply with the appropriate factor. The $\mathbf{b}_i$'s are as follows[11]

$$\begin{aligned}
\mathbf{b}_1 &= \tfrac{2\pi}{v_E}(\mathbf{a}_2 \times \mathbf{a}_3) \\
\mathbf{b}_2 &= \tfrac{2\pi}{v_E}(\mathbf{a}_3 \times \mathbf{a}_1) \\
\mathbf{b}_3 &= \tfrac{2\pi}{v_E}(\mathbf{a}_1 \times \mathbf{a}_2)
\end{aligned} \tag{2.28}$$

with $v_E = \mathbf{a}_1 \cdot (\mathbf{a}_2 \times \mathbf{a}_3)$. This is in fact the volume of the unit cell of the Bravais lattice [11]. It is straightforward to show that

$$\mathbf{a}_i \cdot \mathbf{b}_j = 2\pi\delta_{ij} \tag{2.29}$$

Using a similar notation to that of $\mathbf{R}$, we can express any site on the reciprocal lattice as

$$\mathbf{q} = k_1\mathbf{b}_1 + k_2\mathbf{b}_2 + k_3\mathbf{b}_3; \qquad k_i \in \mathbb{Z} \tag{2.30}$$

Inserting into $e^{i\mathbf{q}\cdot\mathbf{R}}$ proves that the k_i's are indeed integers, just as the n_i's were for the Bravais lattice. It turns out that the reciprocal lattice of the reciprocal lattice is the Bravais lattice we started out with. In other words, the reciprocal lattice and the Bravais lattice take each other as their reciprocal lattice. This can be shown by insertion into another condition on the form of Eq. (2.27). Alternatively, we can say that the lattices are Fourier transforms of one another.

It is worthwhile to note that though the reciprocal lattice in most cases is of the same type as the original lattice, that is not the case for body-centered and face-centered lattices with an underlying cubic or orthorombic structure [11]. Instead, they take each other as reciprocal lattices, i.e. the face-centered cubic lattice has a reciprocal lattice which is body-centered cubic and vice versa. The same applies to orthorombic face-centered and body-centered lattices.

Further constraints on the momentum space indices

As we operate with a system of finite size, we can further constrain the momentum space indices in Eq. (2.30): Instead of only requiring the planar wave to be periodic with respect to translation from site to site in the lattice, we require it to be periodic with translations the size of the system length. This will change the coefficients in Eq. (2.30) We reserve k_i for integers and rename the coefficients of $\mathbf{b}_i$ to c_i. We define $\mathbf{L}_j = L_j\mathbf{a}_j$, where L_j is the size of the lattice in the direction of $\mathbf{a}_j$. Enforcing periodic boundary conditions on the reciprocal lattice, we have for any $\mathbf{R}$

$$e^{i\mathbf{q}\cdot(\mathbf{R}+\mathbf{L}_j)} = e^{i\mathbf{q}\cdot\mathbf{R}} \qquad \rightarrow \qquad e^{i\mathbf{q}\cdot\mathbf{L}_j} = 1$$

Combined with Eq. (2.29), each j yields the relation

$$e^{2\pi i c_j L_j} = 1 \;\rightarrow\; \cos(2\pi c_j L_j) = 1 \;\rightarrow\; 2\pi c_j L_j = 2\pi k_j \;\rightarrow\; c_j = \frac{k_j}{L_j} \tag{2.31}$$

with k_j being an integer. Applying this procedure in all directions, i.e. for $j = 1, 2, 3$ and inserting into (2.30) leads to

$$\mathbf{q} = \frac{k_1}{L_1}\mathbf{b}_1 + \frac{k_2}{L_2}\mathbf{b}_2 + \frac{k_3}{L_3}\mathbf{b}_3 \tag{2.32}$$

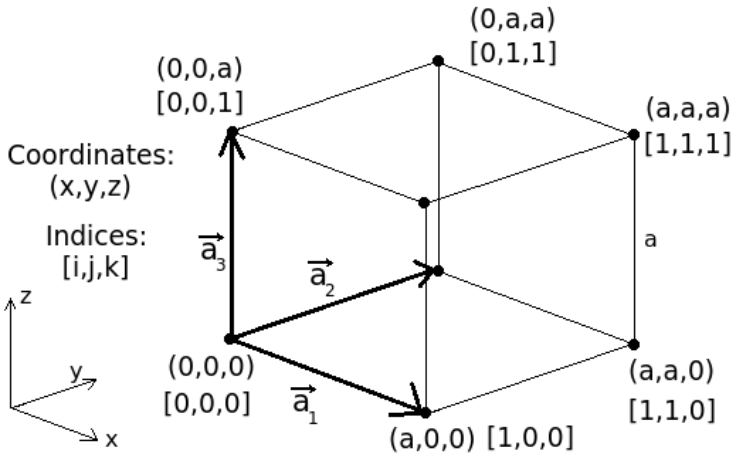

Figure 2.1: The unit cell of the simple cubic lattice. $\mathbf{a}_1$, $\mathbf{a}_2$ and $\mathbf{a}_3$ are the primitive unit vectors and a is the length of the sides. The coordinates (x,y,z) and indices [i,j,k] of some of the sites are given.

2.6.2 The primitive cubic lattice

The primitive or simple cubic lattice is a three-dimensional lattice with only right angles and each side of the unit cell being of equal length. Imagining a cube, there is one site at each corner, as seen in fig (2.1). The primitive vectors coincide with the Carthesian unit vectors, i.e. $\mathbf{a}_1, \mathbf{a}_2, \mathbf{a}_3 = a\hat{x}, a\hat{y}, a\hat{z}$, where a is the grid length.

2.6.3 The face-centered cubic lattice

The face-centered cubic lattice (fcc) has a cubic structure with one site at each corner, just as the primitive cubic lattice, but the fcc has an additional site at the middle of each face. An illustration is given in figure (2.2). These sites have half-integer coordinates, so the primitive unit vectors of the fcc are slightly more complicated than those of the simple cubic lattice. The unit vectors are

$$\mathbf{a}_1 = \frac{a}{2}(1,1,0); \quad \mathbf{a}_2 = \frac{a}{2}(0,1,1); \quad \mathbf{a}_3 = \frac{a}{2}(1,0,1) \tag{2.33}$$

where a is once again the length of the sides of the unit cell. Any site on the face-centered cubic lattice can be expressed by Eq. (2.26) with these primitive unit vectors.

Consequently, the coordinates of a site are:

$$x = \frac{a}{2}(i+k); \quad y = \frac{a}{2}(i+j); \quad z = \frac{a}{2}(j+k) \tag{2.34}$$

where i, j, k are the indices of the site. The unit cell of the face-centered cubic cell is shown in Fig. (2.2). Each site of the lattice has twelve nearest neighbours.

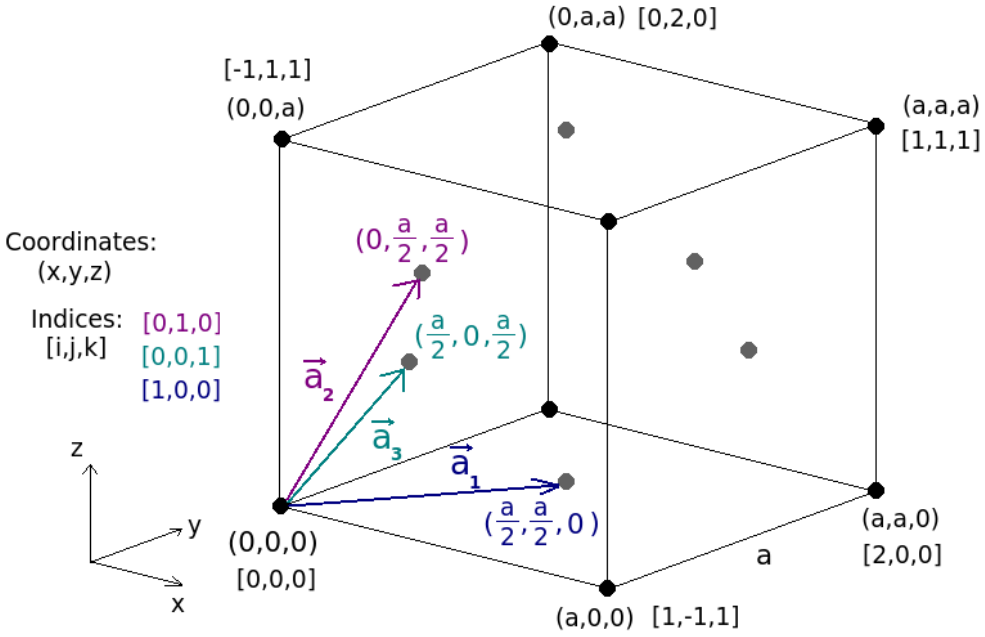

Figure 2.2: The unit cell of the face-centered cubic lattice. $\mathbf{a}_1$, $\mathbf{a}_2$ and $\mathbf{a}_3$ are the primitive unit vectors and a is the length of the sides. The coordinates (x,y,z) and indices [i,j,k] of some of the sites are given.

The reciprocal lattice

Doing the cross-products of Eq. (2.28) for the face-centered cubic lattice, we obtain:

$$\begin{aligned} \mathbf{b}_1 &= \tfrac{2\pi}{a}(1,1,-1) \\ \mathbf{b}_2 &= \tfrac{2\pi}{a}(-1,1,1) \\ \mathbf{b}_3 &= \tfrac{2\pi}{a}(1,-1,1) \end{aligned} \tag{2.35}$$

It is straightforward to show that these vectors indeed satisfy the relation $\mathbf{b}_i \cdot \mathbf{a}_j = 2\pi\delta_{ij}$. The components of $\mathbf{q}$ are given by

$$q_x = \frac{2\pi}{a}\left(\frac{k_1}{L_1} - \frac{k_2}{L_2} + \frac{k_3}{L_3}\right) \tag{2.36}$$

$$q_y = \frac{2\pi}{a}\left(\frac{k_1}{L_1} + \frac{k_2}{L_2} - \frac{k_3}{L_3}\right) \tag{2.37}$$

$$q_z = \frac{2\pi}{a}\left(-\frac{k_1}{L_1} + \frac{k_2}{L_2} + \frac{k_3}{L_3}\right) \tag{2.38}$$

2.7 Fourier transforms and the spin correlation function

2.7.1 Fourier transform

As the Bravais lattice and the reciprocal lattice are Fourier transforms of each other, we will make plenty of use of the Fourier transformed spins. The Fourier transform of a spin component is

$$S^{\alpha}_{\mathbf{q}} = \frac{1}{N}\sum_{\mathbf{r}} S^{\alpha}_{\mathbf{r}} e^{-i\mathbf{q}\cdot\mathbf{r}} \tag{2.39}$$

where $\alpha = x, y, z$.

2.7.2 The spin correlation function

The spin-spin correlation function in momentum space, or spin correlation function for short, is denoted by $\langle S^{\alpha}_{-\mathbf{q}} S^{\alpha}_{\mathbf{q}} \rangle$, where $S^{\alpha}_{\mathbf{q}}$ is given by Eq. (2.39). Writing it out in full

$$\langle S^{\alpha}_{-\mathbf{q}} S^{\alpha}_{\mathbf{q}} \rangle = \frac{1}{N^2} \langle \sum_{\mathbf{r}} \sum_{\mathbf{r}'} S^{\alpha}_{\mathbf{r}'} S^{\alpha}_{\mathbf{r}} e^{i\mathbf{q}\cdot(\mathbf{r}'-\mathbf{r})} \rangle \tag{2.40}$$

This is just the Fourier transform of Eq. (3.5.7) in Chaikin & Lubensky [6], or the disconnected version of (3.5.1) i Newman & Barkema [17]. The spin correlation function is a useful property as we are interested in the periodicity $\mathbf{q}$ of our spins, which informs us whether the system is commensurate or incommensurate. If we plot the value of the spin correlation function as a function of $\mathbf{q}$, its maximum will be the most significant periodicity in our system.

Working with three-dimensional continuous spins, we will make frequent use of its vectorial counterpart

$$\langle \mathbf{S}_{-\mathbf{q}} \cdot \mathbf{S}_{\mathbf{q}} \rangle = \frac{1}{N^2} \langle \sum_{\mathbf{r}} \sum_{\mathbf{r}'} \mathbf{S}_{\mathbf{r}'} \cdot \mathbf{S}_{\mathbf{r}} e^{i\mathbf{q}\cdot(\mathbf{r}'-\mathbf{r})} \rangle \tag{2.41}$$

which is in fact just

$$\langle \mathbf{S}_{-\mathbf{q}} \cdot \mathbf{S}_{\mathbf{q}} \rangle = \sum_{\alpha=x,y,z} \langle S^{\alpha}_{-\mathbf{q}} S^{\alpha}_{\mathbf{q}} \rangle = \langle S^{x}_{-\mathbf{q}} S^{x}_{\mathbf{q}} \rangle + \langle S^{y}_{-\mathbf{q}} S^{y}_{\mathbf{q}} \rangle + \langle S^{z}_{-\mathbf{q}} S^{z}_{\mathbf{q}} \rangle$$

Finding $\langle S^{\alpha}_{-\mathbf{q}} S^{\alpha}_{\mathbf{q}} \rangle$ can be optimized by utilizing one of the many excellent Fast Fourier transforms out there. For this thesis, we have chosen FFTW, or "The Fastest Fourier Transform in the West" [9]. We let FFTW function compute (2.39), then find $\langle S^{\alpha}_{-\mathbf{q}} S^{\alpha}_{\mathbf{q}} \rangle$ by multiplying the result with its own complex conjugate since

$$S^{\alpha}_{-\mathbf{q}} = \frac{1}{N}\sum_{\mathbf{r}} S^{\alpha}_{\mathbf{r}} e^{i\mathbf{q}\cdot\mathbf{r}} = \left(\frac{1}{N}\sum_{\mathbf{r}} S^{\alpha}_{\mathbf{r}} e^{-i\mathbf{q}\cdot\mathbf{r}} \right)^{*} = \left(S^{\alpha}_{\mathbf{q}} \right)^{*} \tag{2.42}$$

Clearly, the elements of $\langle S^{\alpha}_{-\mathbf{q}} S^{\alpha}_{\mathbf{q}} \rangle$ are all real

$$\tilde{S}^{\alpha}_{-\mathbf{q}} \tilde{S}^{\alpha}_{\mathbf{q}} = \tilde{S}^{\alpha}_{\mathbf{q}} (\tilde{S}^{\alpha}_{\mathbf{q}})^* = |\tilde{S}^{\alpha}_{\mathbf{q}}|^2 \tag{2.43}$$

2.8 The ordering wave vector and the order parameter

The **ordering wave vector** $\mathbf{q} = \mathbf{Q}$ reflects the magnetic ordering of the system, and gives the periodicity of the spin rotation. So far, we have only defined the uniform magnetization of the system. It can easily be generalized to

$$m_{\alpha}(\mathbf{q}) = \frac{1}{N} \sum_{\mathbf{r}} S^{\alpha}_{\mathbf{r}} e^{i\mathbf{r}\cdot\mathbf{q}} \tag{2.44}$$

where $\mathbf{q}$ is a wave vector. We see that the uniform magnetization is just a special case of Eq. (2.44), namely $\mathbf{q} = \mathbf{0}$. If $\mathbf{q} = \mathbf{Q}$ is the ordering wave vector, Eq. (2.44) gives the **order parameter** of the system, described in section 2.2. However, we take the average over a representable collection of states. To avoid a cancellation of the different contributions, we operate with $\langle m^2_{\alpha}(\mathbf{Q}) \rangle$.

$\langle m^2_{\alpha}(\mathbf{q}) \rangle$ is in fact equal to the spin correlation function for $\mathbf{q}$, so the peak of the spin correlation function will be the value of the order parameter, and its position will be the ordering wave vector $\mathbf{Q}$. This is the reason why we involve $\langle \mathbf{S}_{-\mathbf{q}} \cdot \mathbf{S}_{\mathbf{q}} \rangle$, since it provides a good visual aid in determining the phase.

We mentioned in section 2.2 that the order parameter will be affected by finite size effects whenever we do a simulation. It will not be strictly zero above the phase transition, but decrease more slowly [6]. This will make it harder to locate the phase transition directly from the order parameter. Instead, we will use a quantity that takes $m^{\alpha}(\mathbf{q})$ as input.

2.9 The Binder cumulant

The **Binder cumulant** thoroughly simplifies the task of detecting the phase transition. It is sometimes referred to as the fourth-order cumulant and is defined as [5]

$$U_L = 1 - \frac{\langle m^4 \rangle_L}{3 \langle m^2 \rangle^2_L} \tag{2.45}$$

If we plot the Binder cumulant for different L as a function of temperature, we will get graphs $U_L(T)$ that cross at different temperatures T^*, as seen in figure (2.3). The locations of these crossings will in fact converge to the critical temperature T_c as $L \to \infty$. This can be shown by the convergence of U_L above and below the critical temperature. For $T > T_c$, U_L tends to zero as $U_L \propto L^{-d}$, where d is the dimensionality of the lattice. For temperatures smaller than the critical value, $T < T_c$, it will converge to $2/3$ with increasing L[5]. Therefore, the graphs must cross, and do so near the critical temperature.

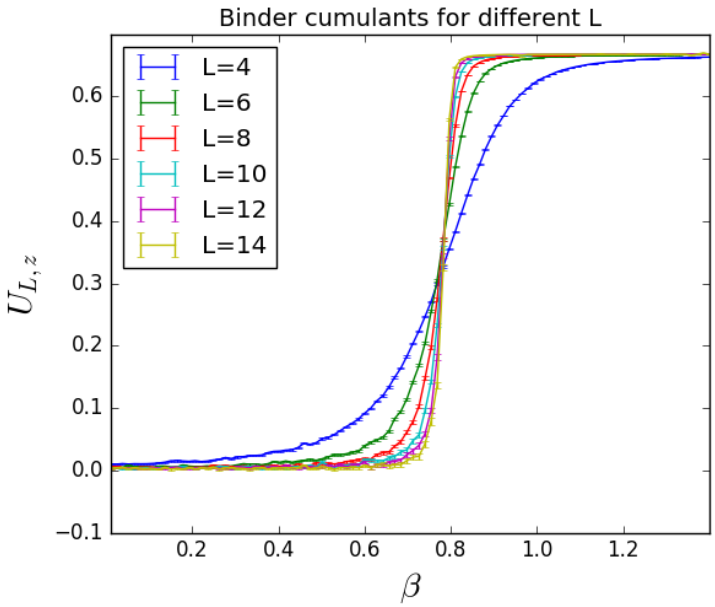

Figure 2.3: Typical behaviour of the Binder cumulants. This figure was made by using the Bootstrap method on the model of Jensen et. al., and is repeated in section 7.1. The magnetization is defined in terms of Eq. (2.44).

The scaling of the T^*'s with the system size L will be given in Chapter 7, and derived in Appendix F.

The value of U_L at the crossing, usually denoted by U^*, also converges to a specific value U_c as $L \to \infty$. This value is the same for large groups of systems. It is for instance independent of the details of the lattice structure, but depends on the shape and dimensionality of the system and the symmetry of the interactions[2]. U_c does not depend solely on the universality class, however, but is also sensitive to among others the boundary conditions and the shape of the system[4]. Studies on two-dimensional Ising systems with competing nearest- and next-nearest neighbour interactions has shown U_c varying with the ratio of the coupling strengths [22],[23],[1], though not by much for the ratios we consider[23]. For these reasons, we have not compared our result for U_c to other works.

Chapter 3

The models: An introduction

We will base our thesis on the models of three papers that suggest couplings for $LiNiPO_4$: one by Jensen et. al. [13], one by Li et. al. [15] and one by Toft-Petersen et. al. [25]. Jensen's partitipation in [13] was in connection with his PhD work, which we refer to for more information on the model. It is there, for instance, that he estimates the critical temperatures for the model, which we will ourselves set out to find.

3.1 Jensen et. al.

Table (3.1) shows the couplings for $LiNiPO_4$ suggested by Jensen et. al. [13] and Jensen in his PhD thesis[12]. The couplings are identical in both publications, except for being given with higher accuracy in the thesis. The suggested models contain both nearest and next-nearest neighbour couplings, which gives rise to the frustration often associated with incommensurability. The single-ion anisotropy, the paper states, will cause the spins to favour the z-direction. We will show that this is indeed the case later on. When one direction is energetically preferable in such a way, we say that the Hamiltonian has an easy axis. There are no Dzyaloshinskii-Moriya couplings in the model. Jensen justifies this by arguing that the canting is small and claims that the DM interaction is small compared to the other interactions[12].

The parameters of the model were found using a best fit to the spin wave exitation spectrum (which is called the spin wave dispersion). In order to obtain a good fit, the single-ion anisotropies were allowed to change with temperature according to table

Table 3.1: The couplings and single-ion anisotropies found by Jensen et. al (denoted by 'Article') [13] and Jensen in his dissertation (denoted by 'Thesis') [12].

	J_{yz}	J_y	J_z	J_{xy}	J_{xz}	D^x_{an}	D^y_{an}	D^z_{an}
Article	1.04(6)	0.670(9)	-0.05(6)	0.30(6)	-0.11(3)	0.339(2)	1.82(3)	0
Thesis	1.036	0.6701	-0.04969	0.2977	-0.1121	0.339	1.82	0

Table 3.2: How the single-ion anisotropy of Jensen et. al. varies with the temperature. The table is taken from [12].

T [K]	D_{an}^{x}	D_{an}^{y}	D_{an}^{z}
1.5	0.3392	0.9097	0
18.2	0.2046	0.9204	0
19.2	0.1812	0.7034	0
20.2	0.1350	0.6	0

(3.2). Table (3.1) is actually the couplings at 1.5 K. However, involving changing couplings will muddle our understanding of the different terms in the Hamiltonian, so we find it better to stick with the couplings of table (3.1).

In addition to listing the couplings, Jensen also gives the temperatures for the phase transitions. The commensurate-incommensurate phase transition occurs at about T= 20.8 K, while the incommensurate-paramagnetic one takes place at approximately T= 21.8 K.

3.2 Li et. al.

Table (3.3) shows the couplings for $LiNiPO_4$ suggested by Li et. al. [15]. The couplings were found using a best fit to the spin wave dispersion. The model has a few similarities with that of Jensen et. al.: the couplings all have the same signs and comparable sizes, and both disregard the antisymmetric exchange (DM). However, the ratios of nearest and next-nearest neighbour couplings will be different. It turns out that this ratio governs the incommensurability not just for the chain, but also for the face centered cubic lattice.

Table 3.3: The couplings and single-ion anisotropies found by Li et. al (2009)[15].

J_{yz}	J_y	J_z	J_{xy}	J_{xz}	D_x	D_y	D_z
0.94(08)	0.59(05)	-0.11(05)	0.26(02)	-0.16(02)	0.34(06)	1.92(01)	0

3.3 Toft-Petersen et. al.

Out of our three reference papers, Toft-Petersen et. al. is the only one that suggests a model containing Dzyaloshinskii-Moriya terms. The couplings are given in table (3.4). Note that except for the inclusion of the DM terms, the couplings are quite close to those of Jensen et. al.

Referring to Eq. (2.23), the DM-vector is $\mathbf{D}_{DM} = D_{14}\hat{y}$, and the interaction is only present between neighbours in the yz-plane. Spins that are neighbours in the other planes have no antisymmetric coupling.

Toft-Petersen et. al. found the Heisenberg couplings and the single-ion anisotropy through low temperature spin waves. The Dzyaloshinskii-Moriya coupling was found through measuring the angle of the spin canting[25].

Table 3.4: The couplings and single-ion anisotropies found by Toft-Petersen et. al (2011)[25]. D_x, D_y, D_z are the single-ion anisotropies in the x, y and z-direction, respectively, and D_{14} is the DM coupling between the x- and z-components of some of the spin neighbours (see text).

J_{yz}	J_y	J_z	J_{xy}	J_{xz}	J_{xz}	D_x	D_y	D_z	D_{14}
1.002	0.67	-0.06	0.321	-0.112	-0.23	0.413	1.423	0	$\pm$0.32

Chapter 4

Further background

This chapter will be two-fold: First, we use the spiralization parametrization for a chain to find the effect of the different terms in the Hamiltonian. Then, we find the form of the antiferromagnetic ordering wave vector for the chain and the face-centered cubic lattice. This section is not included in the general theoretical background as it is based on calculations specific to this thesis.

4.1 The spiralization parametrization for a chain

Since we shall discuss different models, we should have a better intuition of how the different terms in the Hamiltonian affect the state of the system. Assuming the spins rotate with a fixed angle about some set axis of rotation, we can make use of the parametrization

$$\mathbf{S}(\mathbf{r}) = \mathbf{u}\cos(\mathbf{Q}\cdot\mathbf{r}) + \mathbf{v}\sin(\mathbf{Q}\cdot\mathbf{r}) \tag{4.1}$$

Where $\mathbf{u}$, $\mathbf{v}$ are normalized, orthogonal vectors in the plane of rotation. We have done this for each term in the Hamiltonian. The details are listed in Appendix C, but we summarize our results.

- The nearest neighbour Heisenberg favours $Q = 0$ (FM) or $Q = \pi$ (AFM).
- Competing nearest- and next-nearest Heisenberg terms favours the incommensurate ordering given by θ in Eq. (2.19).
- The Dzyaloshinskii-Moriya interaction favours $Q = \pi/2$, i.e. orthogonal spin neighbours.
- The Dzyaloshinskii-Moriya interaction together with nearest neighbour Heisenberg terms favour an intermediate angle $Q = \arctan(\pm D_{DM}/J)$.
- The Dzyaloshinskii-Moriya interaction together with nearest- and next-nearest neighbour Heisenberg terms favours an intermediate angle for the couplings of Toft-Petersen et. al. (table (3.4)).

- For positive strengths D_{an}^{x}, D_{an}^{y}, D_{an}^{z}, the following applies for the single ion anisotropy terms

  1. If $D_{an}^{\alpha} > 0$, the spins will favour the $\beta\gamma$-plane.
  2. If $D_{an}^{\alpha}, D_{an}^{\beta} > 0$, the spins will favour the $\pm\hat{\gamma}$-direction.
  3. If all $D_{an}^{\alpha} > 0$, the energy will be shifted. The difference in the D_{an}^{α}'s will affect the spin orientations.

4.2 The ordering wave vector of an antiferromagnetic system

From Chapter 2, we know that the ordering wave vector $\mathbf{q}$ maximizes $m(\mathbf{q})$ Eq. (2.44). This should be the case if the ordering wave vector matches the rotation of the spins, i.e. $\mathbf{q} = \mathbf{Q}$. We have verified this in Appendix B. For the antiferromagnetic chain, the ordering wave vector is then $\mathbf{q} = \frac{\pi}{a}\hat{x}$.

For the fcc lattice, on the other hand, the sites take half-integer coordinates. Say that we want to find the periodicity in the y-direction. Then the difference in the y-coordinate between neighbours is $\Delta r_y = a/2$. If there is an antiferromagnetic ordering between nearest neighbours in the y-direction, we need an additional factor of 2 in q_y to compensate for the reduced lattice spacing. This is explained in greater detail in Appendix D.1. So for the fcc lattice, components of $q_w = \frac{2\pi}{a}\hat{w}$ in $\mathbf{w}$ signifies an antiferromagnetic ordering in direction $\hat{w} = \hat{x}, \hat{y}, \hat{z}$.

Chapter 5

Spin correlation functions of the models

This chapter shows plots of the spin correlation functions of the different models. The maxima of the spin correlation function is the order parameter, so these plots are helpful in determining the state of the system. The spin correlation function will be plotted against K, given by $\mathbf{q} = \frac{2\pi}{a}(0, K, 0)$.

5.1 Jensen et. al.

Figure (5.1) shows the spin correlation function for several temperatures T for the model of Jensen et. al.. It shows an antiferromagnetic peak that decreases with increasing temperature, but no sign of the incommensurate peaks. In other words, the model of Jensen et. al. fails to account for the commensurate-incommensurate phase transition.

Since we are interested in the ordering in the y-direction, it should be sufficient to look at the couplings J_{xy}, J_{yz} and J_y. Figure (5.2) shows a very simplified model, with $J_{yz} = 1.3337$ and $J_y = 0.6701$. These couplings are derived from the second row of table (3.1). Even with this simplified approach, the incommensurate phase does not appear.

However, if we set $J_{xy} = 0$, i.e. lower the nearest neighbour coupling to $J_{nn} = J_{yz} = 1.04$, the spin correlation function was found to exhibit two incommensurate peaks. A few plots are given in figure (5.3), with and without single-ion anisotropy. Evidently, the model of Jensen et. al. only needs a slight modification to yield an incommensurate phase. Such modifications are further addressed in section 6.2, Chapter 8 and Appendix G. The commensurate phase was however not found, so this is not a viable candidate for the commensurate-incommensurate phase transition either.

In Appendix B, figure (C.11) shows two plots of another model similar to Jensen. It shows two incommensurate peaks whose location varies very slightly with the strength of the single-ion anisotropy. Note that the difference in single-ion anisotropy is very large.

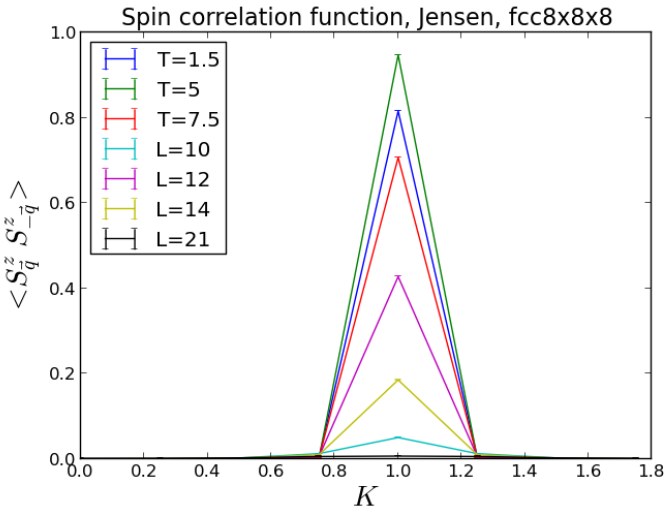

Figure 5.1: The spin correlation function for the model of Jensen et. al. for several temperatures.

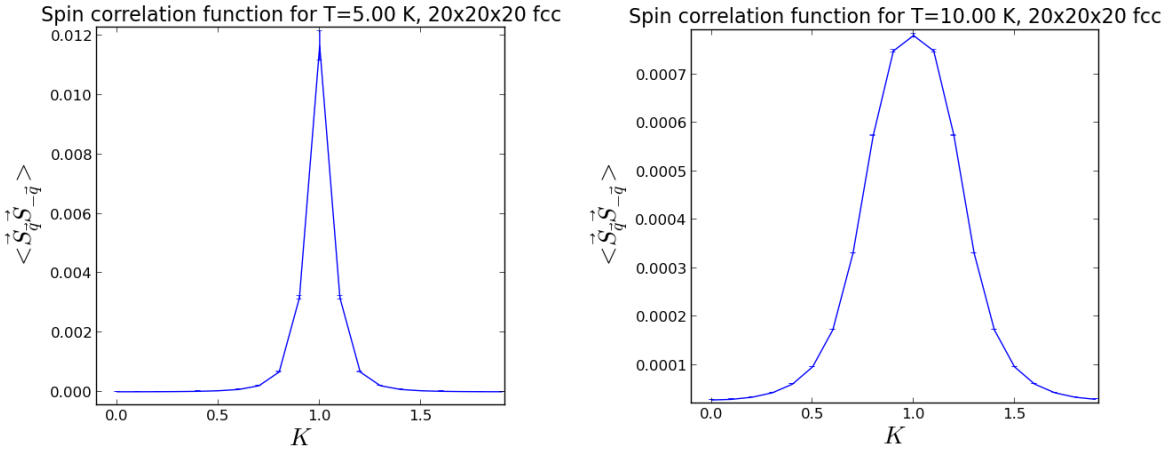

Figure 5.2: The spin correlation function for $J_{yz} = 1.3337$ and $J_y = 0.6701$, a simplified version of the Jensen et. al. model. We have included the plots of T= 5 K and T= 10 K. There is no incommensurate phase.

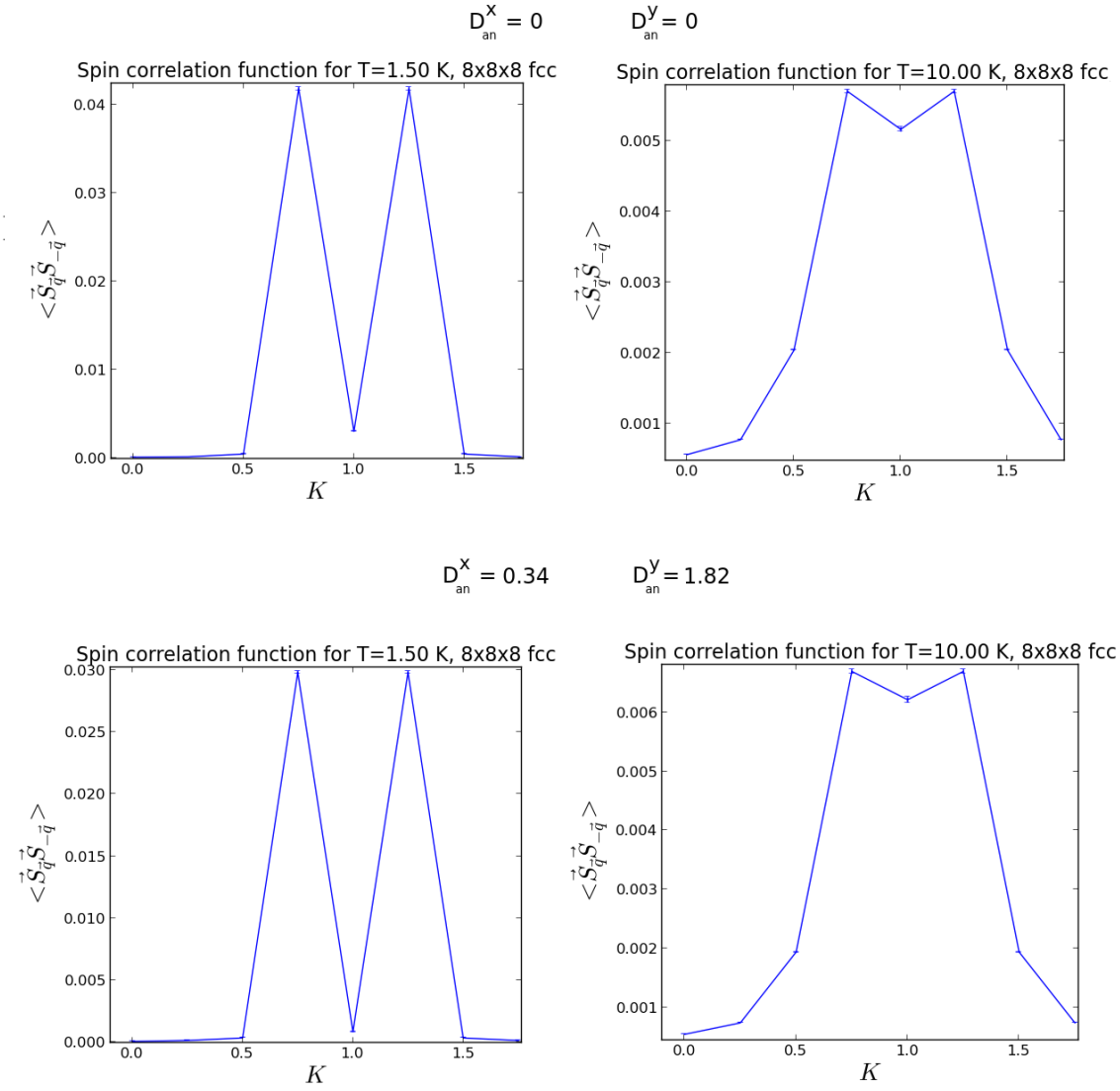

Figure 5.3: The spin correlation function for $J_{yz} = 1.04$ and $J_y = 0.67$, a simplified version of the Jensen et. al. model. We have included the function at T= 1.5 K and T= 10 K. For the upper two plots there is no single-ion anisotropy, while the lower two plots have $D^x_{an} = 0.34$ and $D^y_{an} = 1.82$.

5.2 Li et. al.

Figure (5.4) shows the spin correlation function for the model of Li et. al. for a set of different temperatures. Only the antiferromagnetic peak is present, so this model fails to account for the commensurate-incommensurate phase transition.

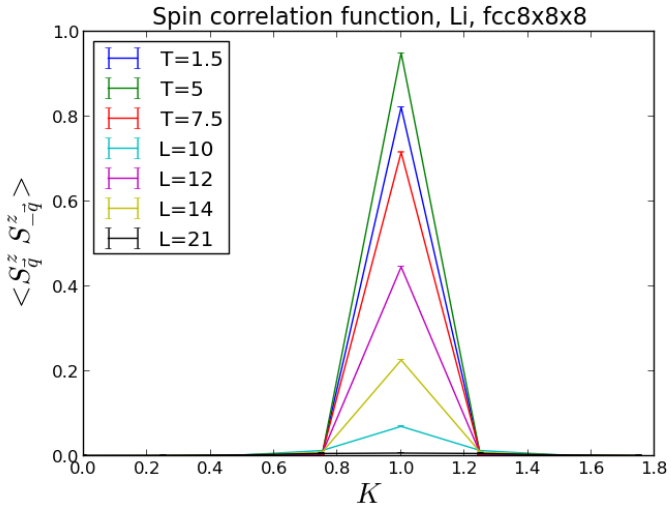

Figure 5.4: The spin correlation function for the model of Li et. al. for several different temperatures. No incommensurate peaks were found.

5.3 Toft-Petersen et. al.

Figure (5.5) shows the spin correlation function for a set of different temperatures for the model of Toft-Petersen et. al. We identify the incommensurate peaks, but see no antiferromagnetic peak for any temperature. Though the model captures the incommensurate phase, it therefore fails to account for the commensurate-incommensurate phase transition.

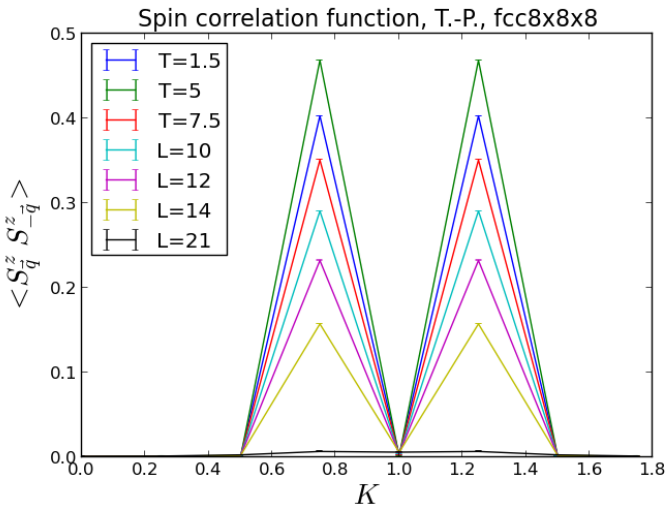

Figure 5.5: The spin correlation function for the model of Jensen et. al. for several temperatures.

Chapter 6

Ordering in the y-direction of the face-centered cubic lattice

The Hamiltonian with nearest and next-nearest neighbour Heisenberg couplings in all directions reads

$$\begin{aligned} H = J_{xz} \sum_{\langle ij \rangle_{xz}} \mathbf{S}_i \cdot \mathbf{S}_j + J_x \sum_{\langle\langle ij \rangle\rangle_x} \mathbf{S}_i \cdot \mathbf{S}_j + J_z \sum_{\langle\langle ij \rangle\rangle_z} \mathbf{S}_i \cdot \mathbf{S}_j \\ + J_{xy} \sum_{\langle ij \rangle_{xy}} \mathbf{S}_i \cdot \mathbf{S}_j + J_{yz} \sum_{\langle ij \rangle_{yz}} \mathbf{S}_i \cdot \mathbf{S}_j + J_y \sum_{\langle\langle ij \rangle\rangle_y} \mathbf{S}_i \cdot \mathbf{S}_j \end{aligned} \tag{6.1}$$

where we have ordered the terms according to how they couple spins in the y-direction. $\langle ij \rangle$ denotes neighbours ij in the given direction, while $\langle\langle ij \rangle\rangle$ denotes next-nearest neighbours in the given direction. The first line of the equation only contains couplings between spins in the same y-layer of the crystal, while the two next terms contains all couplings between adjacent y-layers and the last term couples spins two y-layers apart.

Applying the condition of spiralization, Eq. (4.1) yields a formidable Hamiltonian.

$$\begin{aligned} H = \frac{1}{2} N_{xz} J_{xz} \left[\cos\left(\frac{Q_x a}{2} + \frac{Q_z a}{2} \right) + \cos\left(\frac{Q_x a}{2} - \frac{Q_z a}{2} \right) \right] \\ + N_x J_x \cos(Q_x a) + N_z J_z \cos(Q_z a) \\ + \frac{1}{2} N_{xy} J_{xy} \left[\cos\left(\frac{Q_x a}{2} + \frac{Q_y a}{2} \right) + \cos\left(\frac{Q_x a}{2} - \frac{Q_y a}{2} \right) \right] \\ + \frac{1}{2} N_{yz} J_{yz} \left[\cos\left(\frac{Q_y a}{2} + \frac{Q_z a}{2} \right) + \cos\left(\frac{Q_y a}{2} - \frac{Q_z a}{2} \right) \right] \\ + J_y N_y \cos(Q_y a) \end{aligned} \tag{6.2}$$

N_α being the number of bonds in the α-direction. However, we will primarily be interested in a system with ordering wave vector $\mathbf{q} = \frac{2\pi}{a}(0, K, 0)$. The ordering wave

vector matches the spiralization of the spins, i.e. $\mathbf{Q} = \mathbf{q}$, just as we verified in Appendix B. Therefore, we will enforce $Q_x = Q_z = 0$.

Now, the Hamiltonian (6.2) simplifies to

$$H = A + (J_{xy}N_{xy} + J_{yz}N_{yz}) \cos\left(\frac{Q_y a}{2}\right) + J_y N_y \cos(Q_y a)$$

where the terms without a Q_y-dependence have been merged to form a constant A. We take the derivative to find the extremal points

$$\frac{\partial E}{\partial Q_y} = -\frac{a}{2}(J_{xy}N_{xy} + J_{yz}N_{yz}) \sin\left(\frac{Qya}{2}\right) - 2aJ_y N_y \sin\left(\frac{Q_y a}{2}\right) \cos\left(\frac{Q_y a}{2}\right) = 0$$

$$\left[(J_{xy}N_{xy} + J_{yz}N_{yz}) + 4J_y N_y \cos\left(\frac{Q_y a}{2}\right)\right] \sin\left(\frac{Q_y a}{2}\right) = 0$$

This is equivalent to what Nagamyia found in 1967 by Fourier transforming the couplings[16]. One solution of the equation is

$$\sin\left(\frac{Q_y a}{2}\right) = 0 \qquad \rightarrow \qquad Qy = \frac{2\pi n}{a}$$

where n is an integer. If n is odd, we have an antiferromagnetic ordering, and if n is even, we have a ferromagnetic ordering.

To find the other solution, we equate the terms in the bracket to zero. Rearranging, we obtain

$$\cos\left(\frac{Q_y a}{2}\right) = -\frac{J_{xy}N_{xy} + J_{yz}N_{yz}}{4J_y N_y} \tag{6.3}$$

or

$$Q_y a = \frac{2}{a} \arccos\left(-\frac{J_{xy}N_{xy} + J_{yz}N_{yz}}{4J_y N_y}\right)$$

When the right-hand side of Eq. (6.3) is ± 1, the ordering is ferromagnetic or antiferromagnetic. If the right hand side is somewhere in between -1 and 1, however, incommensurate ordering is favoured.

The number of bonds depends on the boundary conditions of the systems. For periodic boundary conditions, $N_{xy} = N_{yz} = N_{xz} = 2N$ and $N_x = N_y = N_z = N$, where N is the number of spins in our systems. Table (6.1) lists the number of bonds for the face-centered cubic lattice with open boundary conditions in the y-direction. The ratio between the number of next-nearest and nearest neighbour bonds tends to two as the system size increases.

The solution (6.3) favours an incommensurate ordering in the y-direction. The solution is only available for $J_{xy}N_{xy} + J_{yz}N_{yz} \leq 4J_y N_y$, however. In the limit of $N_{xy} = N_{yz} =$

Table 6.1: The number of bonds for the face-centered cubic lattice with open boundary conditions in the y-direction for an $L \times L \times L$ lattice.

	4	6	8	10	12	14	16	18	20	22
N_{xy}	112	408	992	1960	3408	5432	8128	11592	15920	21208
N_{yz}	112	408	992	1960	3408	5432	8128	11592	15920	21208
N_{xz}	128	432	1024	2000	3456	5488	8192	11664	16000	21296
N_y	60	210	504	990	1716	2730	4080	5814	7980	10626
N_z	64	216	512	1000	1728	2744	4096	5832	8000	10648
N_{xy}/N_y	1.867	1.943	1.968	1.980	1.986	1.990	1.992	1.994	1.995	1.996

$N_{xz} = 2N$ and $N_y = N$, this simplifies to $J_{xy} + J_{yz} \leq 2J_y$. Discarding the ferro- and antiferromagnetic solutions, incommensurate phases in the y-direction might be found for

$$\frac{1}{4}\left(J_{xy}N_{xy} + J_{yz}N_{yz}\right) < J_y N_y \qquad \text{for general } N \tag{6.4}$$

and

$$\frac{1}{2}\left(J_{xy} + J_{yz}\right) < J_y \quad \text{in the limit of } N_y = N,\ N_{xy} = N_{yz} = 2N \tag{6.5}$$

The incommensurate state has the lowest energy when the inequality (6.4) holds, which we have shown in Appendix E.

6.1 Discussion

By inspecting table (6.2), we can easily compare the sides of the inequality (6.5) in order to determine if the system is in the incommensurate regime. The model of Li et. al. fails the condition for incommensurability, meaning that we should not expect to observe such a phase at all. Our inspection of the spin correlation function in Chapter 5 agrees with this analysis.

The condition does however hold for the model of Jensen et. al. presented in [13]. Consequently, we would expect to observe an incommensurate phase for $J_{yz} + J_{xy} =$

Table 6.2: The couplings of the models, together with the right hand side of the condition (6.5). If the number in the second to last row is smaller than the number in the last row, the incommensurate phase has the lowest energy.

	J_{xy}	J_{yz}	$\frac{1}{2}\left(J_{xy} + J_{yz}\right)$	J_{xy}
Jensen, paper	0.3	1.04	0.67	0.67
Jensen, thesis	0.2977	1.036	0.66685	0.6701
Li	0.26	0.94	0.6	0.59
Toft-Petersen	0.321	1.002	0.6615	0.67

Table 6.3: A comparison of the energy for couplings in Jensen's regime. There is a very little energy difference between the incommensurate and the antiferromagnetic ordering of spins in the y-direction. The energies are per particle, and are given by Eq. (E.2) and (E.5) in Appendix E.

N regime	J_{yz}	J_y	I.C.	A.F.	Total diff.	Rel. diff.
$N_{yz} = 2N_y$	1.3337	0.6701	-1.99733	-1.9973	$3.2 \cdot 10^{-5}$	$1.6 \cdot 10^{-5}$
$N_{yz} = 2N_y$	1.34	0.67	-2.01	-2.01	0	0
$L = 8$	1.3337	0.6701	-1.9552	-1.9546	$5.8 \cdot 10^{-4}$	$3.0 \cdot 10^{-4}$
$L = 8$	1.34	0.67	-1.96746	-1.96712	$3.4 \cdot 10^{-4}$	$1.7 \cdot 10^{-4}$

1.3337 and $J_y = 0.6701$. Nevertheless, we see no such ordering in our plots of the spin correlation function.

We note that the inequality does not hold for $J_{yz} = 1.04$, $J_{xy} = 0.30$, $J_y = 0.67$ as the two sides are identical. If we take the open boundary conditions into account, though, incommensurability is permitted. We see this as inequality (6.4) does hold for the system sizes we run. However, we do not find such a phase for these couplings either.

We might consider the energy for the different extremal points. The ferromagnetic ordering maximizes the energy and is of no interest to us. The energy per spin for the systems with incommensurate and antiferromagnetic ordering in the y-direction are listed in table (6.3) for the couplings of Jensen and Jensen et. al. as presented in [12] and [13]. The phases are revealed to be close in energy, with an energy difference per particle of less than 10^{-3} meV for $L = 8$. This energy difference corresponds to a temperature of 0.012 K, so the system should not be sensitive to it at the temperatures we consider.

Of course, we have made an approximation in assuming spiraling spins. This is excellent for finding the ground state, but at non-zero temperatures, thermal excitations will appear and make the system less ordered. Spins might deviate from the spiralization, possibly by a lot. States like these are not covered by our approximation, so we do not know what their energies will be. The antiferromagnetic and the incommensurate ordering of Jensen et. al. are very close in energy, so there is the possibility that slightly unordered states close to the perfect AF ordering are more energetically favourable or more easily accessible than those close to the perfect incommensurate (IC) ordering. If that is the case, we will only see the antiferromagnetic phase. If we are further within the incommensurate regime defined by inequality (6.4), the difference between the energy of the AF ground state and the IC ground state will be larger, and we will observe the incommensurate state. Tweaking the couplings of Jensen et. al. somewhat, we can find where we first spot the incommensurate peaks.

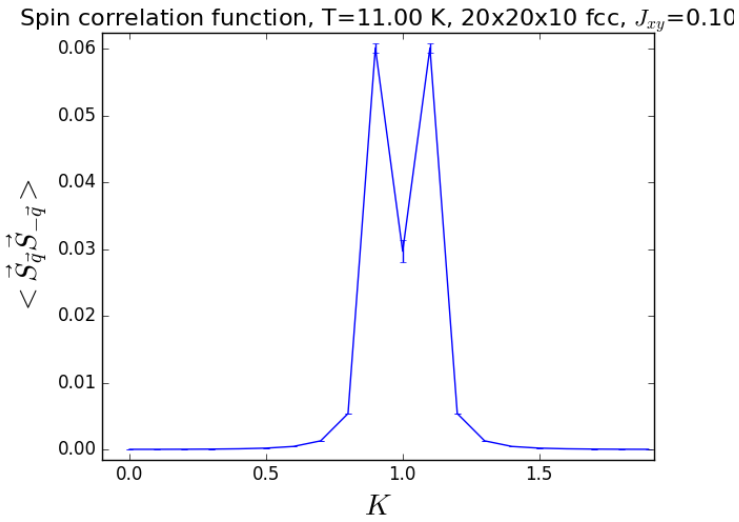

Figure 6.1: The spin correlation for $T = 11$K using Jensen's model with J_{xy} replaced by 0.10. The system shows two incommensurate peaks.

6.2 The incommensurate phase

The system is not incommensurate for Jensen's set of parameters, but can we find a set of couplings for which it is true? As we found in the previous subchapter, Jensen's next-nearest neighbour couplings are just small enough compared to J_y for Eq. (6.5) to hold. Since we cannot find the incommensurate phase for these couplings, we should try to lower $J_{xy} + J_{yz}$ so that we are further within this regime. We choose to change J_{xy} while keeping all the other parameters of the model as they are.

Figures (6.1) to (6.3) show the spin correlation functions for $J_{xy} = 0.10$, $J_{xy} = 0.11$ and $J_{xy} = 0.12$ for the $20 \times 20 \times 10$ fcc. For these values, $J_{xy} + J_{yz}$ corresponds to 1.14, 1.15 and 1.16, respectively. By Eq.s (2.36) to (2.38), the spacing between our k's is $\Delta k = 0.1$, so the incommensurate peaks should be visible in all plots. We see that the system is in the incommensurate state at $J_{xy} = 0.10$ and the antiferromagnetic state at $J_{xy} = 0.12$. At $J_{xy} = 0.11$, we identify a single peak of the spin correlation function, but the peak is broader than for $J_{xy} = 0.12$. This could imply that the system is on the verge of incommensurability. Keeping this in mind, we conclude that the incommensurate phase disappears somewhere between $J_{xy} + J_{yz} = 1.14$ and $J_{xy} + J_{yz} = 1.16$. This is equivalent to a ratio of nearest- and next-nearest neigbour couplings $\frac{J_{xy}+J_{yz}}{J_y}$ between 1.70 and 1.73.

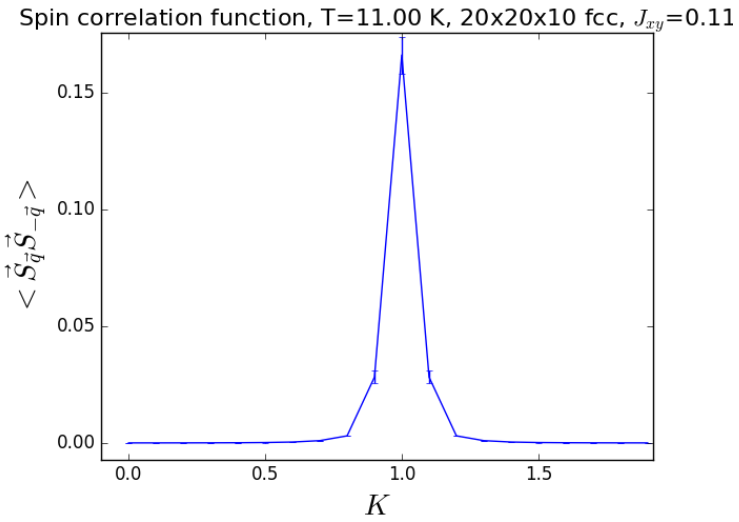

Figure 6.2: The spin correlation for $T = 11$K using Jensen's model with J_{xy} replaced by 0.11. The system no longer exhibits two incommensurate peaks, but the spin correlation function is a bit broader at the bottom.

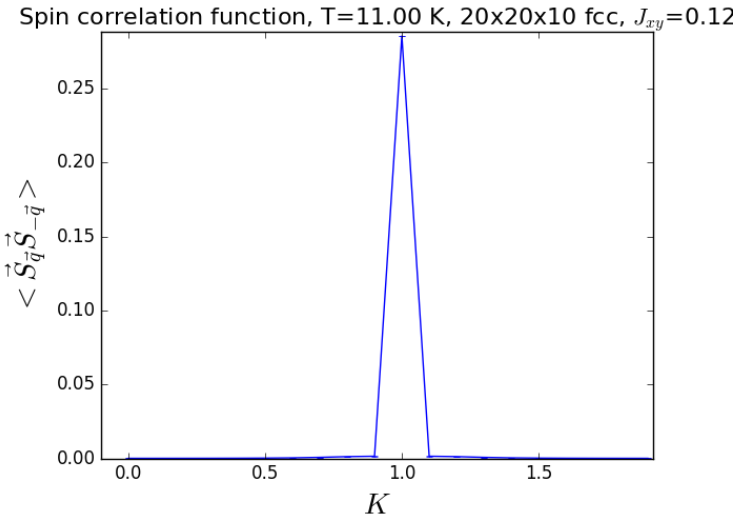

Figure 6.3: The spin correlation for $T = 11$K using Jensen's model with J_{xy} replaced by 0.12. The system no longer shows any trace of the two incommensurate peaks.

Chapter 7

Results from the finite size scaling analysis

The finite size scaling of crossing points is derived in Appendix F. Using the results (F.4), (F.6) and (F.7) together with $\delta = t = \frac{T-T_c}{T_c}$, we wind up with a couple of scaling relations that we can use to find ν and the first irrelevant exponent ω. From the value of the temperature at the crossing, we got

$$T^* = T_c + xL^{-1/\nu-\omega} \tag{7.1}$$

or

$$\log(T^* - T_c) = -\left(\frac{1}{\nu} - \omega\right)\log L + \log x \tag{7.2}$$

where x is some constant that does not depend on L. We get a similar relation for the value of the Binder cumulant at the crossing

$$U^* = U_c + bL^{-\omega} \tag{7.3}$$

or

$$\log(U^* - U_c) = -\omega \log L + \log b \tag{7.4}$$

In Appendix F, we also found that the derivative s of the Binder cumulant can be used to find an estimate $1/\nu^*$ of $1/\nu$, where

$$\frac{1}{\nu^*(L)} = \frac{1}{\ln\left(1 + \frac{\Delta L}{L}\right)} \ln\left(\frac{s\left(t^*, L + \Delta L\right)}{s\left(t^*, L\right)}\right) \tag{7.5}$$

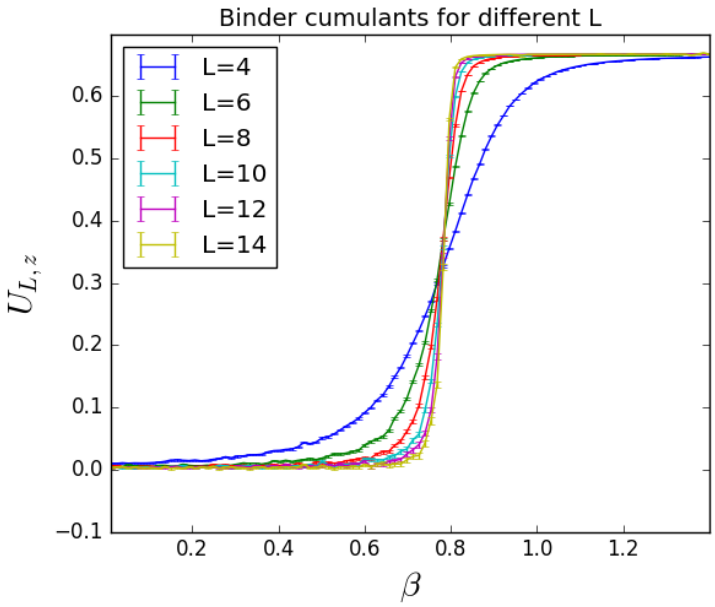

Figure 7.1: The Binder cumulants for the model of Jensen et. al. The magnetization is defined in terms of Eq. (2.44) with the antiferromagnetic ordering wave vector.

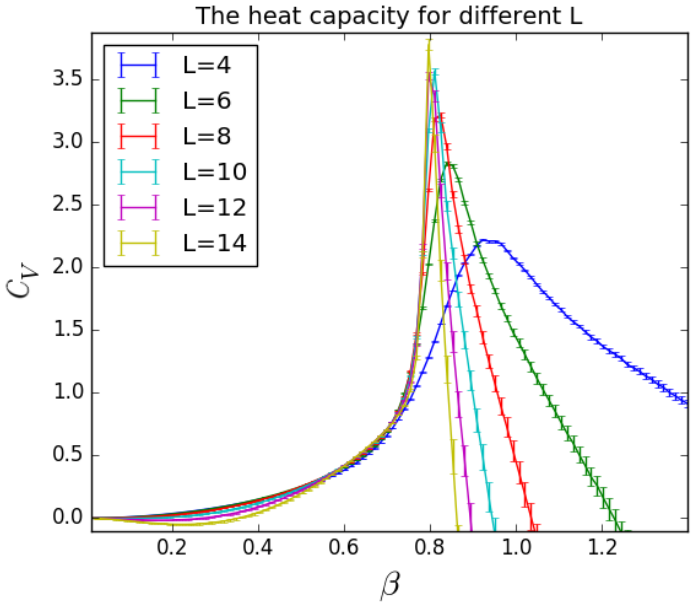

Figure 7.2: The heat capacity per particle for the model of Jensen et. al.

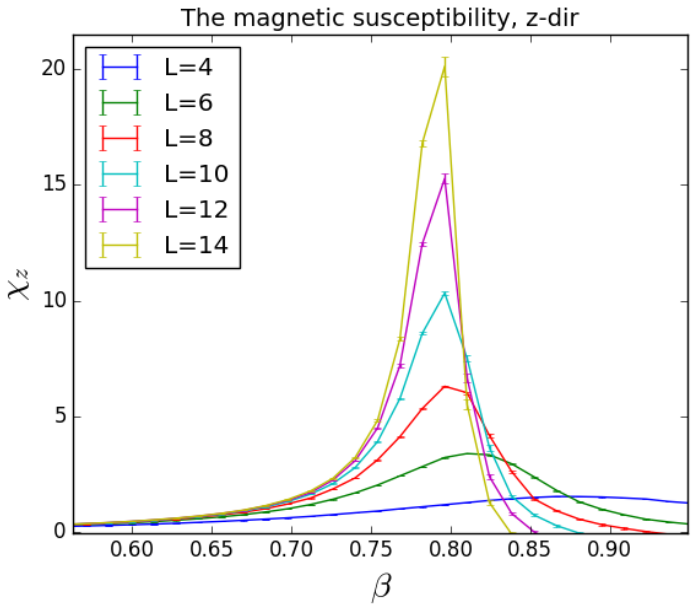

Figure 7.3: The magnetic susceptibility per particle for the model of Jensen et. al. The susceptibility is in terms of the z-component of the spin.

7.1 Jensen et. al.

Figures (7.1) to (7.3) show plots of several quantities that are of interest when doing finite size scaling: The Binder cumulant, the magnetic susceptibility and the specific heat capacity. L gives the size of the system, as we have studied an $L \times L \times L$ lattice. We have employed open boundary conditions in the y-direction. The simulations used to generate these overview plots were done with 10 000 equilibration sweeps and 10 000 lattice sweeps per bin in 100 bins. We merged output from three different sets of random number seeds. We see that the Binder cumulants takes the form described in section 2.9, and that the peaks of the susceptibility and heat capacity move towards lower β with increasing system size. Other than the drift in the temperature, the peaks of the latter quantities increase in magnitude with increasing L. We will find a few critical exponents from the drift in a while. First, we will extract information from the Binder cumulant crossings, to which end 10^6 latttice sweeps were used.

Making plots of Eq.s (7.2) and (7.4), we expect the data points to give a straight line. We could make the plots and read the critical exponents off the slopes. However, that would require us to know T_c and U_c in advance, which we do not. Instead, we will plot graphs of T^* and U^* against L^{-p} for different p and observe when the points appear to reside on a line. Those values of p will be our estimate of the critical exponents. We used figures such as (7.4) and (7.5) to evaluate the suitabillity of the exponent p. Numpy's polyfit function is plotted as a dashed line to help guide the eye.

For small system sizes, correction terms to Eq.s (7.1) and (7.3) will have a larger effect. For that reason, we will try to weight figure (7.5) more than figure (7.4) in our

Table 7.1: A comparison of the critical exponents of different systems. The 3D Ising and Heisenberg models are taken from [6]. The results from our simulations are listed under the second horizontal line.

Type	α	γ	ν
Ising, theory	0.11	1.24	0.63
Ising, experiments	$0.11^{+0.01}_{-0.03}$	$1.24^{+0.16}_{-0.04}$	0.63 ± 0.04
Heisenberg, theory	-0.12	1.39	0.71
Heisenberg, experiment	$0.1^{+0.05}_{-0.04}$	1.4 ± 0.07	0.7 ± 0.03
Jensen, χ and c_V	0.22±0.06	1.2±0.3	0.50±0.13
Jensen, Binder, visual	–	–	1.0±1.4
Jensen, Binder, curve_fit	–	–	0.7±0.4

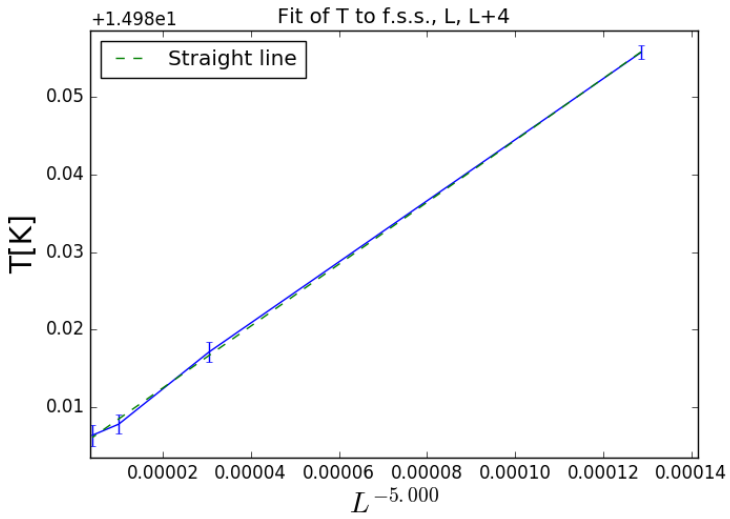

Figure 7.4: An example of the plots used to find a range for the exponent $\frac{1}{\nu} + \omega$. All points are included.

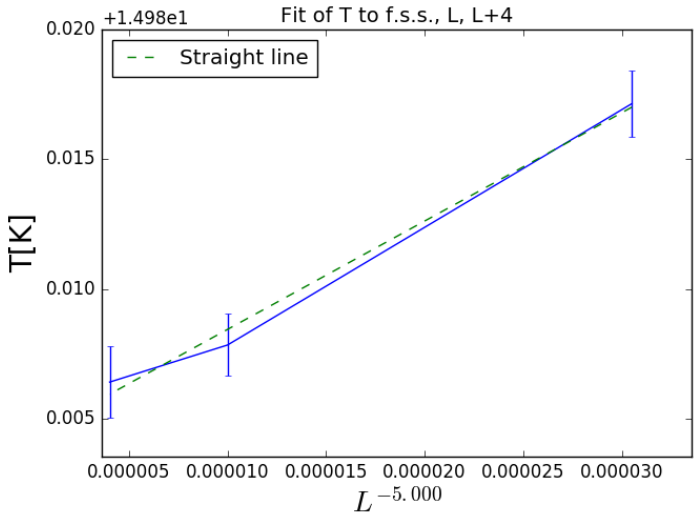

Figure 7.5: An example of the plots used to find a range for the exponent $\frac{1}{\nu} + \omega$. The smallest system size is left out.

evaluation of the different p's. Still, we might weight the small system sizes too much.

In order to find T_c and U_c, we will use polyfit to find the straight line using L^{-p} for the p's we found from the visual inspection. The slope and the intersection with the y-axis will then correspond to the weight and the critical value, respectively. Since these are found by a fit to a set of points, they are related quantities, and we cannot use Eq. (A.9) of Appendix A.2 to estimate the uncertainty. Instead, we will take the somewhat crude approach of finding the critical value for $p + \Delta p$, p and $p - \Delta p$ and giving the uncertainty from these.

We have chosen to consider the crossings between L and $L + 4$. Strictly speaking, this means increasing $\frac{\Delta L}{L}$ by a factor of two compared to L, $L + 2$. The derivation of the finite size scaling was done assuming $\frac{\Delta L}{L}$ to be small, which holds better for $\Delta L = 2$ than it does for $\Delta L = 4$.

However, the standard deviation of the crossings is lower for $\Delta L = 4$ than for $\Delta L = 2$, as seen from table (7.2). This is because the slopes of the graphs differ more for $\Delta L = 4$, as we can see by figure (7.6). When two graphs have almost the same slope, small variations in the $U^*(T)$'s will affect the location of the crossing quite a bit. The Bootstrap method is based on random sampling, so such variations will definitely appear. The only way to decrease this effect is to increase the length of our simulations. As mentioned in Appendix A.2, the standard deviation of the mean scales as roughly $1/\sqrt{N_{\text{sim}}}$, where N_{sim} is the number of measurements. Obtaining significantly better results clearly costs a lot of computation time.

The values of T^* are plotted against L^{-1} for both ΔL in figures (7.7) and (7.8). Both plots show T^* decreasing monotonously as a function of the inverse length, except for the points $L = 14$ and $L = 16$ for $\Delta L = 2$. However, these T^* *do* decrease monotonously within the error bars, just as for $\Delta L = 4$. Due to the seemingly non-monotonous behav-

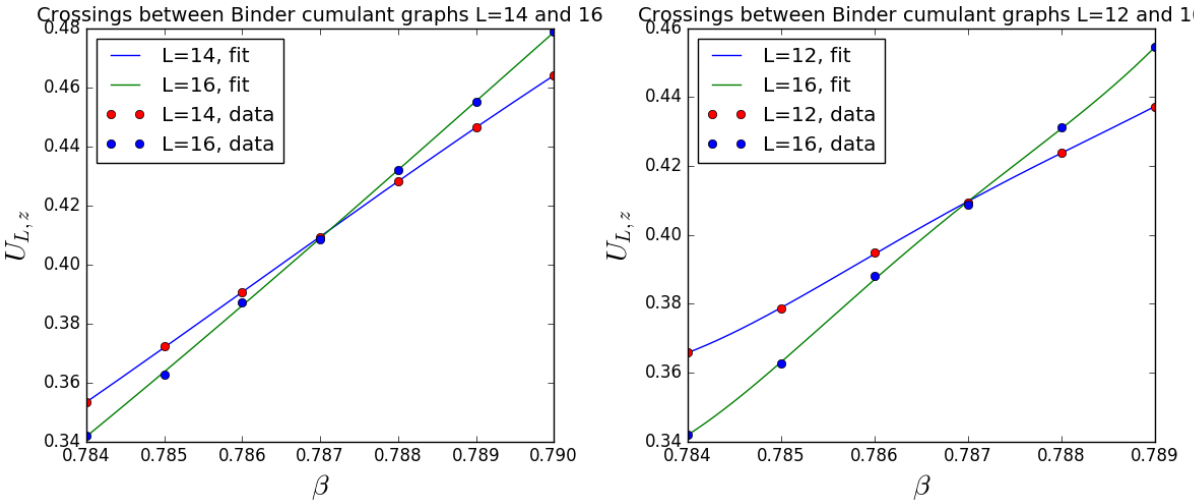

Figure 7.6: The results of one Bootstrap run for large L. To the left is the Binder cumulant crossings for $\Delta L = 2$, and the right is for $\Delta L = 4$. The slopes clearly differ more for $\Delta L = 4$ than for $\Delta L = 2$.

Table 7.2: Standard deviations for T^* and U^* from the crossings of L, $L+2$ and L,$L+4$. Since we consider several different L, we look at the average standard deviations.

	T, $\Delta L = 2$	T, $\Delta L = 4$	U, $\Delta L = 2$	U, $\Delta L = 4$
Average error	0.0014	0.0010	0.0010	0.00069

ior, we found it easiest to inspect L, $L+4$.

The first column of table (7.3) shows the results of the visual inspection. All simulations were done with 10^6 lattice sweeps. As the results were found by visual inspection, the error bars on the critical exponents are quite large. Even though we found T_c and U_c through the critical exponents, they have a much lower uncertainty.

In an effort to decrease the error bars on the critical exponents, we have tried another approach. We can apply scipy's optimize.curve_fit-function to obtain a least-squares fit of Eq.s (7.1) and (7.3) to find the values. We will use the best-fit parameters to plot Eq.s (7.2) and (7.4) as a visualization. Obviously, a three-parameter fit of only a few values is a bit shaky. Furthermore, the fit will weight the crossing points of the small system

Table 7.3: An estimate of the critical exponents ω and $\frac{1}{\nu}$ from the finite-size scaling analysis. The critical temperature T_c and U_c is also included. The data were found by analysis of the crossings between L and $L+4$.

Analysis	ω	$\frac{1}{\nu}+\omega$	$\frac{1}{\nu}$	ν	T_c	U_c
Visual	3±1	4±1	1.0±1.4	1.0±1.4	14.736±0.007	0.411±0.003
Curve fit	3.6±0.7	5.1±0.3	1.5±0.8	0.7±0.4	14.7436±0.0017	0.414±0.004

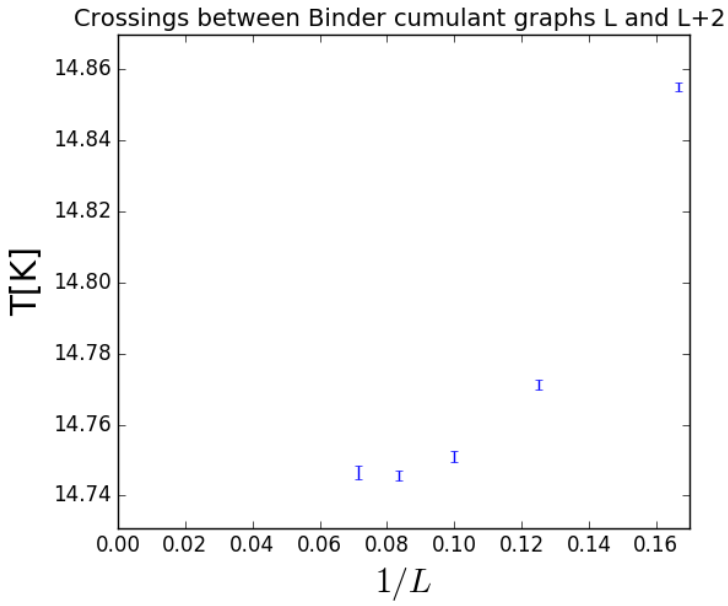

Figure 7.7: The crossing temperatures T^* plotted against L^{-1} for different L, $L + 2$. 10^6 lattice sweeps were used in the Monte Carlo procedure.

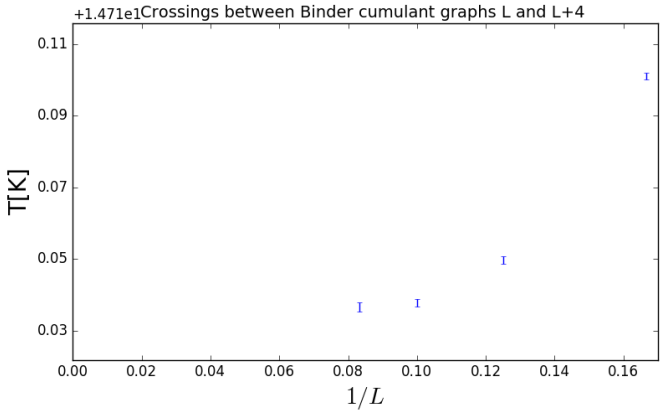

Figure 7.8: The crossing temperatures T^* plotted against L^{-1} for different L, $L + 4$. 10^6 lattice sweeps were used in the Monte Carlo procedure.

Table 7.4: The critical temperature and critical exponents from the finite-size scaling analysis of the Binder crossings. The first column denotes what kind of crossing points we have fed into curve_fit. "av" is simply the average from our Bootstrap procedure. To generate "av+stdv", the standard deviation has been added to the average at each point. For "av-stdv", the standard deviation has been subtracted.

Crossing between	T_c	x	$\frac{1}{\nu}+\omega$
L, L+2, av	14.7429±0.0015	736±379	4.9±0.3
L, L+2, av+stdv	14.7446±0.0016	777±435	4.9±0.3
L, L+2, av-stdv	14.7412±0.0014	698±329	4.9±0.3
L, L+4, av	14.7438±0.0017	608±529	5.1±0.5
L, L+4, av+stdv	14.7451±0.0017	680±620	5.2±0.5
L, L+4, av-stdv	14.7424±0.0017	545±453	5.0±0.5

Table 7.5: The value of the Binder cumulant at the critical temperature, U_c, and critical exponent ω from the finite-size scaling analysis of the Binder crossings. The first column denotes what kind of crossing points we have fed into curve_fit. "av" is simply the average from our Bootstrap procedure. To generate "av+stdv", the standard deviation has been added to the average at each point. For "av-stdv", the standard deviation has been subtracted.

Crossing between	U_c	b	ω
L, L+2, av	0.4117±0.0018	-40.0±30.9	3.7±0.4
L, L+2, av+stdv	0.4139±0.0016	-29.6±17.8	3.5±0.3
L, L+2, av-stdv	0.4096±0.0020	-55.1±53.8	3.9±0.6
L, L+4, av	0.4116±0.0016	-44.3±35.5	3.9±0.5
L, L+4, av+stdv	0.4132±0.0016	-33.7±23.3	3.7±0.4
L, L+4, av-stdv	0.4102±0.0017	-59.5±55.2	4.1±0.5

sizes just as much as the crossing points of the larger ones. This is unfortunate since the smaller system sizes are more vulnerable to correction terms.

Tables (7.4) and (7.5) show the result of applying curve_fit to the data. We have included the results from the crossing between L and $L+2$ and crossings between L and $L+4$. Additionally, we have added and subtracted the standard deviation at each point to see how the uncertainty in our crossings affects the results. A plot of Eq. (7.2) for $\Delta L = 2$ and $\Delta L = 4$ is given in figure (7.9). We clearly see that $\Delta L = 4$ gives the best approximation to a straight line, which is what we want. In plotting U^* for the two values of ΔL, we get a plot similar to figure (7.9). In using curve_fit, we will therefore consider the Binder crossings of $\Delta L = 4$, just as we did for the visual inspection.

Tables (7.6) and (7.7) take the uncertainty in both the weight and the crossings into account. The data were fit to Eq.s (7.1) and (7.3), but this time with the weight fixed, so that there were only two parameters to find. This was done for a series of weights in the

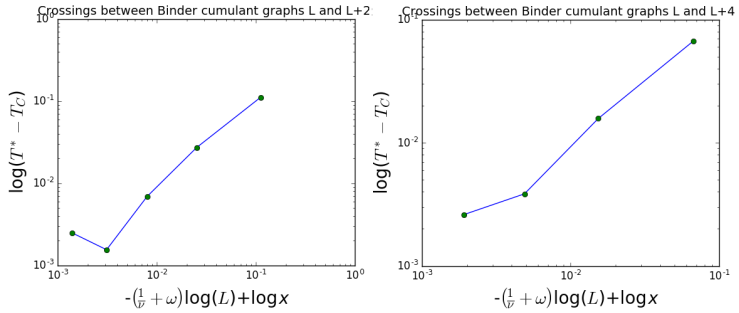

Figure 7.9: A plot of Eq. (7.2) using the averages from table (7.4) from the crossing between system L and L+2 (left) and L and L+4 (right). We expect a straight line in this log-log plot, which is best accomplished by L and L+4.

Table 7.6: The ranges of T_c and $\frac{1}{\nu} + \omega$ found from varying the weight in Eq. (7.1).

System sizes	Smallest T_c	Largest T_c	Smallest $\frac{1}{\nu} + \omega$	Largest $\frac{1}{\nu} + \omega$
L, L+2	14.7397441803	14.7445175992	4.44296833505	5.09350410004
L, L+4	14.7418466153	14.745259632	4.72679379627	5.38412071062

Table 7.7: The ranges of U_c and ω found from varying the weight in Eq. (7.3).

System sizes	Smallest U_c	Largest U_c	Smallest ω	Largest ω
L, L+2	0.410021054892	0.417156448785	2.84284497249	4.0128773809
L, L+4	0.410037480382	0.417420188693	2.88781767779	4.2782802545

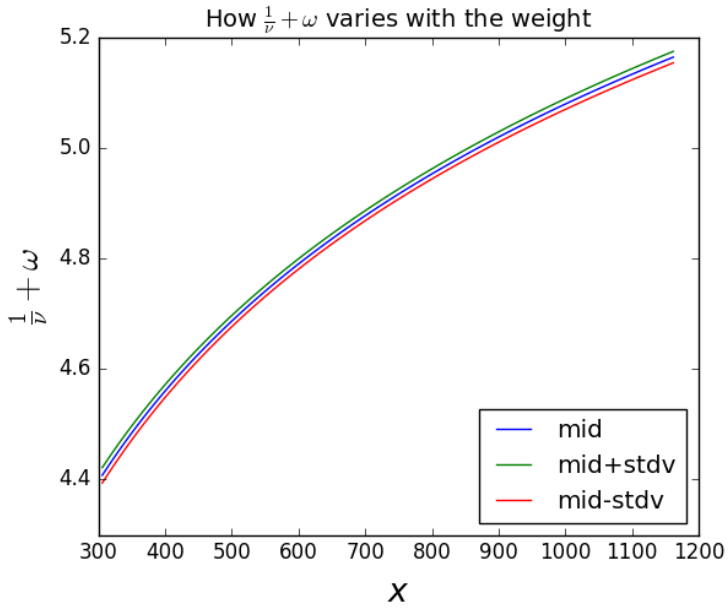

Figure 7.10: How our estimate of the exponent $\frac{1}{\nu}+\omega$ varies with the weight in (7.1), denoted by x. The fitting was done by curve_fit. The middle graph, ”mid”, was found by feeding the average from the Bootstrap procedure to curve_fit. To generate ”mid+stdv”, the standard deviation has been added to the average at each point before feeding the data. For ”mid-stdv”, the standard deviation was subtracted. The data set was generated by studying the crossings of the graphs with dimensionality L and $L+2$.

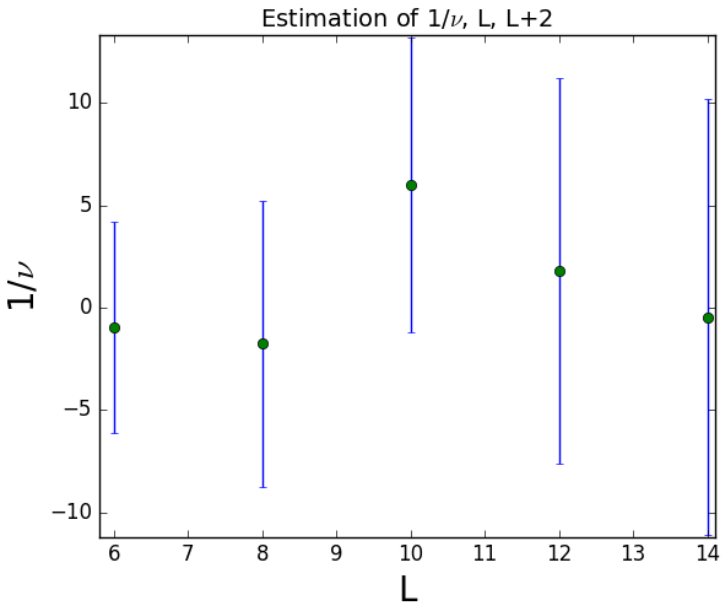

Figure 7.11: An estimate of the exponent $1/\nu$ from the slope of the Binder cumulants, as found by Eq. (7.5). The data set was generated by studying the crossings of the graphs with dimensionality L and $L+2$.

range given in table (7.4) and (7.5), yielding a lot of different fits. The standard deviations were added or subtracted to the data set to yield even more fits. The smallest and the largest parameters from these fits are given in tables (7.6) and (7.7). The dependence of the weight is visualized in figure (7.10).

We have also attempted to find the exponent $1/\nu$ by the slope of the derivative at the crossing, by applying Eq. (7.5) at every Bootstrap step after the crossing T^* has been found. Unfortunately, the uncertainty in the approximation was too large to yield anything useful, with the standard deviation often surpassing the average itself. The uncertainty actually increases with L. For small L, $s(t^*, L)$ is significantly smaller than $s(t^*, L+2)$, as seen from figure (7.6). The argument of ln is then quite large, and $\ln(x)$ changes slower for large x . For large L, the Binder cumulants of L and $L+2$ have almost the same slope, so that T^* and hence the $s(t^*, L)$'s vary more. In this regime, the logarithm changes faster, so there should be a larger spread in $1/\nu^*$. So the standard deviation increases with L. This is unfortunate since $1/\nu^*(L)$ should converge to $1/\nu$ as $L \to \infty$.

The magnetic susceptibility

The peak of the magnetic susceptibility scales as

$$\chi_{max}(L) = L^{\gamma/\nu}\tilde{\chi}\left(L^{1/\nu}t\right) \tag{7.6}$$

Table 7.8: The critical temperature and the critical exponent found from finite-size scaling of the magnetic susceptibility and the heat capacity per particle.

α/ν	γ/ν	$1/\nu$	ν	α	γ	T_c
0.432 ± 0.003	2.33 ± 0.09	2.0 ± 0.5	0.50 ± 0.13	0.22 ± 0.06	1.2 ± 0.3	14.72 ± 0.03

in the vicinity of the phase transition. $\tilde{\chi}\left(L^{1/\nu}t\right)$ is called the scaling function for the susceptibility, and it does not depend on the system size[17]. t is the reduced temperature, $t = \frac{T-T_c}{T_c}$. As opposed to Eq. (7.1) and (7.3), χ_{max} is directly proportional to $L^{\gamma/\nu}$, so the critical exponent can easily be found by taking the logarithms on both sides

$$\log\left(\chi_{max}\right) = \frac{\gamma}{\nu}\log(L) + \log\left(\tilde{\chi}\left(L^{1/\nu}t\right)\right) \tag{7.7}$$

The data from our simulations were run through the Bootstrap procedure, locating the maxima at every step. The data for this section and the next were generated using 10^5 equilibration sweeps, 100 bins and 10^5 lattice sweeps per bin. Numpy's polyfit function was used to make a least squares line fit of the logarithm of the data points. The results of the simulation are listed in table (7.8).

The peak of the magnetic susceptibility also moves with *temperature* for different system sizes. The scaling goes as [17]

$$T_{\chi_{max}}(L) = T_c + x_{max}L^{-1/\nu} \tag{7.8}$$

where x_{max} is constant with respect to L. Again, we perform a visual inspection of the data points vs L^{-p}. The results are listed in table (7.8) together with those from Eq. (7.7).

The specific heat

The specific heat scales as

$$c_{V,max}(L) = L^{\alpha/\nu}\tilde{c}\left(L^{1/\nu}t\right) \tag{7.9}$$

where $\tilde{c}$ is the scaling function for the specific heat. Just as $\tilde{\chi}$, $\tilde{c}$ does not depend on L [17]. We can read the exponent α/ν off of the slope of the log-log plot

$$\log\left(c_{V,max}\right) = \frac{\alpha}{\nu}\log(L) + \log\left(\tilde{c}\left(L^{1/\nu}t\right)\right) \tag{7.10}$$

The results are listed in table (7.8). The critical exponents found from c_V and χ, namely α, γ and ν, are also listed in table (7.1).

The uncertainty in ν found by Eq. (7.8) is much smaller than the ones we found from the treatment of the Binder cumulant. Even though ν found from curve_fit had quite a small uncertainty as well, that approach weighted all system sizes the same. In our

Table 7.9: The critical temperature found using finite-size scaling of the different quantities.

	Binder, visual	Binder, curve_fit	From $T_{\chi_{max}}(L)$
T_c	14.736±0.007	14.736±0.0017	14.72±0.03

visual analysis of $T_{\chi_{max}}$, we were able to ascribe the data points of large L with more significance. That will help compensate for the effect of correction terms, which might not be negligible for small systems.

We also have multiple estimates of the critical temperature, gathered in table (7.9). Yet again, we don't put too much emphasis on the results of curve_fit: the error estimate on T_c is probably too small to compensate for possible correction terms in Eq. (7.1). For the other two quantities, we had the possibility of reducing that bias. T_c from $T_{\chi_{max}}(L)$ seems to depend more strongly on ν than T_c from T^* does, since it had the smallest error in ν and the largest uncertainty in T_c. The first row of table (7.9) therefore seems like the more reliable option.

We can compare our critical exponents with those of 3D Ising and Heisenberg models listed in table (7.1). Our exponent ν agrees with the one of 3D Ising within the uncertainty, as do γ. α, however, is a bit too large to fit with either of the models, but it is closer to exponent of the 3D Ising model than to the 3D Heisenberg. Since the Hamiltonian have an easy axis, our system is practically the same as the Ising system.

7.2 Li et. al.

Figures (7.12) to (7.14) show the Binder cumulant, the heat capacity per spin and the magnetic susceptibility for the model of Li et. al. for different L's. The simulations were run with 10 000 equilibration sweeps, 100 bins and 10 000 lattice sweeps per bin. The Binder cumulant was studied closer to estimate the values of T_c and U_c. We performed the visual inspection we did in the previous chapter to arrive at the results of table (7.10). The results were generated using 10^6 lattice sweeps per bin. We note that the critical temperature is $T_c = 14.978 \pm 0.006$ a bit higher than that of Jensen et. al.

Table (7.11) shows that the value of U_c is the same for the models of Jensen et. al. and Li et. al. within the uncertainty. The models differ by the strengths of the couplings, which should not affect the universality class. We know that the critical value of the Binder cumulant is not unique within a given universality class, but depends on

Table 7.10: The results from analyzing the Binder cumulant of Li et. al. Visual inspection of the plots were used to determine the exponents, and T_c and U_c found from there.

$\frac{1}{\nu} + \omega$	ω	$\frac{1}{\nu}$	ν	T_c	U_c
5 ± 1	4 ± 1	1.0 ± 1.4	1 ± 1.4	14.978 ± 0.006	0.411 ± 0.003

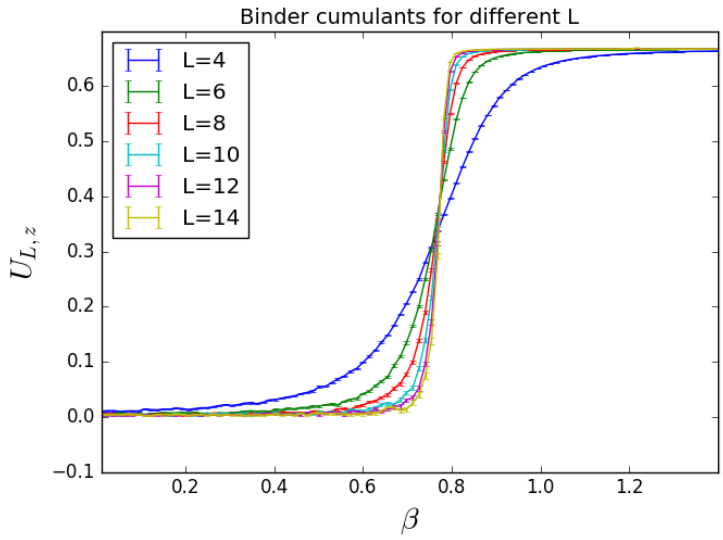

Figure 7.12: The Binder cumulants for the system of Li et. al. The Binder cumulant was found in terms of the z-component of the magnetization in Eq. (2.44) for the antiferromagnetic ordering wave vector.

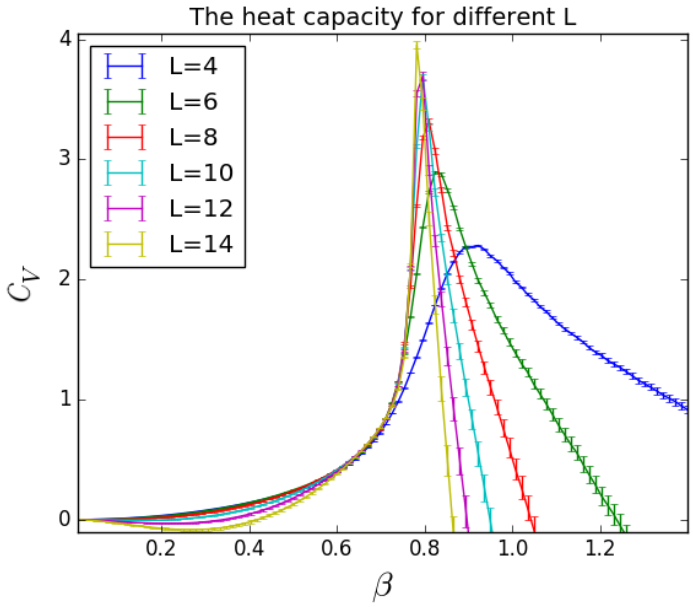

Figure 7.13: The heat capacity per particle for the system of Li et. al.

Table 7.11: The critical value of the Binder cumulant, U_c, for the models of Jensen et. al. and Li et. al. The values are the same within the uncertainty.

	Jensen, visual	Jensen, curve_fit	Li, visual
U_c	0.411±0.003	0.414±0.004	0.411 ± 0.003

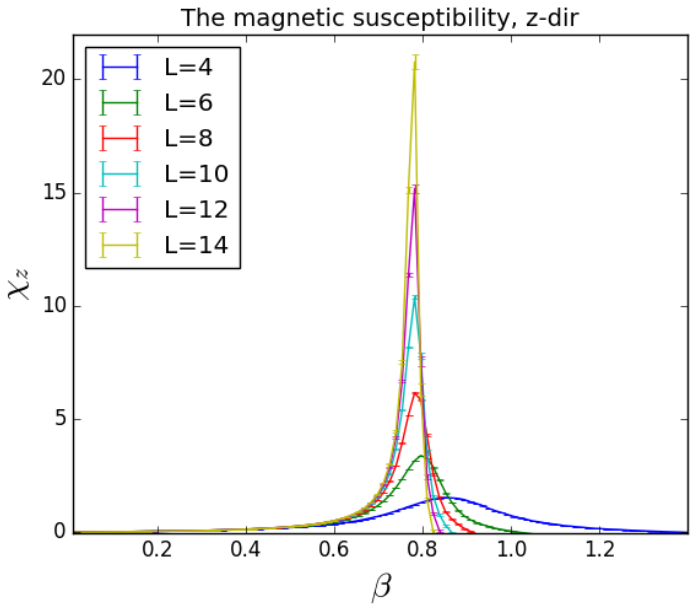

Figure 7.14: Magnetic susceptibility in the z-direction per particle for the system of Li et. al.

the boundary conditions and the shape of the system. These are however fixed in our simulations, so we *do* expect to get the same value of U_c for the two systems.

In section 2.9, we also mentioned reports of U_c depending on the relative strengths of the couplings in the frustrated 2D Ising model. Fig. 4 of [23] shows that for a large interval of ratios, U_c hardly changes. The couplings of Li et. al. and Jensen et. al. actually belongs to this interval. Since such an interval exists, our findings do not contradict those of [22], [23] and [1].

7.3 Toft-Petersen et. al.

Figure (7.15) shows the Binder cumulant for three different system sizes. The Binder cumulant remains small for all system sizes, so there clearly is no antiferromagnetic-paramagnetic phase transition for this model. The results of Appendix C, which focuses on the spin chain, suggests that this model should exhibit an incommensurate phase. This is confirmed by our observations in section 5.3.

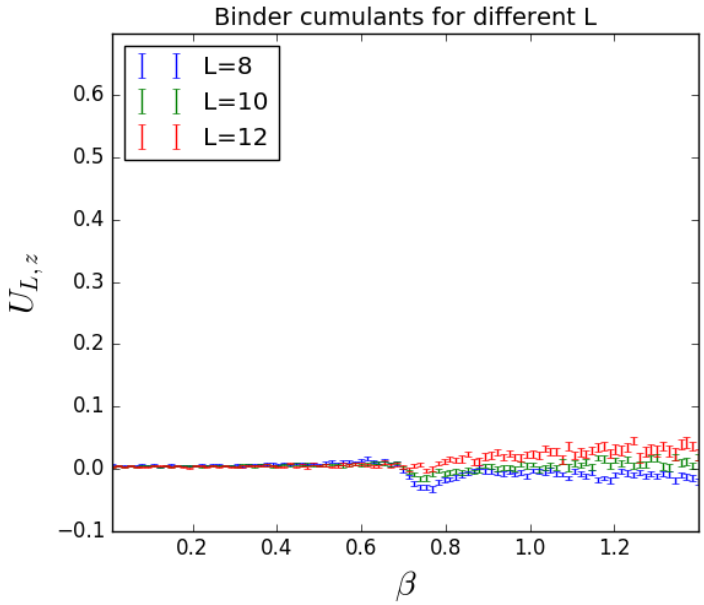

Figure 7.15: The Binder cumulants for the system of Toft-Petersen et. al. The Binder cumulant was found in terms of the z-component of the magnetization in Eq. (2.44) for the antiferromagnetic ordering wave vector.

Chapter 8

Modifying the Jensen et. al. model

8.1 Varying J_y in the Jensen et. al. model

Figure (8.1) shows that the crossing temperature T^* for the Binder cumulants $L = 12$ and $L = 14$ decreases with increasing J_y. The other couplings are given in the first row of table (3.1), and the simulations were run with 100 bins, 10 000 equilibration sweeps and 10^5 Monte Carlo sweeps per bin. As we have seen from Chapter 7, this T^* is close to the critical temperature T_c of the system, so figure (8.1) is quite close to a phase diagram of the temperature T versus the next-nearest neighbour coupling J_y. The part of the plot below the line is the antiferromagnetic phase, and the part above is the paramagnetic phase.

We see that T^* decreases with increasing J_y. This seems fair: J_y is in competition with the nearest neighbour coupling in the y-direction, $J_1 = 2(J_{xy} + J_{yz})$, so increasing J_y should decrease the effective antiferromagnetic coupling $J_1 - J_y$ and thereby T^*. A close-up of figure (8.1) near $J_y = 0.67$ is given in figure (8.2)

Since the nearest-neighbour couplings J_1 in the y-direction are kept constant, we can use these data to find how T_c varies with $J_1 - J_y$. Looking at root mean squares of power-law fits, we find that $T_c \sim (J_1 - J_y)^{1.2}$ is a fairly good approximation. The details, together with a plot, are left in Appendix G for the interested reader. Of course, we keep in mind that our data are actually T^* and not T_c, so our treatment is somewhat rough.

We have studied the spin correlation function when increasing J_y. We see from figure (8.3) that the incommensurate phase appears at $J_y = 0.74$. The ratio between nearest- and next-nearest neighbour couplings is then

$$\frac{J_{xy} + J_{yz}}{J_y} = 1.81$$

which is not too different from what we found in section 6.2, but a bit larger. This means that the couplings are a bit closer to the border between incommensurability and commensurability given by Eq. (6.5).

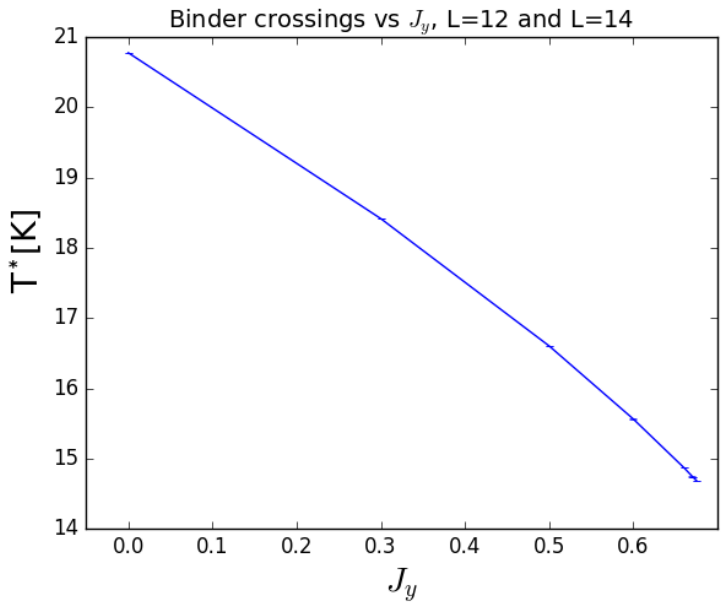

Figure 8.1: How the crossing temperature T^* for the Binder cumulants of $L = 12$ and $L = 14$ varies when we alter J_y in the model of Jensen et. al.

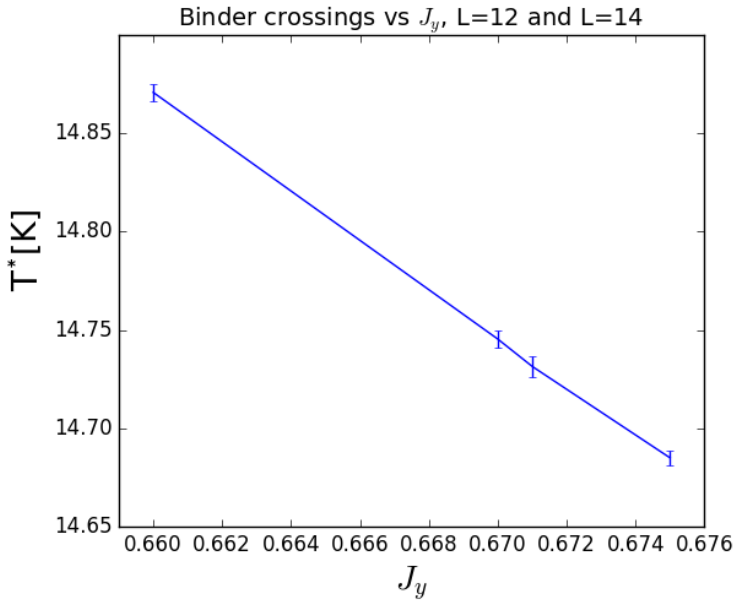

Figure 8.2: How the crossing temperature T^* for the Binder cumulants of $L = 12$ and $L = 14$ varies when we alter J_y in the model of Jensen et. al., near $J_y = 0.67$.

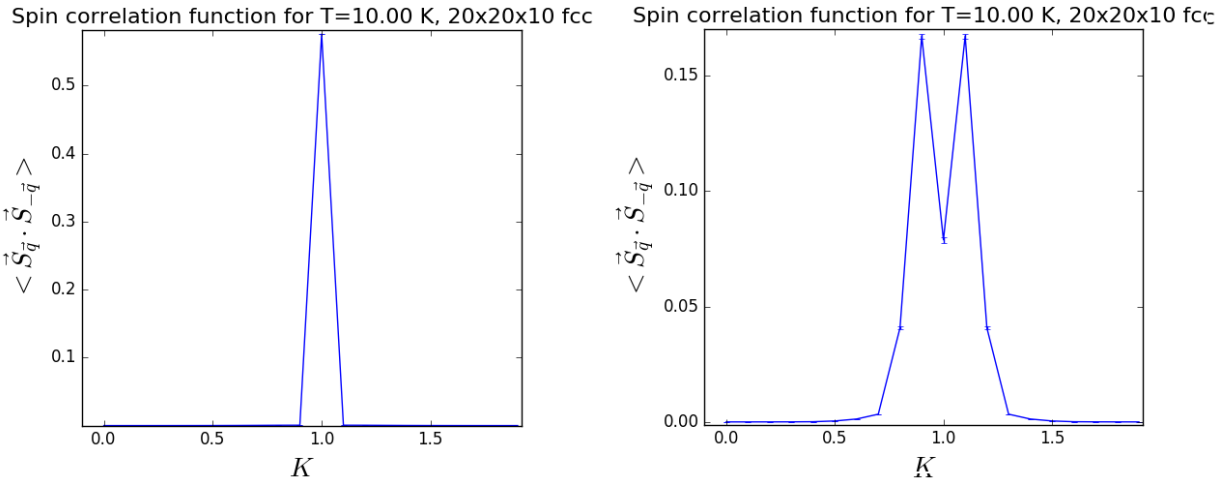

Figure 8.3: The spin correlation function using Jensen's model, but with $J_y = 0.73$ (left) and $J_y = 0.74$ (right). We see that the incommensurate peaks appear at $J_y = 0.74$.

8.2 A new set of couplings

The incommensurate phase was found by replacing $J_y = 0.67$ in Jensen's model with $J_y = 0.74$. Motivated by the relation $T_c \sim 2(J_{xy} + J_{yz}) - J_y$ found in the last subchapter, we insert for the couplings and use the critical temperature found in Chapter 7 to find a more exact relation. To see the incommensurate phase in a modified version of Jensen's model, we might set

$$J_{xy} = 0.46 \text{ meV}, \quad J_{yz} = 1.59 \text{ meV}, \quad J_y = 1.03 \text{ meV}$$

$$D_{an}^x = 0.34 \text{ meV}, \quad D_{an}^y = 1.82 \text{ meV}, \quad D_{an}^z = 0 \text{ meV}$$

in order to find the incommensurate-paramagnetic phase transition at roughly 21.8 K. These proposed couplings are derived in Appendix G. This modified model should be taken with a grain of salt: It was derived from Binder cumulant crossings T^* between L$=$ 12 and L$=$ 14 instead of T_c, the fit was not perfect, and more data points would have been useful. Furthermore, we have not verfied this model by any simulations, so it could be that the critical temperature actually is a bit different from 21.8 K.

Chapter 9

An evaluation of the models

9.1 Jensen and Jensen et. al.

The model of Jensen's thesis does fullfil the condition for incommensurability, Eq. (6.5), but it is just on the verge of doing so. In fact, rounding the couplings to two significant digits, the commensurate phase is lost to the antiferromagnetic one. Jensen argues that since the system just barely meets the condition, it is sensitive to small changes in the interactions that occur as the temperature changes[12]. However, he changes the single-ion anisotropy with temperature, but not the Heisenberg couplings (see table (3.2)). Our findings in table (C.9) of Appendix C suggests that the single-ion anisotropy should not be strong enough to force the system out of the incommensurate phase, so Jensen's approach in this regard is somewhat questionable.

A change in the couplings would have been a more convincing argument for the appearance of the commensurate-incommensurate phase. In figure (1.1), we see that the location of the incommensurate peaks in $LiNiPO_4$ move with temperature. Since a fixed relation between the nearest and next-nearest neighbour couplings leads to a fixed angle of rotation θ, changing the Heisenberg couplings would explain the movement of the peaks. The single-ion anisotropy, as we have shown in table (C.9) of Appendix B, would have to be much larger than Jensen states to explain that movement.

Moreover, we found the critical temperature to be about 14.7 K. Jensen has located two phase transitions in his thesis, found using scattering experiments: one for the commensurate-incommensurate phase transition at 20.8 K and one for the incommensurate-paramagnetic phase transition at 21.8 K[12]. Our critical temperature does not agree with any of these temperatures.

Doing simulations on the models of [12] and [13], we did not find the incommensurate phase, even though the former model obeys condition (6.5). Strictly speaking, that condition is for the incommensurate phase to be the ground state. Since we do not study zero temperature, we expect some thermal exitations in our system, forcing it out of the ground state. We have seen that the energies of the incommensurate and commensurate phases are almost the same, so the system might easily prefer a state closer

to the AF ordering. Had Jensen's couplings been further within the incommensurate regime given by (6.5), the IC ordering would have appeared, as we see from section 6.2.

9.2 Li et. al.

As we found in Chapter 6, the condition for incommensurability is not met in the model of Li et. al., so we are not surprised that the system exhibits no incommensurate phase. This is verified by figure (5.4) in section 7.2. The model therefore fails to exhibit a C-I phase transition.

9.3 Toft-Petersen et. al.

As seen in section 7.3, the model of Toft-Petersen et. al. did exhibit an incommensurate phase, but no antiferromagnetic phase. Hence, it has no commensurate-incommensurate phase transition.

Chapter 10

Conclusion and outlook

10.1 Conclusion

We did not find the commensurate-incommensurate phase transition for any of the suggested models. The models of Jensen et. al. and Li et. al. showed no incommensurate phase, just an antiferromagnetic one. The model of Toft-Petersen et. al., on the other hand, did exhibit an incommensurate phase, but not a commensurate one.

We found the ordering of the spins to depend on the ratio of nearest- and next-nearest neighbour couplings. Letting this ratio vary with temperature seems like the best way to model a commensurate-incommensurate phase transition. Figure (1.1) supports this notion as it shows moving incommensurate peaks. There is however the question of whether such a change of the couplings can be justified by thermal expansion. Jensen suggested that changing single-ion anisotropies could account for the phase transition[12]. Preliminary simulations of a spin chain did show the ordering wave vector depending on the size of the single-ion anisotropies, but not strongly enough to account for the drift of the peaks.

Jensen's model exhibited an antiferromagnetic-paramagnetic phase transition at 14.736 ± 0.007 K. This is lower than any of the phase transitions that Jensen suggested in his thesis, which were at about 20.8 K and 21.8 K[12]. We found the critical exponents of said model to be $\alpha = 0.22 \pm 0.06$, $\gamma = 1.2 \pm 0.3$ and $\nu = 0.50 \pm 0.13$. These are quite close to those of the three-dimensional Heisenberg and Ising systems, more so for Ising than Heisenberg. Since the Hamiltonian have an easy axis, this is not surprising.

The model of Jensen et. al. can be modified to exhibit an incommensurate phase by a relatively small change in the Heisenberg couplings. Rescaling the couplings, we can get an incommensurate-paramagnetic phase transition at about 21.8 K. A rough estimate is

$$J_{xy} = 0.46 \text{ meV}, \quad J_{yz} = 1.59 \text{ meV}, \quad J_y = 1.03 \text{ meV}$$
$$D_{an}^x = 0.34 \text{ meV}, \quad D_{an}^y = 1.82 \text{ meV}, \quad D_{an}^z = 0 \text{ meV}$$

but this model has not yet been verified by simulations. Furthermore, this modified model does not account for the commensurate-incommensurate phase transition in

$LiNiPO_4$, just like the model of Toft-Petersen et. al. From what we have seen, simulating the C-I phase transition is not possible with fixed Heisenberg couplings.

10.2 Outlook

We presented a modification to the Jensen et. al. model, one that should have an incommensurate-paramagnetic phase transition at roughly 21.8 K. The derivation of the couplings was somewhat rough, and we left the single-ion anisotropies as they were. Simulations should be done to determine the exact location of the phase transition, after which the model can be optimized.

We also mentioned that simulating a commensurate-incommensurate phase transition could be done by letting the nearest- and next-nearest couplings vary with temperature in a way that does not preserve their ratio. Thought has to be put into just how they vary with temperature, and such a project would probably involve delving deeper into the microscopic properties of the material.

Appendix A

Numerical methods

A.1 Monte Carlo and the Metropolis algorithm

A Monte Carlo algorithms

For systems of some size, the number of states is so huge that direct application of Eq. (2.3) is not tractable for most Hamiltonians. Instead, we must generate some smaller, yet representable collection of states to recreate the physics. In doing so, the probability distribution of the states must equal the Boltzmann distribution, which is closely related to Eq. (2.3). This is achieved by Monte Carlo simulations. Keep in mind that as long as we select some states randomly, there will be statistical errors, however small they may be [17].

To find a suitable way of drawing states for our system, we utilize two concepts of statistical dynamics [18]

1. A system is **ergodic** if it can reach any state of the system from any other state in a finite time interval.

2. The **ergodic hypothesis** states that for an ergodic system, the average over all possible states (the ensemble average) is equal to the time average. Beware that the time average must be taken over a sufficiently long time.

The ergodic hypothesis allows us to extract the information we want from the time-evolution of the system. We start off with one state and modify it time step by step according to the Boltzmann distribution. Ergodicity may be ensured by only updating the system by one spin flip at a time [17], which is the approach we will take in this thesis.

The updates in Monte Carlo simulations are based on **Markov processes**. In the context of Monte Carlo simulations, a Markov process will select a state ν at random, with a probability that depends only on ν and the current state μ of the system. This is called the transition probability $P(\mu \to \nu)$. As the system must be in *some* state after the transition, these transition probabilities must obey [17]

$$\sum_{\nu} P(\mu \to \nu) = 1 \tag{A.1}$$

where the system remaining in the same state, $\mu \to \mu$, is also a possibility. The Monte Carlo procedure makes use of several consecutive Markov processes, each starting with the result of the former. This is called a Markov chain [17].

To obtain a set of states obeying the Boltzmann distribution, we need to put further restrictions on the transition probabilities. We wish to study a system at equilibrium, the definition of which being that the system exits and enters a state μ at equal rate

$$\sum_{\nu} p_\mu P(\mu \to \nu) = \sum_{\nu} p_\nu P(\nu \to \mu) \tag{A.2}$$

where p_μ is the probability of the system being in state μ and $P(\mu \to \nu)$ is still the transition probability. To ensure the right distribution, we must employ a similar, but stricter condition, namely the **condition of detailed balance** [17]

$$p_\mu P(\mu \to \nu) = p_\nu P(\nu \to \mu) \tag{A.3}$$

Combining Eq.s (2.4) and (A.3) gives the following ratio for transition probabilities

$$\frac{P(\mu \to \nu)}{P(\nu \to \mu)} = \frac{p_\nu}{p_\mu} = e^{-\beta(E_\nu - E_\mu)} \tag{A.4}$$

which together with Eq. (A.1) is the foundation of all Monte Carlo algorithms [17]. Since we have explicitly inserted the Boltzmann probabilities, the states of the simulations belong to the correct distribution.

There is still a lot of freedom in choosing the transition probabilities, and some choices are more clever than others. In order to make our options more transparent, the transition probability can be separated into two factors, the selection probability $g(\mu \to \nu)$ (i.e. the probability to pick a specific state) and the acceptance ratio $A(\mu \to \nu)$ (the probability of accepting it): $P(\mu \to \nu) = g(\mu \to \nu)A(\mu \to \nu)$. An efficient algorithm is to be preferred, meaning we want the acceptance ratio to be as close to unity as possible while still obeying the conditions mentioned above.

The ratios must obey Eq. (A.4), meaning that

$$\frac{P(\mu \to \nu)}{P(\nu \to \mu)} = \frac{g(\mu \to \nu)A(\mu \to \nu)}{g(\nu \to \mu)A(\nu \to \mu)} = e^{-\beta(E_\nu - E_\mu)} \tag{A.5}$$

is fixed. We have a certain freedom in choosing $A(\mu \to \nu)$ and $A(\nu \to \mu)$, so we can set the largest to one and set the other so that the condition (A.5) holds. This is indeed what the Metropolis algorithm does.

B The Metropolis algorithm

Say our system is in a state μ, and it can make a transition to one of N_s available states ν. One way to construct the selection probabilities is to set them equal for all ν, i.e. $g(\mu \to \nu) = \frac{1}{N_s}$, and zero otherwise. This is the choice done by the Metropolis algorithm. As a consequence, the gs in Eq. (A.5) cancel, leaving a constraint on the acceptance ratio only. Additionally, we must have $A(\mu \to \nu) \leq 1$, as the acceptance rate is in fact a probability. The optimal way of fulfilling these conditions is to set [17]

$$A(\mu \to \nu) = \begin{cases} e^{-\beta(E_\nu - E_\mu)} & \text{if } E_\nu - E_\mu > 0 \\ 1 & \text{otherwise} \end{cases} \tag{A.6}$$

Outline of the implementation of the Metropolis algorithm

The steps in implementing the Metropolis algorithm is as follows [17]

1. Start with one state of the system.
2. Suggest another state by randomly flipping a spin in the system. Find the energy of the new state or the energy difference of the proposed update.
3. Accept or reject the new state according to Eq. (A.6).
4. Repeat a number of times to equilibrate the system.
5. Repeat a number of times while doing the relevant measurements on the system.
6. Optional: Repeat step 5. several times to divide the results into groups of data, hereby referred to as bins.

The spins to be flipped may be chosen at random, or the lattice may be traversed. We will adopt the former. Repeating step 2 and 3 N times, the spins have on average been subject to one suggested update. This is called a sweep [17]. In order to retain the accuracy for systems of different sizes, it is useful to measure the simulations in the number of Monte Carlo sweeps. Step 6 is not required in Monte Carlo simulations, but show that it is useful later on. Furthermore, it offers one way to find error estimates of quantities such as the heat capacity and magnetic susceptibility, which depend on averages of the energy and magnetization.

Correlations in the Metropolis algorithm

Obviously, two states separated by one possible spin flip will be strongly correlated, which is another reason to divide our measurements into lattice sweeps. Still, we will have correlations between subsequent states in the simulations. One way to remedy this is to only gather information every nth lattice sweep, but that would increase the computation time considerably [17]. Using bins, we average out this correlation to some extent.

Disadvantages with the Monte Carlo algoritms

Monte Carlo algorithms are inefficient at low temperatures since the acceptance ratio decrases with temperature, so a lot of simulation time will be spent on rejecting suggested transitions. Of course, a physical system at low temperatures will spend a lot of time in the ground state, but reproducing this in a simulation is hardly time-efficient [17]. For single-flip algorithms, there will be little difference between subsequent states.

Another issue at low temperatures is the chance to get stuck in metastable states. At low temperatures, we expect the system to be close to the ground state. In the equilibration process, the system might however reach a local minima of the energy on its path to the ground state. In that case, the system must cross an energy barrier in order to approach the ground state. In single-flip algorithms, the suggested new state will be closely related to the current one. Each proposed move will then require an energy cost. With a low acceptance rate, very few moves will be accepted, and we will stay in the vicinity of the metastable state for a very long time.

A.2 General error estimation

Since the Monte Carlo procedure draws random states, there will always be some statistical error in the result [17]. We will use the spread of the data to estimate the uncertainty. For quantities such as the energy, we retrieve the measurement at every step and find the average over each bin. When the Monte Carlo procedure is done, we use the bin averages to find the total average and the standard deviation. This kind of error estimate is called **the standard deviation in the mean**. Mathematically, it is given by[24]

$$\sigma_m = \left(\frac{1}{N_{\text{bins}}(N_{\text{bins}}-1)} \sum_{i=1}^{N_{\text{bins}}} \left(\bar{x}(i) - \bar{x}_{\text{tot}}\right)^2 \right)^{1/2} \tag{A.7}$$

where $\bar{x}(i)$ is the average of the measurements done in bin i, $\bar{x}_{\text{tot}}$ is the average over all measurements and N_{bins} is the number of bins [24]. In contrast, **the standard deviation of single measurements** reads

$$\sigma_s = \left(\frac{1}{N-1} \sum_{i=1}^{N} \left(x(i) - \bar{x}\right)^2 \right)^{1/2} \tag{A.8}$$

where $x(i)$ is measurement i, N is the number of measurements and $\bar{x}$ is the average of the measurements. This equation applies when we don't bin our data. σ_s will not decrease when we perform more measurements: Our precision is the same, so our $x(i)$'s will have the same spread and add up to compensate for the larger N in the exponent. Eq. (A.7) obviously gives the better error estimate: The bin averages will be closer to the total average than $x(i)$, so the sum will be smaller. In fact the two are related by $\sigma_m = \sigma_s/\sqrt{N_b}$[24], where N_b is the number of values in each bin. The standard deviation in the mean can thus be made smaller by increasing the bin size.

Sometimes, a quantity cannot be measured directly, but must be inferred from some other quantities. Imagine we want to give an error estimate of the quantity $Z = Z(A, B, \cdots, M)$, where $A, B, \cdots M$ are independent of each other. In that case, the standard deviation in Z can be found from the standard deviation of $A, B, \cdots M$ by[24]

$$\sigma_Z = \left(\left(\frac{\partial Z}{\partial A} \sigma_A \right)^2 + \left(\frac{\partial Z}{\partial B} \sigma_B \right)^2 + \cdots + \left(\frac{\partial Z}{\partial M} \sigma_M \right)^2 \right)^{1/2} \tag{A.9}$$

A.3 The Bootstrap method

The Bootstrap method is what is called a **resampling method**. In short, it uses data from the simulations to randomly generate other data sets, and use these to obtain a good estimate of the averages and errors. It is widely regarded to be a good method for generating error estimates[17].

The procedure can be implemented as follows [17]

1. Organize the original data into a list of N_d estimates of the relevant variable.
2. Draw, with replacement, N_d elements of the list at random.
3. Use these to find the desired quantity.
4. Repeat step 2. and 3. N_B number of times.
5. Derive an error estimate from the N_B different values of step 3.

As we draw with replacement, some elements will appear multiple times in the new data set, while others do not appear at all. We will find the error estimate from the standard deviation of the N_B data points according to Eq. (A.8). The Bootstrap method is particularly useful when we consider quantities like the magnetic susceptibility [17]. These are functions of two variables that are related, so we cannot find the error estimate from Eq. (A.9). We could of course find the magnetic susceptibility once for every bin, but the Bootstrap method proves much more effective. When doing complicated procedures like extracting the crossings of the Binder cumulant, the error estimations simplifies considerably if we use the Bootstrap method to generate a set of crossings. This is in fact what we will do in the finite-size scaling analysis.

Appendix B

Verification of the code

B.1 The two-particle pure Heisenberg chain with periodic boundary conditions

To help verify our program, we consider the classical Heisenberg Hamiltonian for a spin chain:

$$H = J \sum_{\langle ij \rangle} \mathbf{S}_i \cdot \mathbf{S}_j \tag{B.1}$$

where $\langle ij \rangle$ indicates that the sum are over nearest neighbours. The spins have unit length.

With two spins and periodic boundary conditions, the Hamiltonian becomes

$$H = 2J(\mathbf{S}_1 \cdot \mathbf{S}_2) \tag{B.2}$$

We can decompose the vectors according to Eq. (H.1). Combining with Eq. (B.2), we obtain an energy

$$E = 2J\left(\sin\theta_1 \cos\phi_1 \sin\theta_2 \cos\phi_2 + \sin\theta_1 \sin\phi_1 \sin\theta_2 \sin\phi_2 + \cos\theta_1 \cos\theta_2\right) \tag{B.3}$$

Since our spins are classical, the partition function can be determined by insertion in Eq. (2.5)

$$Z = \int d\theta_1 d\phi_1 d\theta_2 d\phi_2 \sin\theta_1 \sin\theta_2 e^{-\beta E(\theta_1,\phi_1,\theta_2,\phi_2)}$$

Where $\theta_1, \theta_2 \in [0, \pi]$ and $\phi_1, \phi_2 \in [0, 2\pi]$. The sines enter from the Jacobi determinants as usual. We simplify the exponent by express the energy in terms of the relative angle $\theta_{rel} = \mathbf{S}_1 \cdot \mathbf{S}_2$. The angles θ_1, ϕ_1 and ϕ_2 fixes the other angles of rotation in our problem. The integral now takes a much more pleasant form

$$Z = \int d\theta_1 d\phi_1 d\theta_2 d\phi_2 \sin\theta_1 \sin\theta_2 e^{-2\beta J \cos\theta_2}$$

Where we have renamed θ_{rel} to θ_2. We perform the integration:

$$\begin{aligned} Z &= \int_{-1}^{1} d\cos\theta_1 \int_0^{2\pi} d\phi_1 \int_0^{2\pi} d\phi_2 \int_{-1}^{1} d\cos\theta_2 e^{-2\beta J\cos\theta_2} \\ &= \frac{8\pi^2}{\beta J}\frac{1}{2}\left(e^{-2\beta J} - e^{-2\beta J}\right) = 8\pi^2\frac{\sinh(2\beta J)}{\beta J} \end{aligned}$$

The energy

The energy can be found from Eq. (2.8)

$$\langle E\rangle = -\frac{\partial}{\partial\beta}\ln(Z) = -\frac{\partial}{\partial\beta}\ln\left(\frac{8\pi^2}{\beta J}\sinh(2\beta J)\right) = \frac{1}{\beta} - 2J\frac{\cosh(2\beta J)}{\sinh(2\beta J)} \tag{B.4}$$

The heat capacity

The heat capacity can be found from the energy by Eq. (2.9):

$$C_V = -\frac{1}{kT^2}\frac{\partial\langle E\rangle}{\partial\beta} = -k\beta^2\frac{\partial}{\partial\beta}\left[\frac{1}{\beta} - 2\frac{\cosh(2\beta J)}{\sinh(2\beta J)}\right] = k - k\beta^2\frac{(2J)^2}{\sinh^2(2\beta J)} \tag{B.5}$$

The N-particle chain with periodic boundary conditions

The bonds set the spins' orientation relative to each other. However, once the relative orientations are set, we still have a freedom of rotating them in the plane. In the antiferromagnetic ground state, for instance, the neighbours are antiparallel. However, they might be oriented along any axis: the x-, y- or z-axis, or any linear combination thereof. Clearly, we need one θ setting the entire configuration. In other words, if we want to simplify Z through the relative angle, we can only have $N-1$ bonds. The periodic chain has N bonds, meaning that we have to use open boundary conditions if we want a neat expression for the energy and the heat capacity.

Results vs theory

In figures (B.1) to (B.3), we have plotted the theoretical predictions together with the data from our simulations. We see that there is a good agreement between theory and simulations. All results were generated using 10000 equilibration sweeps, 1000 sweeps per bin and 100 bins.

The paramagnetic phase which occurs at high temperatures (low β) is characterized by random spins and thus no net magnetization. Due to the randomness, however, we don't expect the squared magnetization $\langle m_x^2\rangle$ to be exactly zero, especially not for a small system. This explains the low, non-zero value of $\langle m_x^2\rangle$ at low β in figure (B.4).

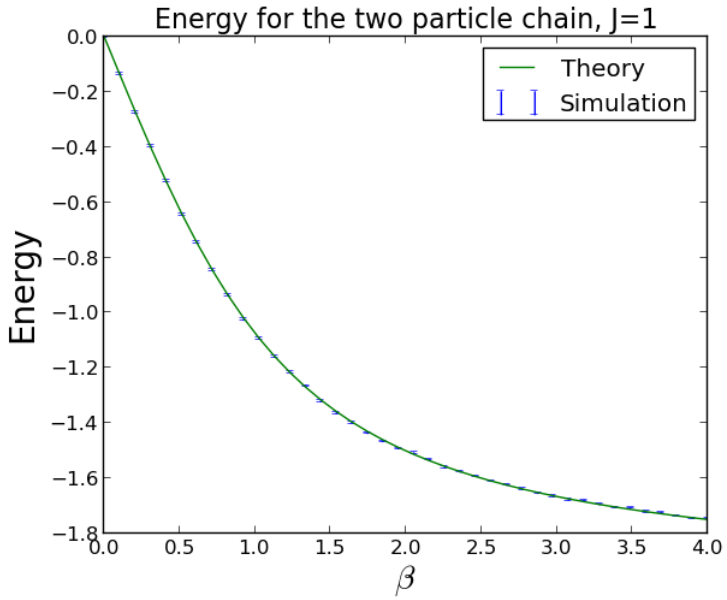

Figure B.1: The energy of a two-particle periodic antiferromagnetic Heisenberg chain as a function of inverse temperature, β, found analytically (green line, Eq. (B.4)) and by simulations (error bars). The agreement is good.

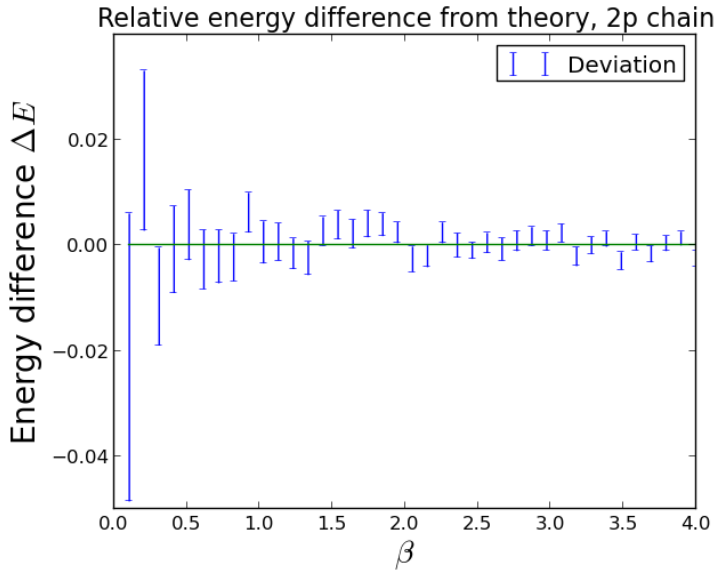

Figure B.2: The plot shows the relative deviation between the calculated energy (Eq. (B.3)) and the results from simulations for a two-particle periodic antiferromagnetic chain as a function of inverse temperature, β. The error bars are centered at the relative energy difference. They are the same as in Fig. (B.1), but divided by the calculated energy. The agreement is good.

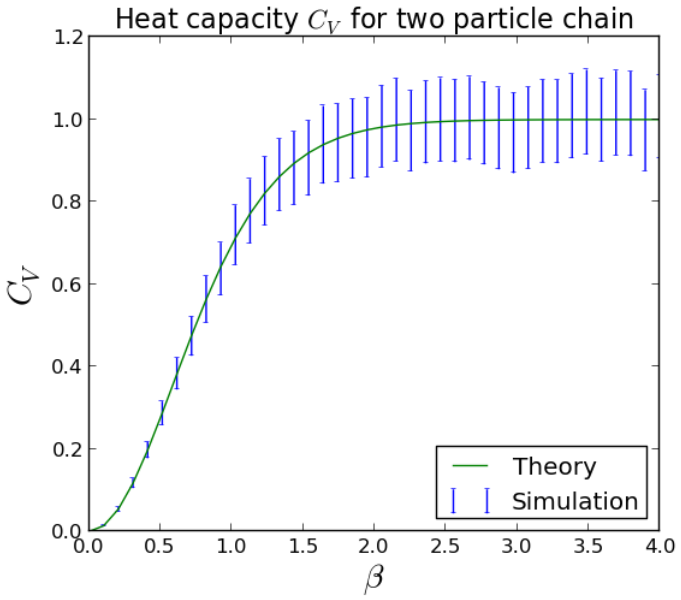

Figure B.3: The heat capacity of a two-particle periodic antiferromagnetic Heisenberg chain as a function of inverse temperature, β, found analytically (green line, Eq. (B.5)) and by simulations (error bars). The agreement is good.

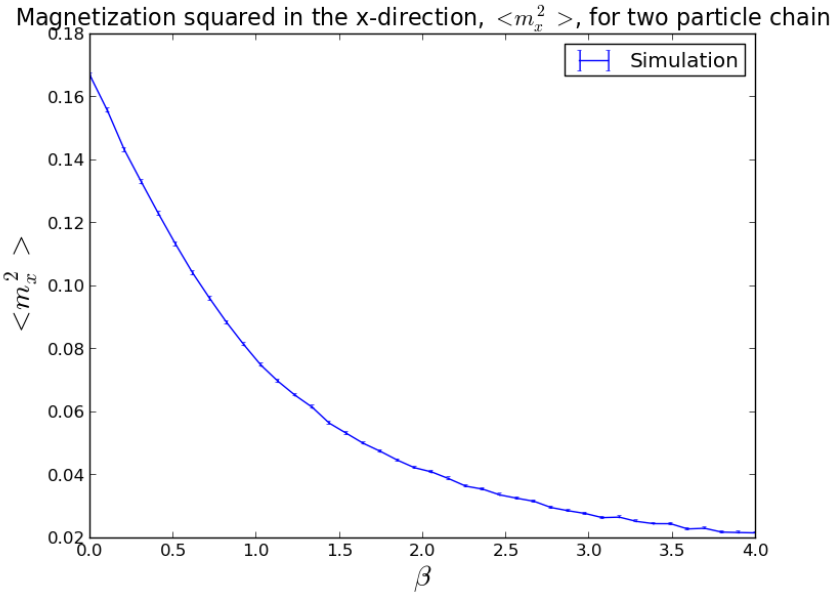

Figure B.4: The squared magnetization in the x-direction of a two-particle periodic antiferromagnetic Heisenberg chain versus inverse temperature, β.

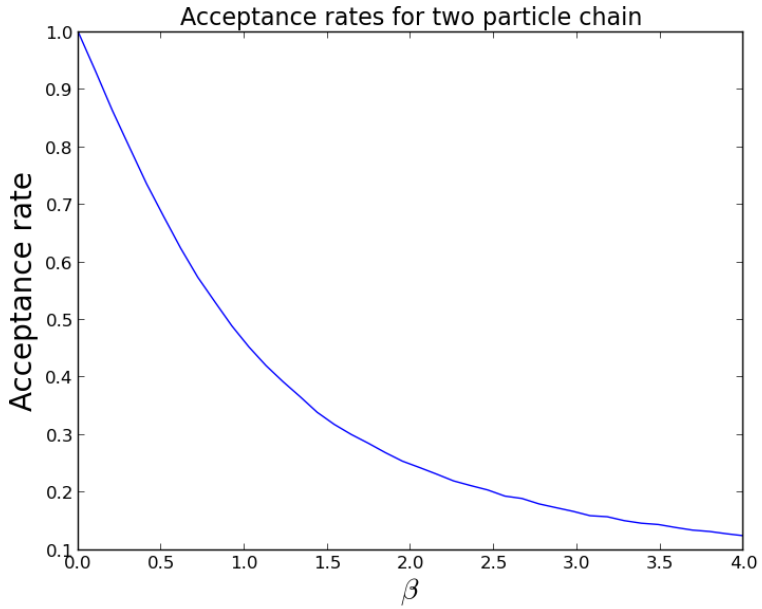

Figure B.5: The acceptance rate of a two-particle periodic antiferromagnetic Heisenberg chain versus inverse temperature, β.

The antiferromagnetic phase also exhibits zero net magnetization. However, the antiferromagnetic phase *favours* antiparallel spins, so we expect $\langle m_x^2 \rangle$ to be *exactly* zero at zero temperature. This explains why $\langle m_x^2 \rangle$ falls off to zero in figure (B.4). There is no anisotropy in the system, so the situation will be no different for $\langle m_y^2 \rangle$ and $\langle m_z^2 \rangle$. As expected, the plots were just about identical to figure (B.4), so they were not included in this thesis.

As a supplement, figure (B.5) shows how the acceptance rate decreases with temperature.

A The N-particle pure Heisenberg chain with open boundary conditions

The partition function

The partition function of a N spin chain with open boundary conditions becomes

$$Z = \int_{-1}^{1} d\cos\theta_1 \left(\int_0^{2\pi} d\phi \right)^N \left(\int_{-1}^{1} d\cos\theta e^{-\beta J \cos\theta} \right)^{N-1}$$

$$= \frac{2(2\pi)^N}{(-\beta J)^{N-1}} \left(e^{-\beta J} - e^{\beta J} \right)^{N-1}$$

$$= \frac{(4\pi)^N}{(\beta J)^{N-1}} \sinh^{N-1}(\beta J)$$

The energy

We differentiate

$$\langle E \rangle = -\frac{\partial}{\partial \beta} \ln(Z) = -\frac{\partial}{\partial \beta} \left[\ln\left(\frac{(4\pi)^N}{J^{N-1}} \right) - \ln(\beta^{N-1}) + \ln(\sinh^{N-1}(\beta J)) \right]$$

$$= (N-1)J \left[\frac{1}{\beta J} - \frac{\cosh(\beta J)}{\sinh(\beta J)} \right] \tag{B.6}$$

The heat capacity

Again, we utilize:

$$C_V = -k\beta^2 \frac{\partial}{\partial \beta} \langle E \rangle$$

$$= -(N-1)Jk\beta^2 \left[-\frac{1}{\beta^2 J} + J \frac{\cosh^2(\beta J) - \sinh^2(\beta J)}{\sinh^2(\beta J)} \right]$$

$$= (N-1)k \left[1 - \frac{(\beta J)^2}{\sinh^2(\beta J)} \right] \tag{B.7}$$

where we have used that $\cosh^2 x - \sinh^2 x = 1$.

Figures (B.6) to (B.9) compares analytical and numerical values of the energy and heat capacity for a four spin chain and the energy for a 50 spin chain. Theory and results agree well. The graph of the squared magnetization $\langle m_x^2 \rangle$ in figure (B.10) behaves as expected, and so does the acceptance rate in figure (B.11). The simulations were run using 10000 equilibration sweeps and 1000 lattice sweeps per bin with 100 bins for the four-particle case, and 10000 sweeps for the 50-particle case.

B The modified Bessel functions of the first kind

In our treatment of the two-particle partition function, the modified Bessel functions of the first kind will appear. Recognizing them simplifies our computations significantly, as they are readily handled by MATLAB. We will mainly make use of the zeroth order modified Bessel functions, but the second one will appear as well. Some useful identities are listed below.

The n-th order modified Bessel function of the first kind is[28]

$$\int_0^{2\pi} e^{-z\cos x} \cos(n\theta) dx = 2\pi I_n(z) \tag{B.8}$$

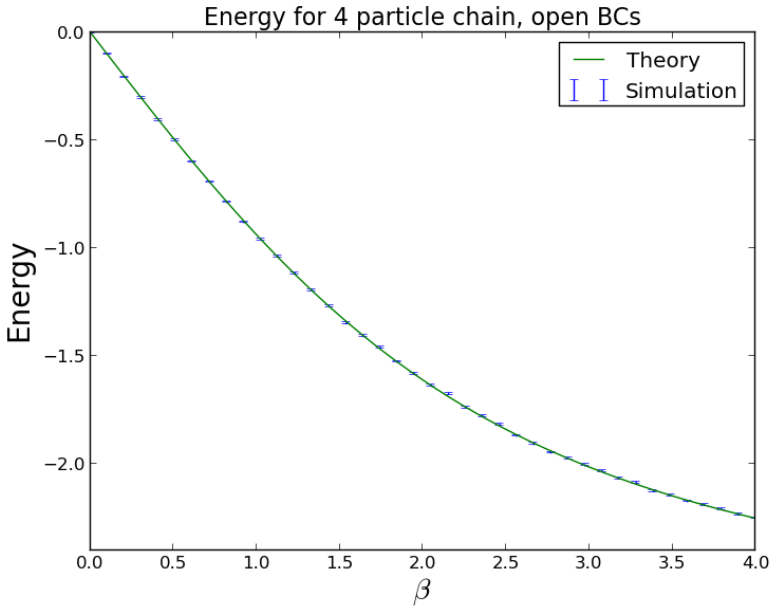

Figure B.6: The energy of a four-particle open antiferromagnetic Heisenberg chain as a function of inverse temperature, β, found analytically (green line) and by simulations (error bars). The agreement is good.

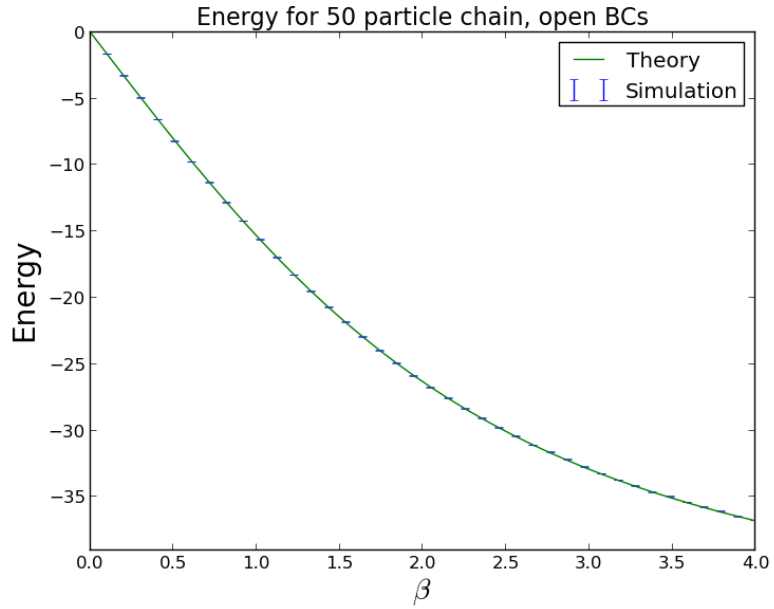

Figure B.7: The energy of a 50-particle open antiferromagnetic Heisenberg chain as a function of inverse temperature, β, found analytically (green line) and by simulations (error bars). The agreement is good.

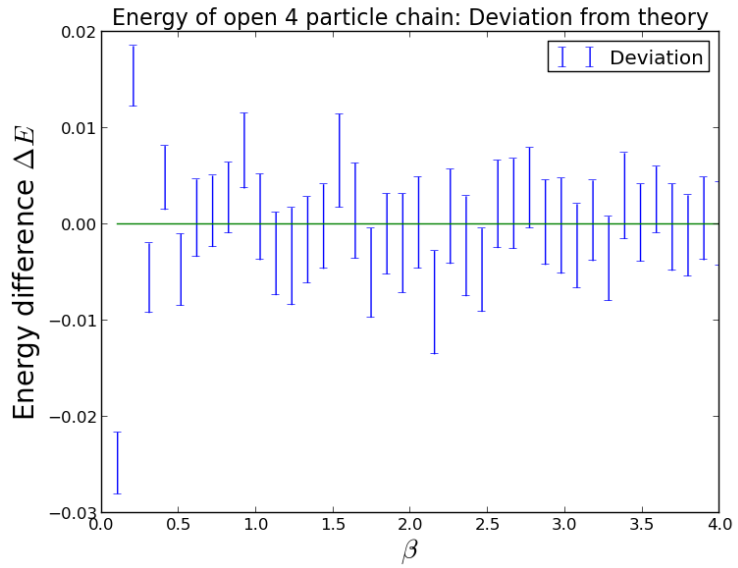

Figure B.8: The plot shows the relative deviation between the calculated energy and the results from simulations for a four-particle open AF chain as a function of β. The error bars are centered at relative energy difference. They are the same as in Fig. (B.6), but divided by the calculated energy. The agreement is good.

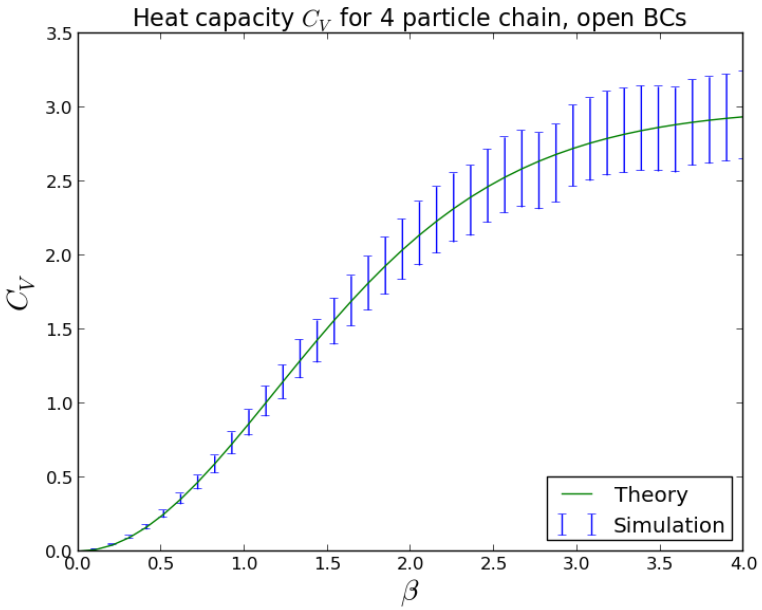

Figure B.9: The heat capacity of a four-particle open antiferromagnetic Heisenberg chain as a function of inverse temperature, β, found analytically (green line) and by simulations (error bars). The agreement is good.

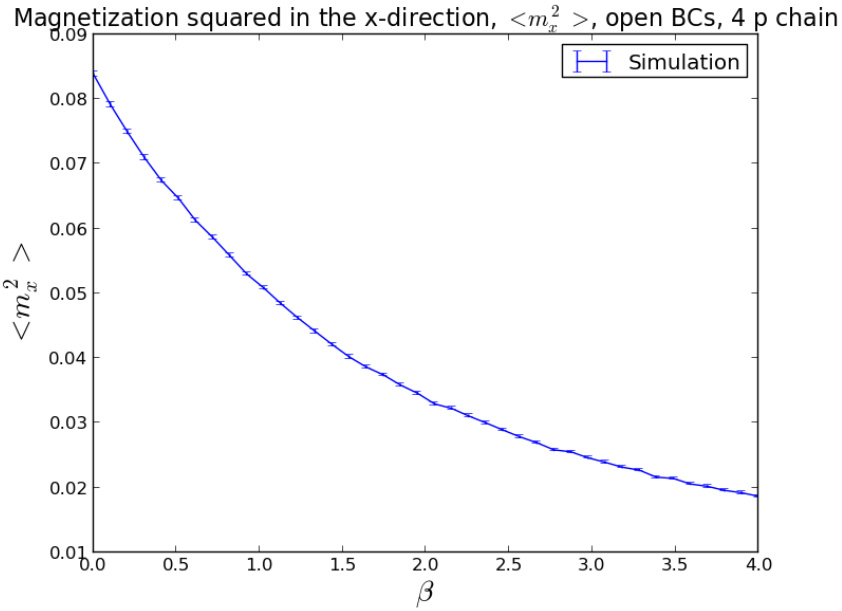

Figure B.10: The squared magnetization in the x-direction of a four-particle open antiferromagnetic Heisenberg chain as a function of inverse temperature, β. The simulations were run using 10000 equilibration sweeps and 1000 lattice sweeps per bin with 100 bins.

The zeroth order function thus simplifies to

$$\int_0^{2\pi} e^{-z\cos x} dx = 2\pi I_0(z) \tag{B.9}$$

The derivative of I_0 is related to I_1 by[19]

$$\frac{\partial I_0(z)}{\partial z} = zI_1(z) \tag{B.10}$$

C The integral of a periodic integrand

Given a periodic function $f(x) = f(x+a)$, we want to show that the integral is invariant under a shift of the integration limits. We denote the indefinite integral as $F(x) = \int f(x)dx$ for brevity.

$$\int_b^{b+a} f(x)dx = \int_0^a f(x)dx \quad \forall \ b \tag{B.11}$$

$$A = \int_b^{b+a} f(x)dx - \int_0^a f(x)dx = (F(b+a) - F(b)) - (F(a) - F(0))$$

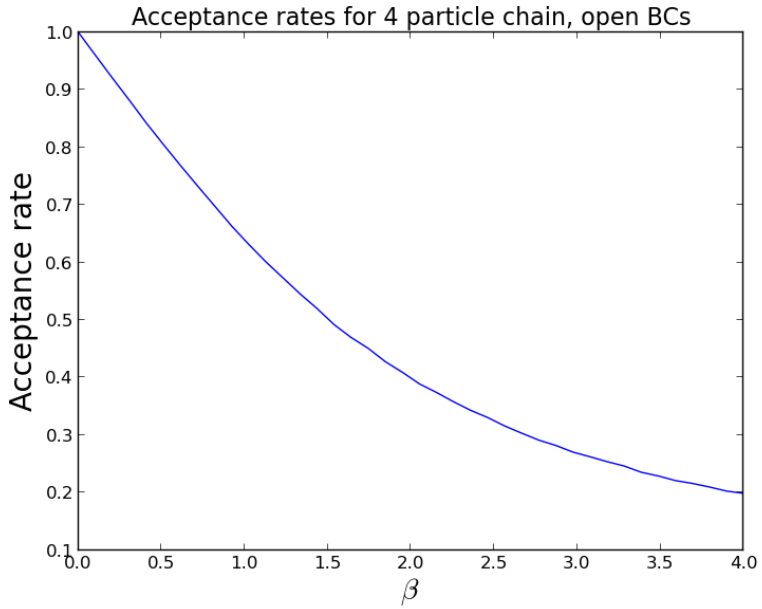

Figure B.11: The acceptance rate of a four-particle open antiferromagnetic Heisenberg chain as a function of inverse temperature, β. The simulations were run using 10000 equilibration sweeps and 1000 lattice sweeps per bin with 100 bins.

$$= F(b+a) - F(a) - (F(b) - F(0)) = \int_a^{b+a} f(x)dx - \int_0^b f(x)dx$$

We introduce a change of variable for the first integral, $t = x - a$ or $x = t + a$.

$$A = \int_0^b f(t+a)dt - \int_0^b f(x)dx = \int_0^b (f(x+a) - f(x))dx = \int_0^b 0dx = 0$$

So Eq. (B.11) holds.

B.2 The two-particle Heisenberg chain with single-ion anisotropy

In order to test our code, we find the energy of a two-particle Heisenberg chain with single-ion anisotropy in the z-direction. This chapter is based on calculations done by Ellen Fogh in a personal note[8]. Our Hamiltonian is as follows:

$$H = J\mathbf{S}_1 \cdot \mathbf{S}_2 + D\left((S_1^z)^2 + (S_2^z)^2\right) \tag{B.12}$$

$$= J\cos\theta + D\left(\cos^2\theta_1 + \cos^2\theta_2\right)$$

Where D is the single-ion anisotropy in the z-direction. The relative angle θ is related to the other quantities by

$$\begin{aligned}\cos\theta &= \sin\theta_1\cos\phi_1\sin\theta_2\cos\phi_2 + \sin\theta_1\sin\phi_1\sin\theta_2\sin\phi_2 + \cos\theta_1\cos\theta_2 \\ &= \sin\theta_1\sin\theta_2(\cos\phi_1\cos\phi_2 + \sin\phi_1\sin\phi_2) + \cos\theta_1\cos\theta_2\end{aligned}$$

Using

$$\begin{aligned}\sin\phi_1\sin\phi_2 &= \frac{1}{2}(\cos(\phi_1-\phi_2) - \cos(\phi_1+\phi_2)) \\ \cos\phi_1\cos\phi_2 &= \frac{1}{2}(\cos(\phi_1+\phi_2) + \cos(\phi_1-\phi_2))\end{aligned}$$

The expression in the paranthesis simplifies

$$J\mathbf{S}_1\cdot\mathbf{S}_2 = J\sin\theta_1\sin\theta_2\cos(\phi_1-\phi_2) + J\cos\theta_1\cos\theta_2$$

Which yields a simpler Hamiltonian

$$H = J\left[\sin\theta_1\sin\theta_2\cos(\phi_1-\phi_2) + \cos\theta_1\cos\theta_2\right] + D\left(\cos^2\theta_1 + \cos^2\theta_2\right)$$

Giving rise to the partition function

$$\begin{aligned}Z = &\int_0^\pi d\theta_1\sin\theta_1\int_0^{2\pi}d\phi_1\int_0^\pi d\theta_2\sin\theta_2\int_0^{2\pi}d\phi_2 \\ &\times\exp\left[-\beta\left(J\left[\sin\theta_1\sin\theta_2\cos(\phi_1-\phi_2) + \cos\theta_1\cos\theta_2\right] + D\left(\cos^2\theta_1+\cos^2\theta_2\right)\right)\right]\end{aligned}$$

As the integral only depends on the difference between the ϕ's, Fogh performs a change of integration variable:

$$\begin{array}{cc} x = \phi_1 - \phi_2 & x(\phi_2 = 0) = \phi_1 \\ dx = -d\phi_2 & x(\phi_2 = 2\pi) = \phi_1 - 2\pi \end{array} \tag{B.13}$$

$$\begin{aligned}Z = &\int_0^\pi d\theta_1\int_0^\pi d\theta_2\sin\theta_1\sin\theta_2\exp\left[-\beta\left(J\cos\theta_2\cos\theta_2 + D\left(\cos^2\theta_1+\cos^2\theta_2\right)\right)\right] \\ &\times\int_0^{2\pi}d\phi_1\int_{\phi_1}^{\phi_1-2\pi}(-dx)\exp\left[-\beta J\sin\theta_1\sin\theta_2\cos x\right]\end{aligned}$$

But the integrand is a periodic function of 2π, so the integral is invariant under any shift of the integration limit. This is evident from Eq. (B.11) with $a = x$ and $b = \phi_1$. Since the limits of the last integral does not depend on ϕ_1, and we can perform the penultimate integral right away:

Table B.1: A comparison between simulations and theoretical output from a MATLAB script for the two-particle Heisenberg chain with $J = 1$ and $D^z_{an} = 2$. Periodic boundary conditions were enforced.

β	E_{theory}	$E_{short\ sim}$	$E_{long\ sim}$	Within $\Delta E_{short\ sim}$	Within $\Delta E_{long\ sim}$
0.5	0.3577	0.3581±0.0020	0.3583±0.0006	Yes	Yes
1.0	-0.4216	-0.4233±0.0025	-0.4213±0.0008	Yes	Yes
2.0	-1.2015	-1.1988±0.0021	-1.2021±0.0007	No	Yes
10.0	-1.8487	-1.8488±0.0009	-1.8492±0.0003	Yes	No
50.0	-1.9699	-1.9699±0.0005	-1.9699±0.0001	Yes	Yes

$$Z = 2\pi \int_0^\pi d\theta_1 \int_0^\pi d\theta_2 \sin\theta_1 \sin\theta_2 \exp\left[-\beta\left(J\cos\theta_2\cos\theta_2 + D\left(\cos^2\theta_1 + \cos^2\theta_2\right)\right)\right]$$
$$\times \int_{-2\pi}^{0} dx \exp\left[-\beta J \sin\theta_1 \sin\theta_2 \cos x\right]$$

The last expression can be expressed as the zeroth order modified Bessel function, given by Eq. (B.9), simplifying our expression somewhat:

$$Z = 4\pi^2 \int_0^\pi d\theta_1 \int_0^\pi d\theta_2 \sin\theta_1 \sin\theta_2 \exp\left[-\beta\left(J\cos\theta_2\cos\theta_2 + D\left(\cos^2\theta_1 + \cos^2\theta_2\right)\right)\right]$$
$$\times I_0(J\sin\theta_1\sin\theta_2) \tag{B.14}$$

As $E = -\frac{1}{Z}\frac{\partial Z}{\partial \beta}$, we need to find $\frac{\partial Z}{\partial \beta}$. Utilizing Eq. (B.10) yields

$$\frac{dZ}{\partial\beta} = 4\pi^2 \int_0^\pi d\theta_1 \int_0^\pi d\theta_2 \sin\theta_1 \sin\theta_2 \exp\left[-\beta\left(J\cos\theta_2\cos\theta_2 + D\left(\cos^2\theta_1 + \cos^2\theta_2\right)\right)\right]$$
$$\times\Big(-\left[J\cos\theta_1\cos\theta_2 + D(\cos^2\theta_1 + \cos^2\theta_2)\right] I_0(J\sin\theta_1\sin\theta_2)$$
$$+ J\sin\theta_1\sin\theta_2 I_1\left(J\beta\sin\theta_1\sin\theta_2\right)\Big) \tag{B.15}$$

The expression for the energy is clearly complicated, and writing it in full is not neccessary. Feeding Eq.s (B.14) and (B.15) into MATLAB and combining the results according to Eq. (2.8), we have an exact expression for the energy. Note that this can be done with both periodic and open boundary conditions. Periodic boundary conditions will produce an additional factor of four to be multiplied with J, which may easily be handled by our program.

The energy for some values of β are listed in tables (B.1) through (B.4) together with the results from simulations. The numerical output were found to agree with the calculated result within the standard deviation for roughly two thirds of the cases, as is

Table B.2: A comparison between simulations and theoretical output from MATLAB for the two-particle Heisenberg chain with $J = 1$ and $D_{an}^{z} = 5$. Periodic boundary conditions were enforced.

β	E_{theory}	E_{sim}	Within ΔE_{sim}
0.5	0.9602	0.9597±0.0114	Yes
1.0	-0.3397	-0.3397±0.0012	Yes
2.0	-1.2136	-1.2140±0.0008	Yes
10.0	-1.8490	-1.8489±0.0004	Yes
50.0	-1.9700	-1.9698±0.0002	Yes

Table B.3: A comparison between simulations and theoretical output from MATLAB for the two-particle Heisenberg chain with $J = 1$ and $D_{an}^{z} = 7$. Open boundary conditions were enforced.

β	E_{theory}	E_{sim}	Within ΔE_{sim}
0.5	1.6638	1.6626±0.0011	No
1.0	0.5768	-0.3397±0.0012	Yes
2.0	-0.1861	-1.2140±0.0008	Yes
10.0	-0.8483	-1.8489±0.0004	Yes
50.0	-0.9699	-1.9698±0.0002	Yes

Table B.4: A comparison between simulations and theoretical output from MATLAB for the two-particle Heisenberg chain with $J = 1$ and $D_{an}^{z} = 0.1$. Open boundary conditions were enforced.

β	E_{theory}	E_{sim}	Within ΔE_{sim}
0.5	-0.0982	-0.0984±0.0002	Yes
1.0	-0.2483	-0.2484±0.0002	Yes
2.0	-0.4753	-0.4751±0.0002	Yes
10.0	-0.8597	-0.8596±0.0002	Yes
50.0	-0.9699	-0.9696±0.0001	No

expected. All simulations were run with 10000 equilibration sweeps and 10000 Monte Carlo sweeps per bin. With the exception of the short simulations in table (B.1), which contained 100 bins, all simulations contained 1000 bins.

B.3 The two-particle Heisenberg chain with DM interaction in the z-direction

We want to study the two-particle classical Heisenberg chain with Dzyaloshinskii-Moriya (DM) interaction in the z-direction, i.e. $D^x_{DM} = D^y_{DM} = 0$, $D^z_{DM} = D$. Because of the cross product in the DM interaction, periodic boundary conditions will lead to cancellation in the two-particle case. Consequently, we will only consider open boundary conditions. The Hamiltonian in question is therefore:

$$H = J\mathbf{S}_1 \cdot \mathbf{S}_2 + \mathbf{D}_{DM} \cdot (\mathbf{S}_1 \times \mathbf{S}_2) \tag{B.16}$$

We calculate the cross product:

$$\mathbf{S}_1 \times \mathbf{S}_2 = \begin{vmatrix} \hat{i} & \hat{j} & \hat{k} \\ S_1^x & S_1^y & S_1^z \\ S_2^x & S_2^y & S_2^z \end{vmatrix} = \hat{i}(S_1^y S_2^z - S_1^z S_2^y) - \hat{j}(S_1^z S_2^x - S_1^x S_2^z) + \hat{k}(S_1^x S_2^y - S_1^y S_2^x)$$

So:

$$\mathbf{D}_{DM} \cdot (\mathbf{S}_1 \times \mathbf{S}_2) = D^x_{DM}(S_1^y S_2^z - S_1^z S_2^y) + D^y_{DM}(S_1^x S_2^z - S_1^z S_2^x) + D^z_{DM}(S_1^x S_2^y - S_1^y S_2^x)$$

When we express the spin components by the polar angles by Eq. (H.1), the Dzyaloshinskii-Moriya term becomes:

$$\begin{aligned} \mathbf{D}_{DM} \cdot (\mathbf{S}_1 \cdot \mathbf{S}_2) = D^x_{DM}(&\sin\theta_1 \cos\theta_2 \sin\phi_1 - \sin\theta_2 \cos\theta_1 \sin\phi_2) \\ +D^y_{DM}(&\sin\theta_2 \cos\theta_1 \cos\phi_2 - \sin\theta_1 \cos\theta_2 \cos\phi_1) \\ +D^z_{DM}(&\sin\theta_1 \sin\theta_2 \cos\phi_1 \sin\phi_2 - \sin\theta_1 \sin\theta_2 \cos\phi_2 \sin\phi_1) \end{aligned}$$

Now, our motivation for only studying the D^z_{DM}-term becomes clear: It is the only term where we can factor out $\sin\theta_1 \sin\theta_2$, i.e. separating the θ's and ϕ's:

$$\begin{aligned} A &= D^z_{DM}(\sin\theta_1 \sin\theta_2 \cos\phi_1 \sin\phi_2 - \sin\theta_1 \sin\theta_2 \cos\phi_2 \sin\phi_1) \\ &= D^z_{DM}(\sin\theta_1 \sin\theta_2(\cos\phi_1 \sin\phi_2 - \cos\phi_2 \sin\phi_1)) \end{aligned}$$

Where A is used for convenience. We use the well-known trigonometric identities together with $D^z_{DM} = D$ to rewrite

$$A = -D \sin\theta_1 \sin\theta_2 \sin(\phi_1 - \phi_2)$$

The Heisenberg term was found in the previous chapter. Our Hamiltonian, in turn, becomes

$$H = \sin\theta_1 \sin\theta_2 \left[J\cos(\phi_1 - \phi_2) - D\sin(\phi_1 - \phi_2)\right] + J\cos\theta_1 \cos\theta_2 \tag{B.17}$$

The partition function is

$$Z = \int_0^{\pi} d\theta_1 \sin\theta_1 \int_0^{2\pi} d\phi_1 \int_0^{\pi} d\theta_2 \sin\theta_2 \int_0^{2\pi} d\phi_2$$
$$\times \exp\Big[-\beta\Big(\sin\theta_1 \sin\theta_2 \left[J\cos(\phi_1 - \phi_2) - D\sin(\phi_1 - \phi_2) \right] + J\cos\theta_1 \cos\theta_2 \Big) \Big]$$

Retracing the steps of the previous chapter, we obtain

$$Z = 2\pi \int_0^{\pi} d\theta_1 \int_0^{\pi} d\theta_2 \sin\theta_1 \sin\theta_2 \exp\left[-J\beta\cos\theta_2 \cos\theta_2 \right]$$
$$\times \int_{-2\pi}^{0} dx \exp\left[-\beta \sin\theta_1 \sin\theta_2 (J\cos x - D\sin x) \right]$$

We want to absorb the sine into the cosine in order to get the integral on a known form. We set $\alpha \equiv \beta \sin\theta_1 \theta_2 J$ and massage the expression in the exponent

$$-\alpha\Big(\cos x - (D/J)\sin x \Big) = -\alpha \left(\cos x - \frac{\sin\nu}{\cos\nu} \sin x \right)$$
$$= -\frac{\alpha}{\cos\nu}(\cos x \cos\nu - \sin x \sin\nu) = -\frac{\alpha}{\cos\nu}\cos(x+\nu)$$

To find the factor in front of the cosine, we must express $\frac{1}{\cos\nu}$ in terms of known quantities

$$\tan^2\nu = \frac{\sin^2\nu}{\cos^2\nu} = \frac{1-\cos^2\nu}{\cos^2\nu} = \frac{1}{\cos^2\nu} - 1$$
$$\frac{1}{\cos\nu} = \sqrt{\tan^2\nu + 1} = \sqrt{(D/J)^2 + 1}$$

So the factor becomes

$$\tilde{\alpha} = \frac{\alpha}{\cos\nu} = \beta \sin\theta_1 \sin\theta_2 J\sqrt{(D/J)^2+1} = \beta \sin\theta_1 \sin\theta_2 \sqrt{D^2 + J^2}$$

In turn

$$Z = 2\pi \int_0^{\pi} d\theta_1 \int_0^{\pi} d\theta_2 \sin\theta_1 \sin\theta_2 e^{-J\beta\cos\theta_1\cos\theta_2} \int_0^{2\pi} dx e^{-\tilde{\alpha}\cos(x+\nu)}$$

We can change variables to $u = x + \nu$, yielding

$$\int_0^{2\pi} dx e^{-\tilde{\alpha}\cos(x+\nu)} = \int_{\nu}^{2\pi+\nu} du e^{-\tilde{\alpha}\cos u} = \int_0^{2\pi} du e^{-\tilde{\alpha}\cos u}$$

once again due to the symmetry of the integrand. But this integral is the zeroth order modified Bessel function of the first kind, Eq. (B.9), as a function of $\tilde{\alpha}$. We simplify our expression to the point where we have to calculate it numerically

Table B.5: Theoretical and numerical results for a two-particle chain with $J = 1$, $D^z_{DM} = 1$.

β	E_{theory}	E_{sim}	Within ΔE?	Within $2\Delta E$?	Within $3\Delta E$?
0.5	-0.27070	-0.26967±0.00234	Yes	Yes	Yes
1.0	-0.50460	-0.50432±0.00227	Yes	Yes	Yes
2.0	-0.81740	-0.81537±0.00233	Yes	Yes	Yes
10.0	-1.26527	-1.27065±0.00206	No	No	Yes
50.0	-1.38418	-1.38490±0.00090	Yes	Yes	Yes

Table B.6: Theoretical and numerical results for a two-particle chain with $J = 1$, $D^z_{DM} = 0.1$.

β	E_{theory}	E_{sim}	Within ΔE?	Within $2\Delta E$?
0.5	-0.16503	-0.16484±0.00019	No	Yes
1.0	-0.31500	-0.31493±0.00018	Yes	Yes
2.0	-0.54026	-0.54032±0.00018	Yes	Yes
10.0	-0.90335	-0.90345±0.00011	Yes	Yes
50.0	-0.98343	-0.98341±5.10e-05	Yes	Yes

$$Z = 4\pi^2 \int_0^\pi d\theta_1 \int_0^\pi d\theta_2 \sin\theta_1 \sin\theta_2 e^{-J\beta\cos\theta_1\cos\theta_2} I_0(\beta \sin\theta_1 \sin\theta_2 \sqrt{J^2 + D^2})$$

The energy can then be calculated by $E = -\frac{1}{Z}\frac{\partial Z}{\partial \beta}$

$$\begin{aligned}\frac{\partial Z}{\partial \beta} = 4\pi^2 \int_0^\pi d\theta_1 \int_0^\pi d\theta_2 \sin\theta_1 \sin\theta_2 e^{-J\beta\cos\theta_1\cos\theta_2} \\ \times[-J\cos\theta_1\cos\theta_2 I_0(\beta\sin\theta_1\sin\theta_2\sqrt{J^2+D^2}) \\ +\sqrt{J^2+D^2}\sin\theta_1\sin\theta_2 I_1(\beta\sin\theta_1\sin\theta_2\sqrt{J^2+D^2})]\end{aligned}$$

Where we have used Eq. (B.10) once more. So we calculate Z and $\frac{\partial Z}{\partial \beta}$ numerically and use them to find the energy.

Tables (B.5) trough (B.8) compares the results generated by MATLAB to the output from our simulations. In the first table, the simulations were run with 1000 Monte Carlo sweeps per bin and 100 bins. For the rest of them, the simulations were run with 100000 Monte Carlo sweeps per bin and 100 bins. The answers agree within one standard deviation in roughly two thirds of the cases.

Table B.7: Theoretical and numerical results for a two-particle chain with $J = 2$, $D^z_{DM} = 5$.

β	E_{theory}	E_{sim}	Within ΔE?	Within $2\Delta E$?
0.5	-2.76778	-2.76683±0.00117	Yes	Yes
1.0	-3.90343	-3.90508±0.00116	No	Yes
2.0	-4.62977	-4.62982±0.00078	Yes	Yes
10.0	-5.23493	-5.23418±0.00038	No	Yes
50.0	-5.35516	-5.35503±0.00019	Yes	Yes

Table B.8: Theoretical and numerical results for a two-particle chain with $J = 1$, $D^z_{DM} = 10$.

β	E_{theory}	E_{sim}	Within ΔE?	Within $2\Delta E$?
0.5	-7.04189	-7.03885±0.00214	No	Yes
1.0	-8.53628	-8.53635±0.00157	Yes	Yes
2.0	-9.29660	-9.29654±0.00115	Yes	Yes
10.0	-9.89975	-9.89982±0.00057	Yes	Yes
50.0	-10.01987	-10.01962±0.00023	No	Yes

B.4 Implementation of the next-nearest neighbours

We have mentioned that there is no frustration in the sytem if the nearest neighbour coupling J_1 and the next-nearest coupling J_2 are both ferromagnetic, because both favour parallel alignment of the spins. Figure (B.12) shows a nearest neighbour ferromagnetic chain, while figure (B.13) and (B.14) shows the next-nearest neighbour ferromagnetic coupling on a chain of and even and an odd number of particles. We note that we get two decoupled chains for an even number of spins. The spins in each chain must therefore align, but there is no coupling forcing the two chains to align with each other. For the odd chain, on the other hand, the periodic boundary condition couples the two chains so that all spins should ve parallel. This means that we can compare the next-nearest neighbour ferromagnet with an odd number of spins to the nearest neighbour ferromagnet to test our implementation.

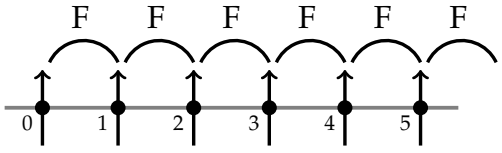

Figure B.12: A six-particle periodic chain with nearest neighbour ferromagnetic interactions. At low-temperatures, the spins will tend to align in order to minimize the energy.

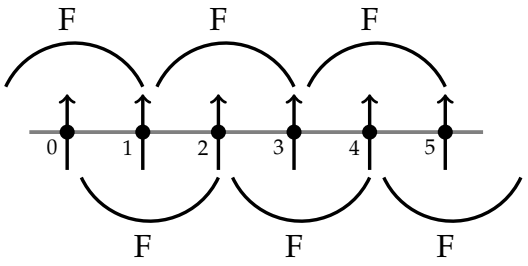

Figure B.13: A six-particle periodic chain with next-nearest neighbour ferromagnetic interactions. We see that not all spins will be coupled: Those we have denoted with even numbers (0,2,4) are only coupled amongst themselves, and the same goes for those denoted by odd numbers (1,3,5). Thus, we effectively have two decoupled chains. In each chain, the spins are aligned, but there is no coupling forcing the two chains to align.

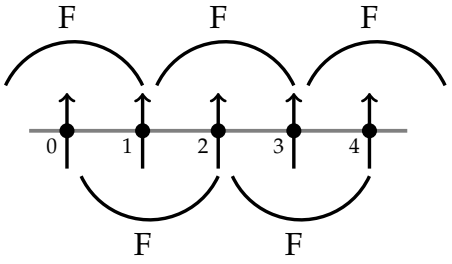

Figure B.14: A five-particle periodic chain with next nearest neighbour ferromagnetic interactions. We see that all spins have to be coupled. In the low-temperature regime, then, the ferromagnetic coupling will cause all spins to align.

Table B.9: Neighbours and next-nearest neighbours of the spins for smaller N-particle chains. n.n. stands for nearest neighbours and n.n.n. stands for next nearest neighbours.

$N = 3$			$N = 4$			$N = 5$		
Spin	n.n.	n.n.n.	Spin	n.n.	n.n.n.	Spin	n.n.	n.n.n.
0	2, 1	1, 2	0	3, 1	2, 2	0	4, 1	3, 2
1	0, 2	2, 0	1	0, 2	3, 3	1	0, 2	4, 3
2	1, 0	0, 1	2	1, 3	0, 0	2	1, 3	0, 4
			3	2, 0	1, 1	3	2, 4	1, 0
						4	3, 0	2, 1

Table B.10: A comparison between the energy for the nearest neighbour ferromagnetic chain and the next-nearest neighbour ferromagnetic chain with different particle numbers N and seeds. N is odd in order for the two systems to be comparable in the low-temperature regime. n.n. denotes the nearest neighbour system, while n.n.n. denotes the next-nearest neighbour system. The numbers have been rounded to a few significant digits after processing ($|E_{n.n.} - E_{n.n.n.}|$ is calculated and then rounded).

N, seed	$E_{n.n.}$	$\Delta E_{n.n.}$	$E_{n.n.n.}$	$\Delta E_{n.n.n.}$	$\lvert E_{n.n.} - E_{n.n.n.}\rvert$	Agree within ΔE?
5, s59	-4.5970	$3.4 \cdot 10^{-3}$	-4.5948	$3.6 \cdot 10^{-3}$	$2.2 \cdot 10^{-3}$	Yes
5, s79	-4.5922	$3.6 \cdot 10^{-3}$	-4.5990	$4.0 \cdot 10^{-3}$	$6.8 \cdot 10^{-3}$	Yes
7, s59	-6.3887	$5.4 \cdot 10^{-3}$	-6.4006	$5.3 \cdot 10^{-3}$	$1.2 \cdot 10^{-2}$	No (within $2\Delta E$)
7, s79	-6.3969	$4.6 \cdot 10^{-3}$	-6.3974	$4.6 \cdot 10^{-3}$	$5.2 \cdot 10^{-3}$	Yes
9, s59	-8.1904	$6.4 \cdot 10^{-3}$	-8.1683	$5.6 \cdot 10^{-3}$	$2.2 \cdot 10^{-2}$	No (within $2\Delta E$)
9, s79	-8.1886	$6.6 \cdot 10^{-3}$	-8.1974	$6.1 \cdot 10^{-3}$	$8.8 \cdot 10^{-3}$	Yes
11, s59	-9.9910	$7.3 \cdot 10^{-3}$	-9.9863	$7.4 \cdot 10^{-3}$	$4.7 \cdot 10^{-3}$	Yes
11, s79	-9.9902	$7.5 \cdot 10^{-3}$	-9.9835	$7.6 \cdot 10^{-3}$	$6.7 \cdot 10^{-3}$	Yes

Neighbours

Table (B.9) shows the nearest and next-nearest bonds for chains of three, four and five particles. For $N = 3$, the system is so small that the nearest and the next-nearest neighbours are the same. Another weird effect occurs for $N = 4$, where the next-nearest neighbour interaction couples each spin to itself. $N = 5$ is the first non-trivial case of the next-nearest neighbour coupling: All the spins are connected by it, and the couplings are different from other terms in the Hamiltonian.

The next-nearest neighbours generated by the program were checked using pen and paper, and everything agreed.

Numerical results

We have compared the nearest neighbour ferromagnetic chain and the next-nearest neighbour ferromagnetic chain with an odd number of particles for $N = 5, 7, 9, 11$. $N = 3$ yielded identical results since the couplings are the same, as seen in table (B.9). The result of the other simulations we performed is listed in table (B.10). The table shows a good agreement between the two models.

B.5 Fourier transformed spins and the spin correlation function

In order to test if the spin correlation function is implemented correctly, calculations on simple systems were performed. The spin correlation function have been computed numerically and analytically for a N-particle chain, assuming periodicity in the reciprocal lattice. The output of FFTW have been scaled by N to in order to agree with Eq. (2.39). Analytic calculations have been performed on chains of up to 5 spins. We will make plenty of use of list (3).

The one dimensional version of (H.4) is

$$\tilde{S}_k^z = \frac{1}{N}\sum_j S_j^z e^{-\frac{2\pi i k j}{N}} \tag{B.18}$$

The chain with parallel spins

To verify our implementation, write out Eq. (B.18) for chains of different length with parallel spins, i.e. $\mathbf{S}_i = 1$, and compare to the output of our code. The Fourier transformed spins are listed in (B.11). For further comparison, we utilize Eq. (2.43) to obtain $\langle \tilde{S}_j^z \tilde{S}_{-j}^z \rangle$, listed in table (B.12). The numerical and analytical results agree in both cases.

Table B.11: Table of the Fourier transforms of the spins, $\tilde{S}_i^z N$, when the spin configuration is set to $S_i^z = 1$. This is the output from the function fftw_plan_dft_r2c from FFTW. Note that it is scaled by N for readability. The output is given as complex numbers on the form of $(a, b) = a + ib$. The right table lists the difference between the numerical and analytical results. The agreement between theory and numerics is superb.

Output	$\tilde{S}_0^z N$	$\tilde{S}_1^z N$	$\tilde{S}_2^z N$	Diff	$\tilde{S}_0^z N$	$\tilde{S}_1^z N$	$\tilde{S}_2^z N$
$N = 2$	(1,0)	(0,0)	–	$N = 2$	(0,0)	(0,0)	–
$N = 3$	(1,0)	(0,0)	–	$N = 3$	(0,0)	(0,0)	–
$N = 4$	(1,0)	(0,0)	(0,0)	$N = 4$	(0,0)	(0,0)	(0,0)
$N = 5$	(1,0)	(0, 0)	(0, 0)	$N = 5$	(0,0)	(0,0)	(0,0)

Table B.12: The numerical results of the spin correlation function $\langle \tilde{S}^z_{-i} \tilde{S}^z_i \rangle$ for different spins i and system sizes N. The spin configuration is again set to $S^z_i = 1$.

Output	$\langle \tilde{S}^z_0 \tilde{S}^z_0 \rangle$	$\langle \tilde{S}^z_{-1} \tilde{S}^z_1 \rangle$	$\langle \tilde{S}^z_{-2} \tilde{S}^z_2 \rangle$	Diff	$\langle \tilde{S}^z_0 \tilde{S}^z_0 \rangle$	$\langle \tilde{S}^z_{-1} \tilde{S}^z_1 \rangle$	$\langle \tilde{S}^z_{-2} \tilde{S}^z_2 \rangle$
$N = 2$	1	0	–	$N = 2$	0	0	–
$N = 3$	1	0	–	$N = 3$	0	0	–
$N = 4$	1	0	0	$N = 4$	0	0	0
$N = 5$	1	0	0	$N = 5$	0	0	0

Table B.13: Exact values of $\cos(2\pi n/5)$ and $\sin(2\pi n/5)$. θ is the angle.

θ	0	$2\pi/5$	$4\pi/5$	$6\pi/5$	$8\pi/5$	2π
$\cos(\theta)$	1	$\frac{1}{4}\left(-1+\sqrt{5}\right)$	$-\frac{1}{4}\left(1+\sqrt{5}\right)$	$-\frac{1}{4}\left(1+\sqrt{5}\right)$	$\frac{1}{4}\left(-1+\sqrt{5}\right)$	1
$\sin(\theta)$	0	$\frac{1}{4}\sqrt{10+2\sqrt{5}}$	$\frac{1}{4}\sqrt{10-2\sqrt{5}}$	$-\frac{1}{4}\sqrt{10-2\sqrt{5}}$	$-\frac{1}{4}\sqrt{10+2\sqrt{5}}$	0

The chain with alternating spins

Due to the rather boring results for $S^z_i = 1$, we have calulated the spin correlation function with $S^z_i = (-1)^i$, i.e. alternating spins. The output of the transformed spins agrees with the theory as listed in table (B.14). The same holds for the spin correlation function, listed in table (B.15). The results were calculated exactly, and the difference was found by subtracting the exact answer from the numerical one in the test code. Note that all the Fourier transformed spins can indeed be found exactly. To fit the table, the

Table B.14: Table of the Fourier transforms of the spins, $\tilde{S}^z_i N$, when we have alternating spins. This is the output from the function fftw_plan_dft_r2c from FFTW. Note that it is scaled by N for readability. The output is given as complex numbers on the form of $(a, b) = a + ib$. The right table lists the difference between the numerical and analytical results. The agreement between theory and numerics is superb.

Output	$\tilde{S}^z_0 N$	$\tilde{S}^z_1 N$	$\tilde{S}^z_2 N$	Diff	$\tilde{S}^z_0 N$	$\tilde{S}^z_1 N$	$\tilde{S}^z_2 N$
$N = 2$	(0,0)	(2,0)	–	$N = 2$	(0,0)	(0,0)	–
$N = 3$	(1,0)	(1,1.73)	–	$N = 3$	(0,0)	(0,0)	–
$N = 4$	(0,0)	(0,0)	(4,0)	$N = 4$	(0,0)	(0,0)	(0,0)
$N = 5$	(1,0)	(1, 0.73)	(1, 3.08)	$N = 5$	(0,0)	(0, 0)	(0, 0)

Table B.15: The numerical results of the spin correlation function $\langle \tilde{S}^z_{-i} \tilde{S}^z_i \rangle$ for different spins i and system sizes N. The spin configuration is again set to $S^z_i = (-1)^i$.

Output	$\langle \tilde{S}^z_0 \tilde{S}^z_0 \rangle$	$\langle \tilde{S}^z_{-1} \tilde{S}^z_1 \rangle$	$\langle \tilde{S}^z_{-2} \tilde{S}^z_2 \rangle$	Diff	$\langle \tilde{S}^z_0 \tilde{S}^z_0 \rangle$	$\langle \tilde{S}^z_{-1} \tilde{S}^z_1 \rangle$	$\langle \tilde{S}^z_{-2} \tilde{S}^z_2 \rangle$
$N = 2$	0	1	$-$	$N = 2$	0	0	$-$
$N = 3$	1/9	4/9	$-$	$N = 3$	0	0	$-$
$N = 4$	0	0	1	$N = 4$	0	0	0
$N = 5$	0.04	0.0611	0.4189	$N = 5$	0	0	0

following round-offs have been performed

$$\sqrt{3} \approx 1.73$$

$$\frac{1}{2}\left(\sqrt{10+2\sqrt{5}} - \sqrt{10-2\sqrt{5}}\right) \approx 0.73$$

$$\frac{1}{2}\left(\sqrt{10+2\sqrt{5}} + \sqrt{10-2\sqrt{5}}\right) \approx 3.08$$

All of which entered by non-canceling sinusoidal terms in Eq. (B.18). The exact expressions for $\sin(\frac{2\pi n}{5})$ are listed in table (B.13), found by the help of [29] and basic trigonometric identities.

A The correlation function for the NxN lattice: Theory vs. results

For a general two-dimensional lattice, the Fourier transforms of the spins becomes:

$$\tilde{S}^z_{k_1,k_2} = \frac{1}{L_1 L_2} \sum_{n_1=0}^{L_1-1} \sum_{n_2=0}^{L_2-1} S^z_{n_1,n_2} e^{-2\pi i \left(\frac{k_1 n_1}{L_1} + \frac{k_2 n_2}{L_2}\right)} \tag{B.19}$$

The 2x2 lattice

As we are working with a lattice of more than one dimension, we want to test our implementation of two- and three-dimensional lattices as well. We start with the simplest case first and study the 2×2-lattice. Due to the small system size, all Fourier transformed spins will be purely real, as seen from list (3). The analytical results for a few cases are listed in table (B.16), together with a comparison with the computational results. Once again, the exact answers were subtracted from the numerical answers in the test code. We see that there is no disagreement except a round-off error in one instance.

Table B.16: Table of different spin configurations for the 2×2 lattice and the resulting Fourier transforms. To improve the readability, the Fourier transforms are multiplied by the number of particles (namely 4). The first eight columns indicates the input and the analytical results, while the last column gives the largest difference between the analytical and numerical results.

$S^z_{0,0}$	$S^z_{0,1}$	$S^z_{1,0}$	$S^z_{1,1}$	$N\tilde{S}^z_{0,0}$	$N\tilde{S}^z_{0,1}$	$N\tilde{S}^z_{1,0}$	$N\tilde{S}^z_{1,1}$	Largest error
1	1	1	1	4	0	0	0	0
1	-1	-1	-1	-2	2	2	2	0
-1	1	1	1	2	-2	-2	-2	0
1	-1	1	1	2	2	-2	2	0
1	-1	-1	1	0	0	0	4	0
1	1	-1	-1	0	0	4	0	0
0.1	0.2	0.3	0.4	1	-0.2	-0.4	0	$3 \cdot 10^{-17}$

Table B.17: Table of the Fourier transforms of the spins of a 3×3 lattice. The spins are increasing in magnitude, with $S^z_{i,j} = 0.1(3i + j + 1)$ and $i, j \in [0, 2]$. To improve the readability, the Fourier transforms are multiplied by the number of particles (namely 9). Complex numbers are given as $(a, b) = a + ib$.

	$N\tilde{S}^z_{0,0}$	$N\tilde{S}^z_{0,1}$	$N\tilde{S}^z_{1,0}$
Theory	(4.5, 0)	(-0.45,0.259808)	(-1.35, 0.779423)
Numerical	(4.5,0)	(-0.45,0.259808)	(-1.35,0.779423)
	$N\tilde{S}^z_{1,1}$	$N\tilde{S}^z_{1,2}$	$N\tilde{S}^z_{2,0}$
Theory	(0,0)	(0,0)	(-1.35,-0.779423)
Numerical	$(-1.1 \cdot 10^{-16}, -4.1 \cdot 10^{-17})$	$(5.6 \cdot 10^{-17}, 5.5 \cdot 10^{-17})$	(-1.35, -0.779423)

Table B.18: Table of the Fourier transforms of the spins of a $2 \times 2 \times 2$ lattice. The spins are increasing in magnitude, with $S^z_{i,j} = 0.1(4i + 2j + k + 1)$ and $i, j, k \in [0, 2]$. To improve the readability, the Fourier transforms are multiplied by the number of particles (namely 8). Very small numbers are given by order of magnitude only.

	$N\tilde{S}^z_{0,0,0}$	$N\tilde{S}^z_{0,0,1}$	$N\tilde{S}^z_{0,1,0}$	$N\tilde{S}^z_{0,1,1}$	$N\tilde{S}^z_{1,0,0}$	$N\tilde{S}^z_{1,0,1}$	$N\tilde{S}^z_{1,1,0}$	$N\tilde{S}^z_{1,1,1}$
Theory	3.6	-0.4	-0.8	0	-1.6	0	0	0
Numerical	3.6	-0.4	-0.8	10^{-16}	-1.6	10^{-16}	10^{-16}	10^{-16}

The 3x3 lattice

We know that fftw only stores $L_1 \times L_2/2$ elements due to symmetry considerations, reducing the output to a six-element array in our case. By said symmetries, we see that $\tilde{S}^z_{0,1} = \tilde{S}^{z*}_{0,2}$, $\tilde{S}^z_{1,1} = \tilde{S}^{z*}_{2,2}$ and $\tilde{S}^z_{1,2} = \tilde{S}^{z*}_{2,1}$.

The analytical results for the case of $S^z_{i,j} = 0.1(3i + j + 1)$ are listed in table (B.17), together with a comparison with the computational results. The results are fine except some round-off errors. Round-off errors are dangerous when evolving a quantity. In finding the spin correlation function in our Monte Carlo procedure, the Fourier transform is done anew for each Monte Carlo step, so we needn't worry. Some round-off errors will be negative and other positive, so there should be some cancellation going on. Since the spin correlation function is averaged, large round-off errors not be accumulated anyway.

B The correlation function for the 2x2x2 lattice: Theory vs. results

The 3-dimensional Fourier transform becomes:

$$\tilde{S}^z_{k_1,k_2,k_3} = \frac{1}{L_1 L_2 L_3} \sum_{n_1=0}^{L_1-1} \sum_{n_2=0}^{L_2-1} \sum_{n_3=0}^{L_3-1} S^z_{n_1,n_2,n_3} e^{-2\pi\left(\frac{n_1 k_1}{L_1} + \frac{n_2 k_2}{L_2} + \frac{n_3 k_3}{L_3}\right)} \tag{B.20}$$

Eq. (B.20) can easily be used to test the implementation of FFTW for the three-dimensional lattice. Due to the small size of the system we once again know the transformed spins to be real. The analytical results for a few cases are listed in table (B.18), together with a comparison with the computational results. Again, the results agree up to roud-off errors.

C The ordering wave vector for a chain

We will investigate the ordering wave vector for an N-particle chain for various couplings. Often, we will resort to studying a 5- or 6-particle cain in order to ease our understanding. Note that systems of odd and even particle number will in practice exhibit different ordering wave vectors, as we only have a discrete set of ordering wave

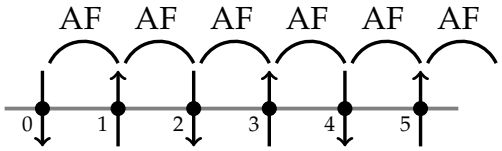

Figure B.15: An even-particle chain with nearest-neighbour antiferromagnetic interactions (in the ground state). The first spin is free to point in any direction, but that would fix the other spins.

vectors to choose from. Referring to Eq. (2.32) and identifying $L_1 = N$ and $\mathbf{b}_1 = \frac{2\pi}{a}\hat{i}$ from Eq. (2.29), our $\mathbf{q}$-vectors takes the values

$$\mathbf{q} = \frac{2\pi k}{Na}\hat{i}$$

where N is the number of particles, a is the grid length and $k = 0, \cdots, N-1$. We shall see that $q = \frac{\pi}{a}$ is a preferred ordering wave vector for many systems, but it only appears in our discrete set if N is even. For odd N, the different values of q will compete for the largest contribution.

The ordering wave vector q is the one that maximizes the spin correlation function:

$$\langle \mathbf{S}_q \mathbf{S}_{-q} \rangle = \frac{1}{N^2} \sum_j \sum_k \mathbf{S}_j \mathbf{S}_k e^{iq\Delta r_{jk}} \tag{B.21}$$

where Δr_{jk} is the separation between the spins at site j and site k. To get an intuition of the ordering wave vector, it is often enough to look at the contribution to (B.21) from $j = 0$:

$$N^2 \langle \mathbf{S}_q \mathbf{S}_{-q} \rangle_{j=0} = \mathbf{S}_0 \mathbf{S}_0 + \mathbf{S}_0 \mathbf{S}_1 e^{iqa} + \mathbf{S}_0 \mathbf{S}_2 e^{2iqa} + \cdots \tag{B.22}$$

where we have inserted for Δr_{jk}.

The simulations in this section were run for $\beta = 1000$ with 10 000 equilibration sweeps, 1000 bins and 10 000 lattice sweeps per bin.

The nearest-neighbour antiferromagnet

The even-particle chain

Figure (B.15) shows one possible configuration of the ground state of a nearest-neighbour antiferromagnetic chain with an even number of particles. The configuration is fixed up to an overall rotation of the spins. Our spin correlation function becomes:

$$N^2 \langle \mathbf{S}_q \mathbf{S}_{-q} \rangle_{j=0} = 1 - e^{iqa} + e^{2iqa} - e^{3iqa} + \cdots$$

In order to get as large a contribution as possible, the exponential factor must be positive for the terms with a plus sign and negative for the terms with a minus sign. We

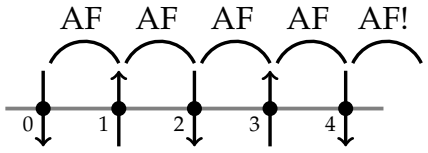

Figure B.16: An even-particle chain with nearest-neighbour antiferromagnetic interactions. With periodic boundary conditions, the coupling between the first and last spin causes a frustration, which would lead the spins to be somewhat rotated with respect to each other (in other words, not completely antiparallel). If we have open boundary conditions, the system is frustration-free.

Table B.19: The spin correlation for different q's for the five spin antiferromagnetic chain with open boundary conditions. $J_1 = 1$ and $\beta = 1000$.

qa	0	$2\pi/5$	$4\pi/5$
$\langle \mathbf{S}_q \mathbf{S}_{-q} \rangle$	0.0400	0.0611	0.419

easily see that $q = \frac{\pi}{a}$ maximizes our spin correlation function: Spins separated by a are antiparallel, and their negative dot product will be multiplied by a factor of $e^{i(2n-1)\pi} = -1$, while the spins separated by $2a$ will be multiplied by a factor of $e^{i2\pi n} = 1$. $\frac{\pi}{a}$ is thus the ordering wave vector of the system:

$$N^2 \langle \mathbf{S}_q \mathbf{S}_{-q} \rangle_{j=0} = 1 - e^{i\pi} + e^{2i\pi} - e^{3i\pi} + \cdots = N$$

The odd-particle chain

Figure (B.16) shows an odd-particle chain with antiferromagnetic interactions. If periodic boundary conditions are employed, the coupling between the first and last spin causes a frustration. In the case of open boundary conditions, there is no such bond, leaving the system frustration-free. In the latter instance, $q = \frac{\pi}{a}$ would maximize $\langle \mathbf{S}_q \mathbf{S}_{-q} \rangle$ just as for the even-particle case, but that value is not included in our discrete set

$$\mathbf{q} = \frac{2\pi k}{Na}\hat{i}; \qquad q = 0, \frac{2\pi}{Na}, \frac{4\pi k}{Na}, \cdots, \frac{2\pi(N-1)}{Na} \tag{B.23}$$

Obviously, as N is odd, it is impossible to retrieve $\frac{\pi}{a}$ for the antiferromagnetic system. Without that option, we will probably get quite a large contribution to the q's closest to $\frac{\pi}{a}$, namely $\frac{\pi}{a} \pm \frac{\pi}{Na}$. We would also expect small contributions from at least some of the other q-values. This is consistent with the results of table (B.19). In the case of the periodic boundary conditions, the system would not be as ordered as in figure (B.16), and we would expect more evenly distributed contributions to $\langle \mathbf{S}_q \mathbf{S}_{-q} \rangle$.

D The chain with a constant angle θ between spins

Assuming there is a fixed angle θ between each spin, the spin correlation function becomes:

$$N^2 \langle \mathbf{S}_q \mathbf{S}_{-q} \rangle = \sum_{k=0}^{N-1} \sum_{j=0}^{N-1} \cos\left((j-k)\theta\right) e^{iqa(j-k)} \tag{B.24}$$

$$= 1 + \cos\theta e^{iqa} + \cos 2\theta e^{i2qa} + \cos 3\theta e^{i3qa} + \cdots$$

We differentiate to minimize with respect to q:

$$\frac{\partial}{\partial q} \langle \mathbf{S}_q \mathbf{S}_{-q} \rangle = ia \sum_{k=0}^{N-1} \sum_{j=0}^{N-1} (j-k) \cos\left((j-k)\theta\right) e^{iqa(j-k)}$$

$$= -2a \sum_{x=1}^{N-1} (N-|x|) x \cos\left(x\theta\right) \sin\left(qax\right) = 0 \tag{B.25}$$

In trying to determine if our q corresponds to a minima or maxima, we must look at the sign of the double derivative with respect to q:

$$N^2 \frac{\partial^2}{\partial q^2} \langle \mathbf{S}_q \mathbf{S}_{-q} \rangle = -2a^2 \sum_{x=1}^{N-1} (N-|x|) x^2 \cos\left(x\theta\right) \cos(qax)$$

There seems to be no straightforward way to solve this in general, however. Instead, we study the function for different Ns.

The derivation of Eq. (B.25)

We want to tidy up the expression

$$\frac{\partial}{\partial q} \langle \mathbf{S}_q \mathbf{S}_{-q} \rangle = ia \sum_{k=0}^{N-1} \sum_{j=0}^{N-1} (j-k) \cos\left((j-k)\theta\right) e^{iqa(j-k)}$$

As k and j only enter through the combination $x = j-k$, we want to sum over x instead. From the ranges of j and k, we see that x can take $2N-1$ possible values, the integers from $-(N-1)$ to $N-1$. Since we have a limited number of available j and k-values, each value of x will appear with a specific weight. For a given x-value a:

$$x = j-k = a \qquad \rightarrow \qquad j = k+a$$

No matter the value of a, j and k must be integers in the range $[0, N-1]$. Assuming that $a > 0$

$$a \leq k+a = j \leq N-1 \qquad \rightarrow \qquad 0 \leq k \leq N-a-1$$

Since k takes integer values starting from 0, it might take on $N - a$ different values. In other words the $x = a$-term should be weighted by $N - a$ in the sum, as long as a is positive.

If $a < 0$, j and k switch roles

$$x = j - k = -|a| \quad \rightarrow \quad k = j + |a|$$

$$|a| \leq j + |a| = k \leq N - 1 \quad \rightarrow \quad 0 \leq j \leq N - |a| - 1$$

So any term $x = a$ appears with weight $N - |a|$ in the sum over x.

We are left with:

$$\frac{\partial}{\partial q} \langle \mathbf{S}_q \mathbf{S}_{-q} \rangle = ia \sum_{x=-N+1}^{N-1} (N - |x|) x \cos(x\theta) e^{iqax}$$

$$= ia \sum_{x=0}^{N-1} (N - |x|) x \cos(x\theta) \left(e^{iqax} - e^{-iqax} \right)$$

$$= -2a \sum_{x=1}^{N-1} (N - |x|) x \cos(x\theta) \sin(qax)$$

Since $(N - |x|)$ and $\cos(x\theta)$ only depends on the absolute value of x and $e^{ikx} - e^{-ikx} = 2i \sin(kx)$.

The 5-particle case

With five particles, q can take the values

$$q = 0, \frac{2\pi}{5a}, \frac{4\pi}{5a}, \frac{6\pi}{5a}, \frac{8\pi}{5a}$$

The spin correlation function is symmetric about $q = \frac{\pi}{a}$, so we only consider the first few values.

We want to limit ourselves to study the chain with periodic boundary conditions. Then we have three angles that might minimize the energy and agree with the length of the chain: $\theta = 0$, $\theta = 2\pi/5$, $\theta = 4\pi/5$.

Table (B.20) shows the expected value of the ordering wave vector versus the program output for different couplings J_1 and J_2 which cause θ to match the length of the chain. We see that there is an agreement for all the listed couplings. When there are two maxima, the value of $\langle \mathbf{S}_q \mathbf{S}_{-q} \rangle$ at each is about half the value of $\langle \mathbf{S}_0 \mathbf{S}_{-0} \rangle$. This is just what we expect, since the spin correlation function is normalized.

Note that for all our efforts, $qa = \theta$ consistently yields the largest value of $\langle \mathbf{S}_q \mathbf{S}_{-q} \rangle$. This should in no way come as a surprise: In order to maximize the spin correlation function, the ordering wave vector should match for the rotation of the spins, so that every spin contributes with $+1$ $N \langle \mathbf{S}_q \mathbf{S}_{-q} \rangle$. That is why the ordering wave vector were

Table B.20: The expected values of the ordering wave vector q with $N = 5$, together with the q's that yield the largest spin correlation function in the simulations. We have set $a = 1$. θ is the angle between neighbouring spins, which we used in our analysis. We have included the largest value of the spin correlation from our simulations.

J_1	J_2	Corresponding θ	Expected q	q, simulations	$\langle \mathbf{S}_q \mathbf{S}_{-q} \rangle$
-1	$1/4$	0	0	0	0.99804
-1	$1/(\sqrt{5}-1)$	$2\pi/5$	$2\pi/5, 8\pi/5$	$2\pi/5, 8\pi/5$	0.49976
1	$1/(1+\sqrt{5})$	$4\pi/5$	$4\pi/5, 6\pi/5$	$4\pi/5, 6\pi/5$	0.49964

Table B.21: The expected values of the ordering wave vector q with $N = 6$, together with the q's that yield the largest spin correlation function in the simulations. We have set $a = 1$. θ is the angle between neighbouring spins, which we used in our analysis. We have included the largest value of the spin correlation from our simulations.

J_1	J_2	Corresponding θ	Expected q	Largest q's	$\langle \mathbf{S_q} \mathbf{S_{-q}} \rangle$
-1	$1/4$	0	0	0	0.99696
-1	$1/2$	$\pi/3$	$\pi/3, 5\pi/3$	$\pi/3, 5\pi/3$	0.49951
1	$1/2$	$2\pi/3$	$2\pi/3, 4\pi/3$	$2\pi/3, 4\pi/3$	0.49953
1	$1/4$	π	π	π	0.99689

found to be $q = 0$ for the ferromagnetic system and $q = -\pi/a$ for the antiferromagnetic system, where the antiparallel neighbours had an angle of $\theta = \pi$ between them. With these ordering wave vectors, the dot product and the exponential had the same sign for each term, maximizing the spin correlation function.

The 6-particle case

With six particles, q can take the values

$$q = 0, \frac{\pi}{3a}, \frac{2\pi}{3a}, \frac{\pi}{a}, \frac{4\pi}{3a}, \frac{5\pi}{3a}$$

The spin correlation function is symmetric about $q = \frac{\pi}{a}$, so we only consider the first four values.

We want to limit ourselves to study the chain with periodic boundary conditions. Then we have four angles that might minimize the energy and agree with the length of the chain: $\theta = 0, \frac{\pi}{3}, \frac{2\pi}{3}, \pi$.

Table (B.21) shows the expected value of the ordering wave vector vs the program output for different couplings J_1 and J_2 which cause θ to match the length of the chain. We see that there is an agreement between expectation and output for all couplings. There is also an agreement between the angle of rotation between neighbours and the ordering wave vector, as expected.

Appendix C

The spiralization condition for a chain

C.1 The Dzyaloshinskii-Moriya term

Applying eq. (4.1) to Eq. (2.23), Where $\mathbf{u}$, $\mathbf{v}$ are normalized, orthogonal vectors in the plane of rotation. The cross product between two adjacent spins are:

$$\begin{aligned}\mathbf{S}\left(\mathbf{r}_i\right)\times\mathbf{S}\left(\mathbf{r}_{i+1}\right) &= \left[\mathbf{u}\cos\left(\mathbf{Q}\cdot\mathbf{r}_i\right)+\mathbf{v}\sin\left(\mathbf{Q}\cdot\mathbf{r}_i\right)\right]\times\left[\mathbf{u}\cos\left(\mathbf{Q}\cdot\mathbf{r}_{i+1}\right)+\mathbf{v}\sin\left(\mathbf{Q}\cdot\mathbf{r}_{i+1}\right)\right]\\ &= \mathbf{u}\times\mathbf{v}\cos\left(\mathbf{Q}\cdot\mathbf{r}_i\right)\sin\left(\mathbf{Q}\cdot\mathbf{r}_{i+1}\right)+\mathbf{v}\times\mathbf{u}\sin\left(\mathbf{Q}\cdot\mathbf{r}_i\right)\cos\left(\mathbf{Q}\cdot\mathbf{r}_{i+1}\right)\\ &= \mathbf{u}\times\mathbf{v}\left[\cos\left(\mathbf{Q}\cdot\mathbf{r}_i\right)\sin\left(\mathbf{Q}\cdot\mathbf{r}_{i+1}\right)-\sin\left(\mathbf{Q}\cdot\mathbf{r}_i\right)\cos\left(\mathbf{Q}\cdot\mathbf{r}_{i+1}\right)\right]\end{aligned}$$

We recognize the bracketed expression as the sine of a difference

$$\mathbf{S}\left(\mathbf{r}_i\right)\times\mathbf{S}\left(\mathbf{r}_i\right)=\mathbf{u}\times\mathbf{v}\sin\left(\mathbf{Q}\cdot\mathbf{r}_{i+1}-\mathbf{Q}\cdot\mathbf{r}_i\right)=\mathbf{u}\times\mathbf{v}\sin\left[\mathbf{Q}\cdot\left(\mathbf{r}_{i+1}-\cdot\mathbf{r}_i\right)\right]=\mathbf{u}\times\mathbf{v}\sin\left(\mathbf{Q}\cdot\Delta\mathbf{r}\right)$$

Where $\Delta\mathbf{r}$ depends on the direction of the bond. In a chain, a quadratic or a simple cubic lattice, it is on a simple form:

$$\Delta\mathbf{r}=a\hat{x}\ \ \vee\ \ a\hat{y}\ \ \vee\ \ a\hat{z}$$

where all possibilities are available for the cubic lattice, but only the first two for the quadratic lattice and only the first for the chain. a is the grid length. Considering only the chain at the moment, our expression simplifies to:

$$\mathbf{S}_i\times\mathbf{S}_{i+1}=\mathbf{S}\left(\mathbf{r}_i\right)\times\mathbf{S}\left(\mathbf{r}_{i+1}\right)=\mathbf{u}\times\mathbf{v}\sin\left(Q_x a\right) \tag{C.1}$$

where Q_x is the x-component of $\mathbf{Q}$ (and the only relevant component in the 1D case). The Hamiltonian simplifies to

$$H_{DM}=-\mathbf{D}\cdot\sum_{i=0}^{\tilde{N}}\mathbf{u}\times\mathbf{v}\sin\left(Q_x a\right)$$

We rename $\mathbf{D} \cdot (\mathbf{u} \times \mathbf{v}) = D \cos \alpha$, where $D = |\mathbf{D}| > 0$ (taking the dot product of $\mathbf{D}$ with the normalized vector $(\mathbf{u} \times \mathbf{v})$).

$$E = H_{DM} = -\tilde{N} D \sin(Q_x a) \cos \alpha \tag{C.2}$$

With the number of bonds $\tilde{N}$ being N for periodic boundary conditions and $N-1$ for open boundary conditions. We minimize E with respect to Q_x and set it equal to zero:

$$\frac{\partial E}{\partial Q_x} = -a\tilde{N} D \cos(Q_x a) \cos \alpha = 0$$

Assuming that $\cos \alpha \neq 0$, this leaves us with $\cos(Q_x a) = 0$, meaning $Q_x a = \frac{\pi}{2}(2n-1)$. We consider the sign of the second derivative:

$$\frac{\partial^2 E}{\partial Q_x^2} = a^2 \tilde{N} \sin(Q_x a)\, \mathbf{D} \cdot (\mathbf{u} \times \mathbf{v})$$

If $\cos \alpha > 0$:

$$\frac{\partial^2 E}{\partial Q_x^2} = a^2 \tilde{N} \sin(Q_x a)\,; \quad \frac{\partial E}{\partial Q_x} \text{ is } \begin{cases} > 0 \text{ for } Q_x a = \frac{\pi}{2}\text{: Minima} \\ < 0 \text{ for } Q_x a = \frac{3\pi}{2}\text{: Maxima} \end{cases}$$

If $\cos \alpha < 0$:

$$\frac{\partial^2 E}{\partial Q_x^2} = -a^2 \tilde{N} \sin(Q_x a)\,; \quad \frac{\partial E}{\partial Q_x} \text{ is } \begin{cases} < 0 \text{ for } Q_x a = \frac{\pi}{2}\text{: Maxima} \\ > 0 \text{ for } Q_x a = \frac{3\pi}{2}\text{: Minima} \end{cases}$$

So the minima and maxima depends on the sign of $\cos \alpha$. In any case, $Q_x = \frac{\pi}{2a}$ and $Q_x = \frac{3\pi}{2a}$ are our extremal points. Note that there is not much difference between these points: They are both a rotation of $\frac{\pi}{2}$, but in different directions. Additionally, one only appears as a minima when $\cos \alpha = \mathbf{D} \cdot (\mathbf{u} \times \mathbf{v}) > 0$, and the other one when $\cos \alpha < 0$: the direction of the rotation by $\frac{\pi}{2}$ is not even arbitrary, but depends on how the spins are oriented with respect to each other. We attempt to find the optimal value of α:

$$\frac{\partial E}{\partial \alpha} = \tilde{N} D \sin(Q_x a) \sin \alpha = 0$$

so we have either $\sin(Q_x a) = 0$ or $\sin \alpha = 0$. The former yields $E = 0$ and is therefore uninteresting. The latter yields $\alpha = \pi n$, so $\cos \alpha = (-1)^n$. We inspect the extremal points for $n = 0$ and $n = 1$:

$$\frac{\partial^2 E}{\partial \alpha^2} = \tilde{N} D \sin(Q_x a) \cos \alpha \quad \rightarrow \quad \left.\frac{\partial^2 E}{\partial \alpha}\right|_{\alpha = \pi n} = \tilde{N} D \sin(Q_x a)\,(-1)^n$$

So if $\sin(Q_x a) > 0$:

$$\left.\frac{\partial^2 E}{\partial \alpha^2}\right|_{\alpha = \pi n} = \begin{cases} > 0 & \text{for } n = 0: \quad \text{minima} \\ < 0 & \text{for } n = 1: \quad \text{maxima} \end{cases}$$

Table C.1: Different couplings for the 12-particle open Dzyaloshinskii-Moriya chain at $\beta = 10$. The simulations were run with 100 000 equilibration sweeps, 10 000 lattice sweeps per bin and 100 bins.

D^x_{DM}	D^y_{DM}	D^z_{DM}	$\bar{S_x}$	$\bar{S_y}$	$\bar{S_z}$	$\bar{\theta}$	Expected θ
2	0	0	0.0977	0.5780	0.6847	1.5779	1.5708
1	0	0	0.1356	0.5751	0.6617	1.5035	1.5708
0	1	0	0.6062	0.2054	0.6385	1.5522	1.5708
0	0	1	0.5821	0.6233	0.2418	1.5274	1.5708

and for $\sin(Q_x a) < 0$:

$$\left.\frac{\partial^2 E}{\partial \alpha^2}\right|_{\alpha=\pi n} = \begin{cases} < 0 & \text{for } n = 0: \quad \text{maxima} \\ > 0 & \text{for } n = 1: \quad \text{minima} \end{cases}$$

So in the ground state configuration, $\mathbf{D} \cdot (\mathbf{u} \times \mathbf{v}) = D \cos\alpha$, $\alpha = \pi n$. Thus $\mathbf{D}$ is perpendicular to the plane spanned out by $\mathbf{u}$ and $\mathbf{v}$, meaning that $\mathbf{D}$ is parallel to the normal vector of said plane. Consequently, $\mathbf{D}$ determines the preferred plane of the spins in the ground state. Inspecting low temperatures, we expect a configuration where all the spins are very close to residing in the plane.

These predictions were tested against the 12-particle open chain for $\beta = 10$, as shown in table (C.1). The average spin component in the direction of $\mathbf{D}$ were significantly smaller than in the other directions, which is part of what we concluded from our analysis. The other prediction, that the angle between the spins would be $\pi/2$, fits well with the results.

C.2 Dzyaloshinskii-Moriya with nearest neighbour Heisenberg terms

We have the Hamiltonian

$$H = J \sum_i \mathbf{S}_i \cdot \mathbf{S}_{i+1} - \mathbf{D} \cdot \sum_i (\mathbf{S}_i \times \mathbf{S}_{i+1}) \tag{C.3}$$

and apply the rotation parametrization, (4.1) to the spins $\mathbf{S}_i$. We already know the result of the last term, so we calculate the dot product:

$$\begin{aligned} \mathbf{S}_i \cdot \mathbf{S}_{i+1} = \mathbf{S}(\mathbf{r}_i) \cdot \mathbf{S}(\mathbf{r}_{i+1}) &= [\mathbf{u}\cos(\mathbf{Q}\cdot\mathbf{r}_i) + \mathbf{v}\sin(\mathbf{Q}\cdot\mathbf{r}_i)] \\ &\cdot [\mathbf{u}\cos(\mathbf{Q}\cdot\mathbf{r}_{i+1}) + \mathbf{v}\sin(\mathbf{Q}\cdot\mathbf{r}_{i+1})] \\ &= \cos(\mathbf{Q}\cdot\mathbf{r}_i)\cos(\mathbf{Q}\cdot\mathbf{r}_{i+1}) + \sin(\mathbf{Q}\cdot\mathbf{r}_i)\sin(\mathbf{Q}\cdot\mathbf{r}_{i+1}) \end{aligned}$$

Using

$$\cos(x \pm y) = \cos x \cos y \mp \sin x \sin y$$

with $x = \mathbf{Q} \cdot \mathbf{r}_{i+1}$ and $y = \mathbf{Q} \cdot \mathbf{r}_i$, we obtain:

$$\begin{aligned} \mathbf{S}_i \cdot \mathbf{S}_{i+1} &= \cos\left(\mathbf{Q} \cdot \mathbf{r}_{i+1} - \mathbf{Q} \cdot \mathbf{r}_i\right) = \cos\left(\mathbf{Q}\left(\mathbf{r}_{i+1} - \mathbf{r}_i\right)\right) \\ &= \cos\left(\mathbf{Q} \cdot \Delta\mathbf{r}_i\right) \end{aligned} \tag{C.4}$$

Considering a chain, the result is

$$\mathbf{S}_i \cdot \mathbf{S}_{i+1} = \cos\left(Q_x a\right)$$

Inserted into our Hamiltonian:

$$E = H = \tilde{N}\left[J \cos\left(Q_x a\right) - D \sin\left(Q_x a\right) \cos\alpha\right] \tag{C.5}$$

In order to obtain the most elegant expressions, we minimize E with respect to α before we find the extrema in terms of Q_x.

$$\frac{\partial E}{\partial \alpha} = \tilde{N} D \sin\left(Q_x a\right) \sin\alpha = 0$$

As $\sin\left(Q_x a\right) = 0$ yields $E = 0$, $\sin\alpha = 0$, i.e. $\alpha = \pi n$.

$$\frac{\partial^2 E}{\partial \alpha^2} = \tilde{N} D \sin\left(Q_x a\right) \cos\alpha$$

So

$$\left.\frac{\partial^2 E}{\partial \alpha^2}\right|_{\alpha=\pi n} = (-1)^n \tilde{N} D \sin\left(Q_x a\right)$$

If $\sin\left(Q_x a\right) > 0$:

$$\left.\frac{\partial^2 E}{\partial \alpha^2}\right|_{\alpha=\pi n} = \begin{cases} > 0 & \text{for } n = 0: \quad \text{minima} \\ < 0 & \text{for } n = 1: \quad \text{maxima} \end{cases}$$

and for $\sin\left(Q_x a\right) < 0$:

$$\left.\frac{\partial^2 E}{\partial \alpha^2}\right|_{\alpha=\pi n} = \begin{cases} < 0 & \text{for } n = 0: \quad \text{maxima} \\ > 0 & \text{for } n = 1: \quad \text{minima} \end{cases}$$

Minimizing with respect to Q_x, we take the derivative of (C.5):

$$\begin{aligned} \frac{\partial E}{\partial Q_x} = -\tilde{N} a \left[J \sin\left(Q_x a\right) + D \cos\left(Q_x a\right) \cos\alpha\right] = 0 \\ J \sin\left(Q_x a\right) + D \cos\left(Q_x a\right) \cos\alpha = 0 \\ J \sin\left(Q_x a\right) = -D \cos\left(Q_x a\right) \cos\alpha \end{aligned}$$

$$\tan\left(Q_x a\right) = -\frac{D\cos\alpha}{J}$$

$$Q_x = \frac{1}{a}\arctan\left(-\frac{D\cos\alpha}{J}\right) + \pi n$$

$$Q_x = \frac{1}{a}\arctan\left(\pm\frac{D}{J}\right) + \pi n$$

$$Q_x = \pm\frac{1}{a}\arctan\left(\frac{D}{J}\right) + \pi n$$

Where we have taken into account that the angles may not only reside in the primary branch of the inverse tangent. So the extremal points depend only on the relative sizes of the couplings, in addition to the grid length.

We take the second derivative to distinguish between minima and maxima:

$$\frac{\partial^2 E}{\partial Q_x^2} = -\tilde{N}a^2\left[J\cos\left(Qx_a\right) - D\cos\alpha\sin\left(Q_x a\right)\right]$$

We insert for our extremal point, keeping in mind that $\cos\alpha = \pm 1$ for the maximum and minimum energies:

$$\sin\left(Q_x a\right) = -\frac{D\cos\alpha}{J}\cos\left(Q_x a\right)$$

$$\begin{aligned}\frac{\partial^2 E}{\partial Q_x^2} &= -\tilde{N}a^2\left[J\cos\left(Qx_a\right) - D\cos\alpha\left(-\frac{D\cos\alpha}{J}\cos\left(Q_x a\right)\right)\right] \\ &= -\tilde{N}a^2\left[J + \frac{D^2\cos^2\alpha}{J}\right]\cos\left(Q_x a\right) \\ &= -\frac{\tilde{N}a^2}{J}\left[J^2 + D^2\right]\cos\left(Q_x a\right)\end{aligned}$$

Since $\tilde{N}a^2$ and the expression in the paranthesis is always positive, only the signs of J and $\cos\left(Q_x a\right)$ determines whether our point is a minima or a maxima. For simplicity, we study ferromagnetic Heisenberg couplings ($J < 0$) and antiferromagnetic Heisenberg couplings ($J > 0$) separately.

For the ferromagnetic coupling, $J < 0$:

$$\frac{\partial^2 E}{\partial Q_x^2} = |\chi|\cos\left(Q_x a\right)$$

where $\chi = -\frac{\tilde{N}a^2}{J}\left[J^2 + D^2\right]$ becomes positive since J is negative. Then:

$$\frac{\partial^2 E}{\partial Q_x^2} = \begin{cases} < 0 \text{ for } \cos\left(Q_x a\right) < 0 \rightarrow Q_x \in \left(-\frac{\pi}{2a}, \frac{\pi}{2a}\right) \text{ (gives a maxima)} \\ > 0 \text{ for } \cos\left(Q_x a\right) > 0 \rightarrow Q_x \in \left(\frac{\pi}{2a}, \frac{3\pi}{2a}\right) \text{ (gives a minima)} \end{cases}$$

Table C.2: Different couplings for the 20-particle open chain with nearest neighbour Heisenberg and Dzyaloshinskii-Moriya interactions at $\beta = 10$. $J_1 = 1$ for all the runs. The simulations were run with 100 000 equilibration sweeps, 10 000 lattice sweeps per bin and 100 bins.

D^x_{DM}	D^y_{DM}	D^z_{DM}	$\lvert\bar{S_x}\rvert$	$\lvert\bar{S_y}\rvert$	$\lvert\bar{S_z}\rvert$	$\bar{\theta}$	Expected θ
2	0	0	0.1194	0.6356	0.6364	1.9265	2.0344
2	0	0	0.1135	0.6286	0.6192	1.9585	2.0344
1	0	0	0.1268	0.6318	0.6229	2.1865	2.3562
1	0	0	0.1920	0.5882	0.6527	2.1645	2.3562
0.5	0	0	0.2121	0.6528	0.5757	2.4289	2.6795
0.5	0	0	0.3093	0.5629	0.6115	2.5783	2.6795
0	0	1	0.6922	0.5544	0.1495	2.3563	2.3562
0	0	1	0.6413	0.6217	0.1497	2.3195	2.3562

The situation is obviously reversed for an antiferromagnetic coupling, $J > 0$:

$$\frac{\partial^2 E}{\partial Q_x^2} = -|\chi| \cos\left(Q_x a\right)$$

$$\frac{\partial^2 E}{\partial Q_x^2} = \begin{cases} > 0 \text{ for } \cos\left(Q_x a\right) < 0 \rightarrow Q_x \in \left(-\frac{\pi}{2a}, \frac{\pi}{2a}\right) \text{ (gives a minima)} \\ < 0 \text{ for } \cos\left(Q_x a\right) > 0 \rightarrow Q_x \in \left(\frac{\pi}{2a}, \frac{3\pi}{2a}\right) \text{ (gives a maxima)} \end{cases}$$

Table (C.2) lists the average absolute value of the spin components and the average angle between the spins for several systems with a different values of D/J, together with the predicted angle from our analytical minimalization. The inverse tangent being multivalued, there were several options for the predicted θ for a given ratio D/J. The ambiguity of the sign arising from $\cos\alpha$ even led to multiple values of θ being possible in one range of arctan. Since $\cos\alpha$ only determines the direction of the rotation (clockwise or counter-clockwise), we chose the prediction of θ closest to the angle from the simulations. In all cases, that angle resided in the $n = 1$-branch of arctan.

The numerical and analytical θ differs with up to about 10%, but we study the system at quite a small value of β, so the discrepancy might be due to our distance from zero temperature. Due to experience, we are hesitant to delve into lower temperatures as metastable states then emerge. In our analysis, we have encountered metastable states with $\beta = 100$. $\beta = 10$ seems like a fair trade-off between accessing low-energy states and avoiding the metastable configurations. On a happier note, the last rows of the table shows a good agreement between the numerical and analytical angle.

C.3 Pure Heisenberg couplings

We already know that

$$H = J\sum_i \mathbf{S}_i \cdot \mathbf{S}_{i+1} = \tilde{N}J\cos\left(Q_x a\right)$$

So:

$$\frac{\partial E}{\partial Q_x} = -\tilde{N}J\sin\left(Q_x a\right) = 0 \quad \rightarrow \quad \sin\left(Q_x a\right) = 0 \quad \rightarrow \quad Q_x = \frac{\pi n}{a}$$

$$\left.\frac{\partial^2 E}{\partial Q_x^2}\right|_{\pi n/a} = \left.-\tilde{N}J\cos\left(Q_x a\right)\right|_{\pi n/a} = -\tilde{N}Ja^2\left(-1\right)^n$$

For $J < 0$: ferromagnetic coupling:

$$\frac{\partial^2 E}{\partial Q_x^2} = \left|\tilde{N}Ja^2\right|\left(-1\right)^n = \begin{cases} > 0 \text{ for} & Q_x = \frac{2\pi n}{a} & \rightarrow \text{ minima} \\ < 0 \text{ for} & Q_x = \frac{\pi}{a}\left(2n-1\right) & \rightarrow \text{ maxima} \end{cases}$$

For $J > 0$: antiferromagnetic coupling:

$$\frac{\partial^2 E}{\partial Q_x^2} = -\left|\tilde{N}Ja^2\right|\left(-1\right)^n = \begin{cases} < 0 \text{ for} & Q_x = \frac{2\pi n}{a} & \rightarrow \text{ maxima} \\ > 0 \text{ for} & Q_x = \frac{\pi}{a}\left(2n-1\right) & \rightarrow \text{ minima} \end{cases}$$

The results are consistent with what we already know: In the ferromagnetic case, the ground states will have parallel spins (an angle of 0 or 2π) between each, while the spins will be antiparallel in the antiferromagnetic case (an angle of π).

C.4 Nearest- and next-nearest neighbour Heisenberg couplings

Looking at nearest- and next-nearest neighbour Heisenberg couplings using the spiralization condition, we obtain

$$H = J_1\sum_i \mathbf{S}_i \cdot \mathbf{S}_{i+1} + J_2\sum_i \mathbf{S}_i \cdot \mathbf{S}_{i+2} \tag{C.6}$$

where J_1 is the nearest neighbour coupling and J_2 is the next-nearest neighbour coupling. If J_1 and J_2 are not both ferromagnetic couplings, there will be a competition between the two terms.

A The extremal points

The Hamiltonian (C.6) simplifies considerably when there is a fixed angle θ between each pair of neighbouring spins

$$E = N\left[J_1\cos\theta + J_2\cos\left(2\theta\right)\right] \tag{C.7}$$

We insert for the awkward factor of $\cos(2\theta)$ using standard trigonometric identities

$$E = N\left[J_1\cos\theta + J_2\left(2\cos^2\theta - 1\right)\right] \tag{C.8}$$

To find the extremal points of E, we must differentiate with respect to θ, using $4\cos\theta\sin\theta = 2\sin 2\theta$ for convenience

$$\begin{aligned}\frac{\partial E}{\partial\theta} &= N\left[-J_1\sin\theta - 4J_2\cos\theta\sin\theta\right] = 0\\ &\sin\theta\left(-J_1 - 4J_2\cos\theta\right) = 0\end{aligned}$$

So either

$$\sin\theta = 0 \quad \rightarrow \quad \theta = n\pi,\ \ n\in\mathbb{Z}$$

or

$$J_1 + 4J_2\cos\theta = 0 \ \rightarrow\ \cos\theta = -\frac{J_1}{4J_2} \ \rightarrow\ \theta = \pm\arccos(-\frac{J_1}{4J_2})(\mp\vee\pm)2n\pi \tag{C.9}$$

The latter solution only holds when

$$\left|\frac{J_1}{4J_2}\right| \leq 1 \quad \rightarrow \quad |J_2| \geq \frac{|J_1|}{4}$$

When the equality holds, the answer coincides with that of $\sin\theta = 0$. If $|J_2| \leq \frac{|J_1|}{4}$, the extremal points are determined by $\sin\theta = 0$, thus being situated at $\theta = n\pi$.

Classifying the extremal points

Now that we have found our extremal points, we want to classify them. We inspect the double derivative of the energy with respect to θ:

$$\begin{aligned}\frac{\partial^2 E}{\partial\theta^2} &= -N\frac{\partial}{\partial\theta}\left[J_1\sin\theta + 2J_2\sin 2\theta\right] = -N\left[J_1\cos\theta + 4J_2\cos 2\theta\right]\\ &= -N\left[J_1\cos\theta + 8J_2\cos^2\theta - 4J_2^2\right]\end{aligned} \tag{C.10}$$

Considering $\theta = \arccos\left(-\frac{J_1}{4J_2}\right)$

$$\frac{\partial^2 E}{\partial\theta^2} = -N\left[-\frac{J_1^2}{4J_2} + 8J_2\frac{J_1^2}{16J_2^2} - 4J_2\right] = -N\left[\frac{2J_1^2 - J_1^2}{4J_2} - 4J_2\right]$$

$$= -4J_2N\left[\left(\frac{J_1}{4J_2}\right)^2 - 1\right] = 4J_2N\left[1 - \left(\frac{J_1}{4J_2}\right)\right]$$

But since $\left|\frac{J_1}{4J_2}\right| = |\cos\theta| \leq 1$, $\left[1 - \left(\frac{J_1}{4J_2}\right)\right] \geq 0$. Then, the sign of $\frac{\partial^2 E}{\partial\theta^2}$ depends solely on the sign of J_2:

$$\begin{aligned} &\text{If } J_2 > 0, \frac{\partial^2 E}{\partial\theta^2} > 0 \quad \text{and we have a (local) minima} \\ &\text{If } J_2 < 0, \frac{\partial^2 E}{\partial\theta^2} < 0 \quad \text{and we have a (local) maxima} \end{aligned} \tag{C.11}$$

As long as we consider $J_2 > 0$ and $J_2 < J_1$, we have found a set of local minimas for the energy

$$E = -N\left[\frac{J_1^2}{8J_2} + J_2\right] \tag{C.12}$$

which we found by using eq.s (C.7) and (C.9).

However, we have another set of extremal points that may also be local minima. In order to determine if Eq. (C.12) is the actual ground state energy, we have to consider the other extremal points $\theta = \pi n$ as well. We only want to evaluate them in the reign where $\theta = \arccos\left(-\frac{J_1}{4J_2}\right)$ might be a minima, i.e. $J_2 > 0$, $|J_1| < 4|J_2|$. Inserting for $\theta = \pi n$ in Eq. (C.10) yields

$$\frac{\partial^2 E}{\partial\theta^2} = -N\left[J_1(-1)^n + 4J_2(2 - J_2)\right]$$

The aim of this thesis is to inspect physical models of $LiNiPO_4$, and in all our sources [13], [15], [25] $0 < J_2 < 1$. In that instance

$$4J_2\,(2 - J_2) > 4\,|J_2| > |J_1|$$

Clearly, $\theta = \pi n$ are local maximas of the energy. But then Eq. (C.12) is indeed the ground state of the system.

B Minimizing the energy with periodic boundary conditions

We have seen that the ground state will favour an angle $\theta = \arccos\left(-\frac{J_1}{4J_2}\right)$ between adjacent spins as a compromise between the nearest and next-nearest neighbour bonds. Considering a chain of N, the angles will add up such that the angle between the first spin $\mathbf{S}_0$ and the last, $\mathbf{S}_{N-1}$, will be $(N-1)\theta$. The endpoint bond will want to rotate $\mathbf{S}_N = \mathbf{S}_0$ by θ from $\mathbf{S}_{N-1}$. In other words, the bonds between the endpoint spins will want to rotate $\mathbf{S}_0$ with an angle $N\theta$ relative to itself. If $N\theta \neq 2\pi n$, the orientations of $\mathbf{S}_0$ are conflicting, and the system is said to be frustrated.

We might avoid this conflict altogether by studying systems with $\theta = \frac{2\pi n}{N}$. The angle θ is determined by our couplings, we must consider J_1 and J_2 such that

$$\arccos\left(\frac{-J_1}{4J_2}\right) = \frac{2\pi n}{N}$$

Table C.3: The expected angle of rotation between neighbouring spins for different 'simplifying' couplings J_1 and J_2 near the ground state for $N = 5$. The expected angle of rotation θ between each spin is given by (C.9). Adding or subtracting $2\pi n$ to that column would still yield the ground state. $\bar{\theta}$ is the average angle between neighbouring spins in the simulation. E stands for the energy and ΔE is the standard deviation in the energy. The simulations were for $\beta = 1000$ run with 10000 equilibration sweeps and 1000 bins with 10000 lattice sweeps in each.

J_1	J_2	Expected θ	$\bar{\theta}$, sim.	E, an.	E, sim.	ΔE
-1	$1/4$	0	0.073	-3.75	-3.74594	$3.5 \cdot 10^{-5}$
-1	$1-\sqrt{5}$	± 1.2566	1.2568	-4.81763	-4.81411	$3.0 \cdot 10^{-5}$
1	$1+\sqrt{5}$	± 2.5133	2.5102	-3.56763	-3.56412	$2.7 \cdot 10^{-5}$

$$\frac{J_1}{J_2} = -4\cos\left(\frac{2\pi n}{N}\right) \tag{C.13}$$

or

$$J_2 = -\frac{J_1}{4\cos\left(\frac{2\pi n}{N}\right)}$$

We could of course avoid the problem altogether by considering open boundary conditions. That would however modify θ somewhat. With open boundary conditions, we have $N-1$ nearest neighbour bonds and $N-2$ next-nearest neighbour bonds. The preferred angle is then

$$\theta = \arccos\left(-\frac{J_1(N-1)}{4J_2(N-2)}\right) \tag{C.14}$$

which approaches (C.9) when $N \to \infty$. We will focus on periodic boundary conditions for the time being, but will revisit Eq. (C.14) later on.

C Results with relevant couplings

With $N = 5$

Table (C.3) shows the expected angles θ between neighbouring spins along with the average $\bar{\theta}$ for the simulations. The analytical and numerical energies are quite similar for all couplings, although they do not agree within the standard deviation. One possible explanation for the discrepancy could be that our temperature is not sufficiently low for the system to have reached the ground state. Additionally, the Metropolis algorithm is not ideal for finding the ground state energy as very few moves will be accepted at low temperatures. We could also be stuck in a metastable state close to the ground state. Whatever the exact reason, the values are close enough to the ground state energies to not discredit our code.

Table C.4: The expected angle of rotation between neighbouring spins for different 'simplifying' couplings J_1 and J_2 near the ground state for $N = 6$. The expected angle of rotation θ between each spin is given by (C.9). Adding or subtracting $2\pi n$ to that column would still yield the ground state. $\bar{\theta}$ is the average angle between neighbouring spins in the simulation. E stands for the energy and ΔE is the standard deviation in the energy. The expected energy was calculated by (C.12). The simulations were for $\beta = 1000$ run with 10000 equilibration sweeps and 1000 bins with 10000 lattice sweeps in each.

J_1	J_2	Expected θ	$\bar{\theta}$, sim.	E, an.	E, sim	ΔE
-1	$1/4$	0	0.0644	-4.5	-4.4950	$4.1 \cdot 10^{-5}$
-1	$1/2$	± 1.0472	1.0476	-4.5	-4.4954	$3.3 \cdot 10^{-5}$
1	$1/2$	± 2.0944	2.0940	-4.5	-4.5000	$3.3 \cdot 10^{-5}$
1	$1/4$	± 3.14159	3.0936	-4.5	-4.4950	$5.3 \cdot 10^{-5}$

With $N = 6$

Table (C.4) shows the expected angles θ between neighbouring spins along with the average $\bar{\theta}$ for the simulations. There is quite a large discrepancy between theory and simulations for θ in the last row, but the two results are not vastly different. Overall, the energies do however agree quite well with the theoretical result, though not within the standard deviation. Possible reasons for the discrepancies is discussed for the five spin case.

C.5 Heisenberg and Dzyaloshinskii-Moriya terms

We have yet to examine the Hamiltonian with both Dzyaloshinskii-Moriya terms and nearest- and next-nearest neighbour Heisenberg terms. Applying the spiralization condition to the chain, we obtain

$$E = N_{nn} J_1 \cos(Q_x a) + N_{nnn} J_2 \cos(Q_x a) - \alpha \sin(Q_x a) \tag{C.15}$$

Table C.5: The angles that minimize Eq. (C.15) by using the couplings in table (3.4). The nearest neighbour couplings are set to $J_{nn} = 2(J_{xy} + J_{yz})$ and $\alpha = 2D^y_{DM}$ to mimick the fcc lattice. N is the number of particles in the chain and $Q_{min}a$ is the angle that minimizes the energy. $Q_{min}a$ for $N = \infty$ was found using periodic boundary conditions. The uncertainty stems from the limited resolution. The last line shows the average angle $\bar{\theta}$ from simulations at 2.5 K.

	N	6	20	100	∞
Theory	$Q_{min}a$	2.522 ± 0.003	2.424 ± 0.003	2.397 ± 0.003	$2.389118 \pm 5 \cdot 10^{-6}$
Experiments	$\bar{\theta}$	2.177	2.150	2.1879	$--$

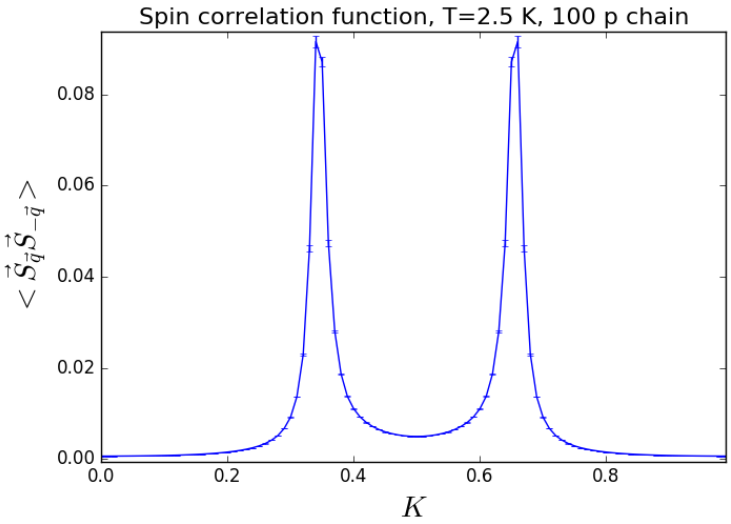

Figure C.1: The spin correlation function for the 100 spin chain with $J_1 = 2.64$, $J_2 = 0.67$ and $D^y_{DM} = 0.64$ and open boundary conditions. We see two incommensurate peaks.

where $\alpha = 2D^y_{DM}$. We minimize Eq. (C.15) numerically using Toft-Petersen's couplings J_{xy}, J_{yz} and D_{14} (see table (3.4)), with the nearest neighbour couplings multiplied by two to compensate for the increased number of neighbours in the face-centered cubic lattice, which we want to mimick. We obtain the results of table (C.5), which shows incommensurate angles. The simulations were run at 2.5 K with 100 bins and 10^5 equilibration sweeps and lattice sweeps per bin. The agreement is not perfect, but T=2.5 K is high enough that the state of the system would deviate a bit from the ground state.

The spin correlation function is plotted in figure (C.1), and shows two incommensurate peaks.

C.6 The effect of single-ion anisotropy

The single-ion anisotropy differs from the other terms of our Hamiltonian as it is an on-site effect, and consequently does not couple spins. That is the reason behind excluding it from Chapter 5. We will start this section by minimizing a one-spin Hamiltonian to get an intuition of the effect, and then move on to inspect how it affects the frustrated system by use of the spiralization condition. As we shall see, the condition must be applied with some caution when describing a system with single-ion anisotropy.

A General

First, we consider a Hamiltonian of only single-ion anisotropy terms. No bonds being present, the spins will be randomly oriented with respect to each other, while minimiz-

ing the energy at $T = 0$.

But how do you obtain the minimal energy for a pure single-ion anisotropy Hamiltonian? The Hamiltonian itself is simple enough

$$H = \sum_i \left[D^x_{\text{an}} \left(S^x_i\right)^2 + D^y_{\text{an}} \left(S^y_i\right)^2 + D^z_{\text{an}} \left(S^z_i\right)^2 \right] \tag{C.16}$$

As seen from Eq. (C.16), the sign of the spin components does not affect the energy. However, the sign of D^α_{an} is crucial in determining the configuration. Now, since there are no bonds, all spins are independent and equal, so we restrict ourselves to looking at one spin only.

$$E = D^x_{\text{an}} \left(S^x\right)^2 + D^y_{\text{an}} \left(S^y\right)^2 + D^z_{\text{an}} \left(S^z\right)^2$$

We check what happens if only one of the coefficients D^α_{an} is non-zero

$$E = D^\alpha_{\text{an}} \left(S^\alpha\right)^2$$

We minimize with respect to S^α:

$$\frac{\partial E}{\partial S^\alpha} = 2D^\alpha_{\text{an}} \left|S^\alpha\right| = 0; \qquad \rightarrow \qquad S^\alpha = 0 \tag{C.17}$$

$$\frac{\partial^2 E}{\partial^2 S^\alpha} = 2D^\alpha_{\text{an}}$$

If $D^\alpha_{\text{an}} > 0$, $\frac{\partial^2 E}{\partial^2 S^\alpha} > 0$, and $S^\alpha = 0$ is a minima of the energy. The ground state is then highly degenerate, including all spins of the form $\mathbf{S} = S^\beta \hat{\beta} + S^\gamma \hat{\gamma}$, where $\alpha \neq \beta \neq \gamma$.

If $D^\alpha_{\text{an}} < 0$, $\frac{\partial^2 E}{\partial^2 S^\alpha} < 0$, and $S^\alpha = 0$ is a maxima of the energy. This leaves us with no information of the ground state, until we remember that the spins are normalized. Due to the minus sign, the smallest possible value of E is

$$E = -\left|D^\alpha_{\text{an}}\right| \left(\left|S^\alpha\right|\right)^2 = -\left|D^\alpha_{\text{an}}\right|$$

i.e. the spin pointing purely in the $\hat{\alpha}$-direction.

There are no cross-terms with the components of $\mathbf{D}_{\text{an}}$ in the Hamiltonian, so we will retrieve Eq. (C.17) for every index. The interpretation will be the same for every direction: If D^α_{an} is negative, that direction is preferred, and if it is positive, the spins will disfavour it at low temperatures. However, we inspect the Hamiltonian with two non-zero components of $\mathbf{D}_{\text{an}}$ to see if we can obtain further insights

$$E = D^\alpha_{\text{an}} \left(S^\alpha\right)^2 + D^\beta_{\text{an}} \left(S^\beta\right)^2$$

The equations $\frac{\partial E}{\partial S^\alpha} = 0$ and $\frac{\partial E}{\partial S^\beta} = 0$ are equivalent, and we obtain $S^\alpha = 0$ and $S^\beta = 0$ as the extremal point. For $D^\alpha_{\text{an}} > 0$, $D^\beta_{\text{an}} > 0$, the ground state is doubly degenerate, i.e. $\mathbf{S} = \pm\hat{\gamma}$.

If $D_{\text{an}}^{\alpha} > 0$ and $D_{\text{an}}^{\beta} < 0$, the ground state is $\mathbf{S} = \pm\hat{\alpha}$, and similarly for β.

If $D_{\text{an}}^{\alpha} < 0$ and $D_{\text{an}}^{\beta} < 0$, the ground state spin will orient itself in the direction of the component of $\mathbf{D}_{\text{an}}$ largest in absolute value. If they are the same, the spin will orient itself in any of the directions in the $\alpha\beta$-plane, as seen from

$$E = -D\left(S^{\alpha}\right)^2 - D\left(S^{\beta}\right)^2 = -D\left[\left(S^{\alpha}\right)^2 + \left(S^{\beta}\right)^2\right]$$

which takes it largest negative value if the normalized spin $\mathbf{S}$ has no γ-component.

If all components of $\mathbf{D}_{\text{an}}$ are non-zero, the spin will avoid pointing in the directions of positive D_{an}^{α}, and orient itself along directions of negative D_{an}^{α}. Note that if $\mathbf{D}_{\text{an}}$ are either all positive or all negative, they will only shift the energy of the system and not affect the configuration of the spins.

The single-ion anisotropy does not conflict with ferro- or antiferromagnetic ordering. Even $D_{\text{an}}^{\alpha}, D_{\text{an}}^{\beta} > 0$ allows parallel or antiparallel ordering, albeit only in the $\hat{\gamma}$-direction. In other words, what the anisotropy does in this case is lowering the ground state degeneracy. Consequently, it will limit the feasibly available configurations at low temperature.

In summary:

For low temperatures:

1. If a single-ion anisotropy strength $D_{\text{an}}^{\alpha} < 0$, the spin will favour that direction.
2. If a single-ion anisotropy strength $D_{\text{an}}^{\alpha} > 0$, the spin will disfavour that direction.

When all $D_{\text{an}}^{\alpha} > 0$:

1. If only $D_{\text{an}}^{\alpha} > 0$, the spins will favour the $\beta\gamma$-plane.
2. If $D_{\text{an}}^{\alpha}, D_{\text{an}}^{\beta} > 0$, the spins will favour the $\pm\hat{\gamma}$-direction.
3. If all D_{an}^{α}>0, the energy will be shifted.

B Single-ion anisotropy and competing Heisenberg terms

We study a chain with competing nearest and next-nearest interactions with single-ion anisotropy terms. Applying the condition of spiralization yields

$$\begin{aligned} H = {} & N_1 J_1 \cos(Qa) + N_2 J_1 \cos(Qa) \\ & + \left(\frac{N+1}{2} + \frac{\cos\left(NQa\right)\sin\left(\left(N-1\right)Qa\right)}{2\sin\left(Qa\right)}\right)\left(D^x u_x^2 + D^y u_y^2 + D^z u_z^2\right) \\ & + \left(\frac{N-1}{2} - \frac{\cos\left(NQa\right)\sin\left(\left(N-1\right)Qa\right)}{2\sin\left(Qa\right)}\right)\left(D^x v_x^2 + D^y v_y^2 + D^z v_z^2\right) \end{aligned}$$

$$+\frac{\sin\left(\left(N-1\right)Qa\right)+\sin\left(NQa\right)}{\sin\left(Qa\right)}\left(D^{x}u_{x}v_{x}+D^{y}u_{y}v_{y}+D^{z}u_{z}v_{z}\right)$$

Where N_1 is the number of nearest-neighbour bonds and N_2 is the number of next-nearest neighbour bonds, both of which depend on our boundary conditions. Since the expression is quite complicated, we will want to simplify it. Minimizing with respect to all the components of **u** and **v** is, for instance, a daunting task. We have already seen/the sources state that the interesting physics happens in the y-direction of the crystal, which is why we should be able to capture much of the information by inspecting the chain. All three of the sources states a large y-component of the single-ion anisotropy, so the configuration will disfavour spin components in that direction. Consequently, the spins will practically reside in the xz-plane. We approximate and set $u_y = v_y = 0$. Now, **u** and **v** must be orthonormal, so we choose $\mathbf{u} = \hat{z}$ and $\mathbf{v} = \hat{x}$. Furthermore, $D^z = 0$ in all the papers. We are left with

$$\begin{aligned} H &= N_1 J_1 \cos(Qa) + N_2 J_1 \cos(Qa) \\ &+ \left(\frac{N-1}{2} - \frac{\cos\left(NQa\right)\sin\left(\left(N-1\right)Qa\right)}{2\sin\left(Qa\right)}\right) D^{x} \end{aligned} \tag{C.18}$$

which we will treat numerically.

At first sight, the last term looks a bit troublesome due to the sine in the denominator. We inspect the limit $Qa \to \pi n$ using L'Hôpital's rule:

$$\begin{aligned} \lim_{Qa\to\pi}\frac{\cos\left(NQa\right)\sin\left(\left(N-1\right)Qa\right)}{2\sin\left(Qa\right)} &= \lim_{Qa\to\pi}\frac{-N\sin\left(NQa\right)\sin\left(\left(N-1\right)Qa\right)}{2\cos\left(Qa\right)} \\ &+ \lim_{Qa\to\pi}\frac{\left(N-1\right)\cos\left(NQa\right)\cos\left(\left(N-1\right)Qa\right)}{2\cos\left(Qa\right)} \\ &= \frac{\left(N-1\right)(-1)^{n(N-1)(-1)^{nN}}}{2(-1)^{n}} = \frac{N-1}{2} \end{aligned}$$

So the entire single-ion anisotropy contribution will vanish in these limits

$$\lim_{Qa\to\pi}\left(\frac{N-1}{2} - \frac{\cos\left(NQa\right)\sin\left(\left(N-1\right)Qa\right)}{2\sin\left(Qa\right)}\right) = \frac{N-1}{2} - \frac{N-1}{2} = 0$$

Our single-ion anisotropy picks out the spin components in the x-direction. Since we have chosen to parametrize the spiralization as

$$\mathbf{S} = \cos(Qa)\hat{z} + \sin(Qa)\hat{x}$$

the spins will be oriented along the z-axis for $Qa = \pi n$. Hence, we neither expect nor get a contribution from the single-ion anisotropy in this case.

The spiralization condition allows us to absorb the single-ion anisotropy into a few terms, which is useful for a lot of cases. However, we mentioned that **u** and **v** have to

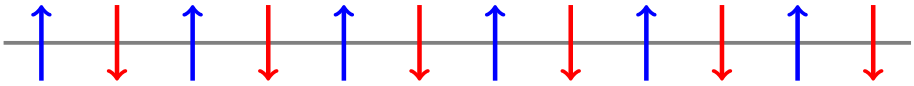

Figure C.2: Antiferromagnetic ordering of the one-dimensional spins.

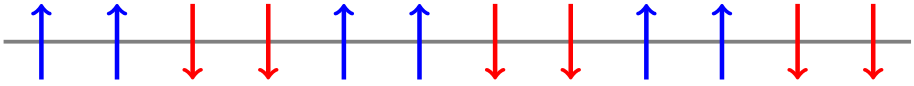

Figure C.3: Two by two ordering of the one-dimensional spins.

be orthogonal. If they are not, the whole condition falls apart. In the cases where we have a strong single-ion anisotropy in two directions, the spins will be effectively be one-dimensional. Then **u** and **v** cannot be orthogonal. In fact, they have to be parallel and consequently fails to properly describe spiralization. The only one-dimensional ordering we can get from the spiralization condition is parallel and antiparallel alignment, which appear when $Qa = \pi n$. There are other options for ordering 1D spins, like two spins pointing up, three pointing down and so on, but those cannot be described by our condition. Therefore, we must be cautious when applying the condition to systems with a large single-ion anisotropy in two directions. Arguably, those are the systems we are interested in.

Possible configurations of the one-dimensional spins

The simplest configuration of one-dimensional, normalized spins is a parallel or antiparallel alignment. Since we have competing interactions, however, we cannot immediately rule out other possibilities, like the spins being ordered in clusters of size two, size three and so on. The clusters of spins pointing up might not even be the same size as the clusters of spins pointing down.

We work with positive couplings, so we can rule out the ferromagnetic configuration as a candidate for the ground state. In deducing the energy for the more complicated configurations, we are going to ignore the contributions from the edges, as those are an effect of the choice of N, and does not scale with the system size anyway.

The antiferromagnetic system is however simple to analyse, as apparent from figure (C.2). All nearest neighbours are antiparallel, and all next-nearest neighbours are parallel. The total energy for the antiferromagnetic system is then

$$E = -(N-1)J_1 + (N-2)J_2$$

Figure (C.3) shows a chain with spins grouped in twos. Every other nearest neighbour bond is positive, and every other negative. Thus, the contribution from the nearest neighbour interaction disappears. All the next-nearest neighbour bonds are negative, so we are left with

$$E = -(N-2)J_2$$

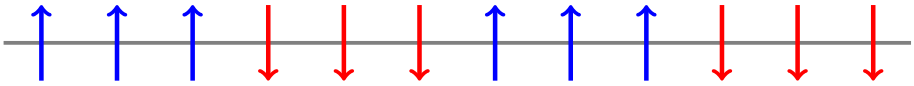

Figure C.4: Three by three ordering of the one-dimensional spins.

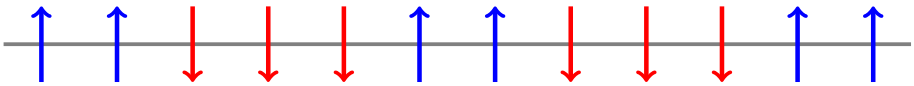

Figure C.5: Two by three ordering of the one-dimensional spins.

Figure (C.4) shows a chain with spins grouped in threes. One third of the nearest neigbour bonds are negative, and one third of the next-nearest bonds are positive. We are left with

$$E = \frac{N-1}{3}J_1 - \frac{N-2}{3}J_2$$

We can also have a mix of different domain sizes , for instance two spins down followed by two spins up and so on. An example is illustrated in figure (C.5). Boundary effects clearly kicks in for this kind of configuration, but roughly speaking, the energy goes as

$$E = \frac{N}{5}(J_1 - 3J_2)$$

for large N.

We might do this for as many configurations we like, but we appear to see a trend: For positive couplings J_1, J_2, large domains seems to be disfavoured. A set of configurations is listed in table (C.6), together with their energy in the limit of large N. Comparing, we see that the antiferromagnetic ordering has the lowest energy of these configurations as long as $2J_2 < J_1$.

Table C.6: The energy for different configurations of one-dimensional spins, when both nearest neighbour couplings J_1 and next-nearest neighbour couplings J_2 are present. *a-b* denotes *a* spin(s) pointing in one direction followed by *b* spin(s) in the other and so on.

Ordering	E/N	Ordering	E/N
AF	$J_2 - J_1$	1-3	0
2-2	$-J_2$	1-4	$1/5(J_1 + J_2)$
3-3	$1/3(J_1 - J_2)$	2-3	$1/5(J_1 - 3J_2)$
4-4	$1/2J_1$	2-4	$1/3(J_1 - J_2)$
1-2	$-1/3(J_1 + J_2)$	3-4	$1/7(3J_1 - J_2)$

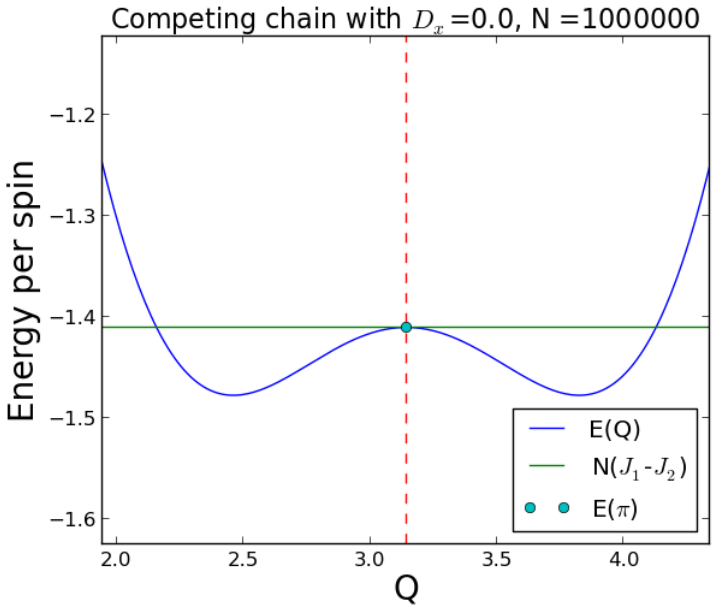

Figure C.6: The energy E versus the angle Q from Eq. (C.18) for $D^x = 0$, i.e. the competing chain without single-ion anisotropy in the x-direction. We have set $a = 1$. The dashed line gives the location of $Q = \pi$, and the dot is at $E(\pi)$. There are two minima of the function. $N = 1000000$.

The energy for $J_1 = 2.08$ and $J_2 = 0.67$

For our present choice of coupling strengths, the antiparallel ordering is the ground state when the spins become one-dimensional. As discussed, the spins lose a dimension when the single-ion anisotropy in that direction becomes too large.

Figures (C.6) to (C.8) shows how the energy E of (C.18) varies with the angle of rotation Q for different values of the single-ion anisotropy D^x. Increasing D^x increases the overall energy, except at $Q = \pi$ where the single-ion anisotropy does not contribute to the energy. For a large enough D^x, the antiferromagnetic ordering at $Q = \pi$ becomes the minima of E. This is seen in figure (C.8).

Figure (C.9) shows that from about $D^x = 0.13$ onwards, the energy will be minimized for an angle of rotation $Q = Q_{min} = \pi$. The exact value of D^x is given with greater accuracy in table (C.7). For now, we concern ourselves with the larger details. The abrupt change in the graph occurs when the single-ion anisotropy is large enough for the spins to favour the antiparallel ordering. The spins have now become one-dimensional and point in the positive or negative z-direction. There will consequently be no contribution from the single-ion anisotropy. That is why the minimal energy does not change as we increase D^x above $D^x \approx 0.13$.

We could wonder why the angle Q_{min} does not change with increasing D^x before the abrupt change at $D^x \approx 0.13$. There could perhaps be some angle Q that offers a compromise between the rotation brought on by J_1 and J_2 and the single-ion anisotropy's

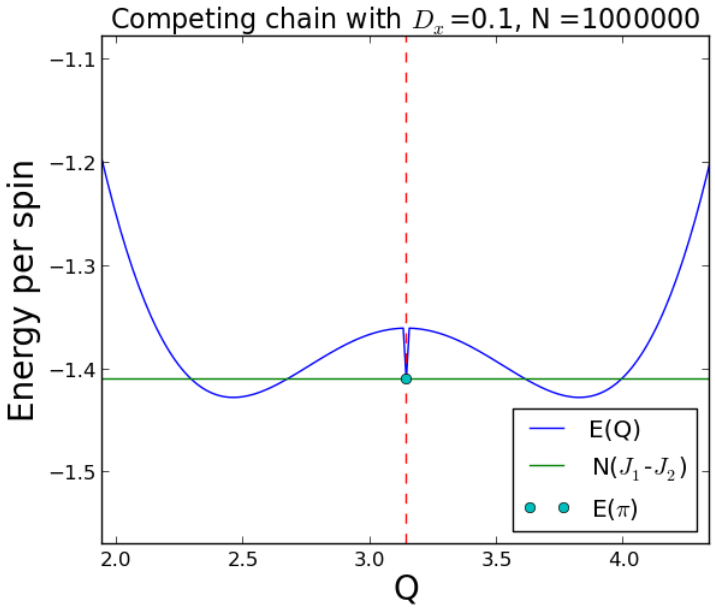

Figure C.7: The energy E versus the angle Q from Eq. (C.18) with $D^x = 0.1$. We have set $a = 1$. The dashed line gives the location of $Q = \pi$, and the dot is at $E(\pi)$. $N = 1000000$.

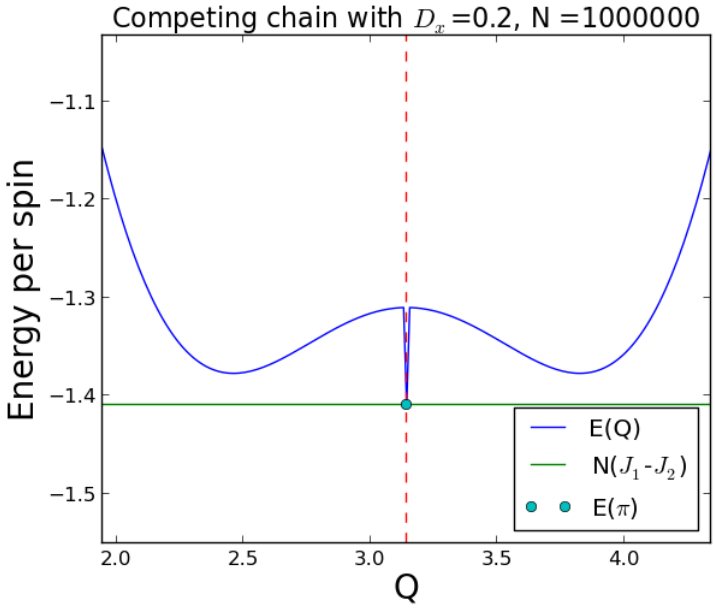

Figure C.8: The energy E versus the angle Q from Eq. (C.18) with $D^x = 0.2$. We have set $a = 1$. The dashed line gives the location of $Q = \pi$, and the dot is at $E(\pi)$. There are two minima of the function. $N = 1000000$.

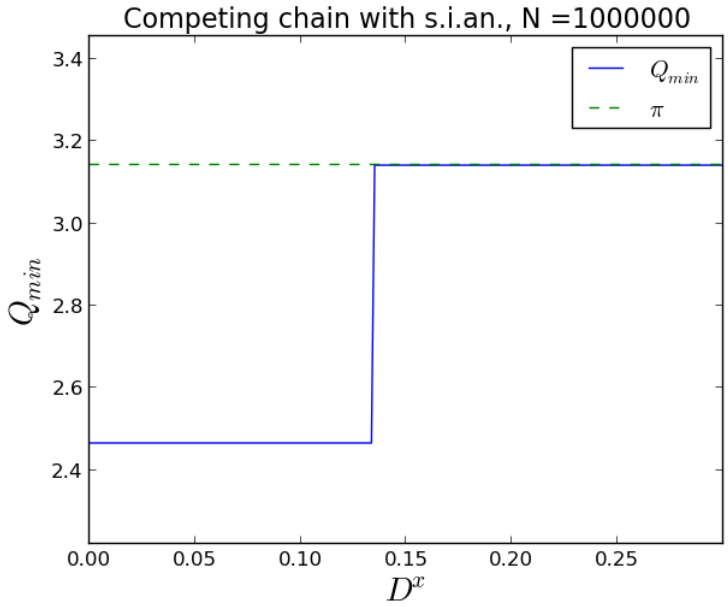

Figure C.9: The value $Q = Q_{min}$ that minimizes the energy E of (C.18) plotted against D^x. For $D^x \gtrapprox 0.13$, $Q_{min} = \pi$. $N = 1000000$.

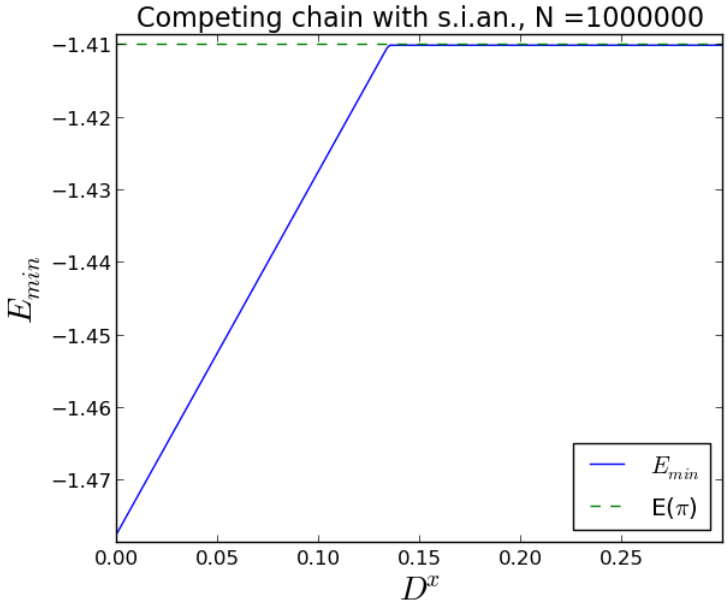

Figure C.10: The lowest energy $E = E_{min}$ of (C.18) as a funciton of D^x. For $D^x \gtrapprox 0.13$, the energy becomes constant. $N = 1000000$.

Table C.7: The value of D^x for which the spins first become one-dimensional for different system sizes N. We denote this single-ion anisotropy by D^x_{ch}. The values were found by locating where $Q_{min} = \pi$ first appeared, and then extracting the corresponding D^y. The resolution is $5 \cdot 10^{-5}$ for all system sizes.

N	10	50	10^2	10^3	10^4	10^6	10^8
D^x_{ch}	0.0382	0.11365	0.1237	0.1331	0.1342	0.1343	0.1343

pull to remove the x-component of the spins. One could imagine setting an angle close to π would be more energetically favourable than forcing the spins to be strictly one-dimensional. However, we study such a large chain that even those angles will eventually add up to yield large x-components in portions of the chain, thereby increasing the energy considerably. This also account for the discontinuity at $Q = \pi$ in figures (C.7) and (C.8). The same goes for any other middle ground angle we could concoct.

In fact, figure (C.7) provides insight into how the system can get stuck in a metastable state. Here, $Q = \pi$ is a metastable state, since it is lower in energy than those surrounding it. Due to the high energy cost of going from $Q = a$ to a nearby state, a system that passes $Q = \pi$ on its way to equilibrium is likely to stay there for a very long time. Of course, this graph only takes states on the form of Eq. (4.1), but it nevertheless provides a valuable visualization of the issue.

Figure (C.10) shows how the minimal energy varies with increasing D^x. The energy increases linearly until it is equal to that of the antiferromagnetic ordering, and after that it remains unchanged for increasing D^x. This agrees with what we found for the angle Q_{min} that minimizes the energy: After $D^x \approx 0.13$, Q_{min} is constant, so $E_{min} = E(Q_{min})$ should be too.

Table (C.7) shows how the emergence of the one-dimensional spins varies with the number of spins N in the chain. The value of D^y where the spins become one-dimensional seems to converge to 0.1343 as $N \to \infty$. Boundary effects obviously play a larger role for smaller system as the spins are few. For larger systems, the boundary effects drowns in the huge contribution from the spins in the middle of the chain. This is evident from Eq. (C.18) too: The couplings are multiplied by factors of $(N-1)$ and $(N-2)$, where the negative terms stems from our open boundary conditions. When N becomes large, these terms will be multiplied by approximately the same factor. This becomes clearer when we consider the average energy E/N: For large N, $(N-1)/N \approx 1$ and $(N-2)/N \approx 1$.

The spins lose their second component already at $D^x = 0.1343$. To arrive at (C.18), we disregarded the spin components in the y-direction as D^y was large. Technically, what we did was setting $D^y = \infty$ so that no y-component could be permissible at all, due to an infinite energy cost. Obviously, the single-ion anisotropy constant in the y-direction is not infinite, but just below two in all of our sources [Ref.]. However, if the second spin component is lost at $D^x = 0.14$, $D^y \approx 2$ should be large enough for the y-component to practically be excluded and our condition to apply well.

Table C.8: The average dot product and absolute value of the spin components for the $J_1 = 2.08$ and $J_2 = 0.67$ for different single-ion anisotropies $D^x_{an} = 0.34\alpha$, $D^y = 1.82\alpha$. The system was a chain of 4000 spins and the temperature set to 12 K.

α	0	1	2	5	10	25	50	75	100
$\mathrm{Av}(\mathbf{S}_i \cdot \mathbf{S}_j)$	-0.5611	-0.6094	-0.6571	-0.7593	-0.8444	-0.9211	-0.9401	-0.9542	-0.9575
$\mathrm{Av}\lvert S^x_i \rvert$	0.4965	0.5182	0.4767	0.3496	0.2664	0.1776	0.1279	0.1053	0.0923
$\mathrm{Av}\lvert S^y_i \rvert$	0.5002	0.3337	0.2597	0.1750	0.1244	0.0805	0.0576	0.0464	0.0404
$\mathrm{Av}\lvert S^z_i \rvert$	0.5046	0.6320	0.7134	0.8576	0.9252	0.9691	0.9842	0.9894	0.9920

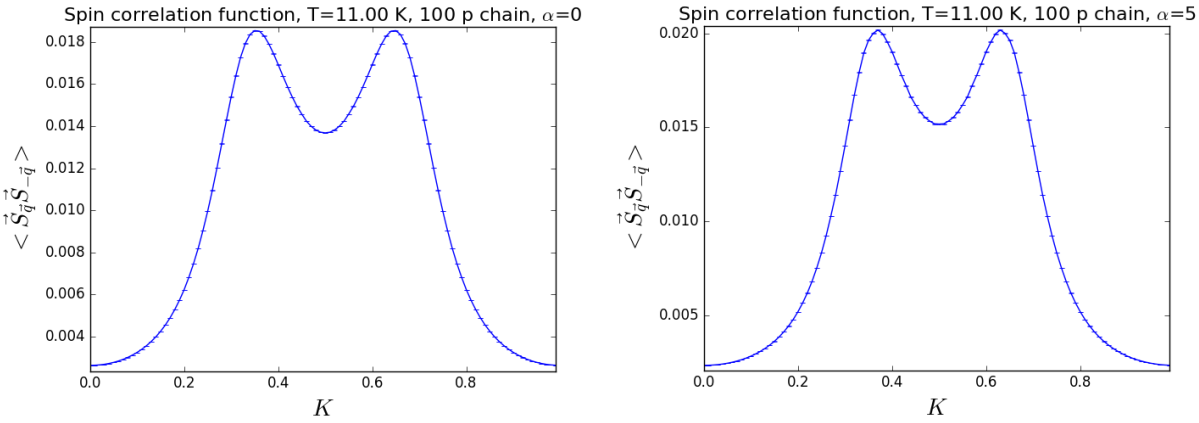

Figure C.11: The spin correlation functions for the 100 spin open chain for varying anisotropy. The couplings are $J_1 = 2.28$ (nearest neighbours) and $J_2 = 0.67$. The single-ion anisotropy is set to $D^x_{an} = 0.34\alpha$ and $D^y_{an} = 1.82\alpha$.

Increasing the single-ion anisotropy

The single-ion anisotropy should have limited effect on the system at temperatures above T≈3.9K, since the thermal energy $E_{th} = k_B T$ is then larger than the energy of the coupling, $D^x_{an} = 0.34$meV. For D^y_{an}, this temperature is 21.1K. Instead of studying how the anisotropy affects the system at low temperatures, which have low acceptance rates, we crank the single-ion anisotropies up and study the system at 12K.

Table (C.8) shows how the average dot product and absolute value of S^z_i varies with the strength of the single-ion anisotropy. The anisotropies given are multiples of those suggested by Jensen et. al.[13]. The simulations were run with 100 000 equilibration sweeps, 100 bins and 100 000 sweeps per bin. The system is slightly affected by the single-ion anisotropy for the smaller couplings, but not enough to cause antiferromagnetic ordering at this temperature. For that to happen, the couplings must be significantly larger than they are. For $\alpha = 25$ onwards, the ordering is pretty close to being antiferromagnetic.

Figure (C.11) shows the spin correlation function for $\alpha = 0$ and $\alpha = 5$. The max-

Table C.9: The peak K of the spin correlation function for different strengths of the single-ion anisotropies $D^x_{an} = 0.34\alpha$ and $D^y = 1.82\alpha$. An open chain of 100 spins was used. K is defined at $\mathbf{Q} = 2\pi/a(0, K, 0)$, where Q is the magnetic ordering wave vector for the system.

α	0	0.1	0.5	1	2	5	7
K	0.35	0.35	0.35	0.36	0.36	0.37	0.38

ima has shifted slightly from one plot to the next. Table (C.9), which lists the ordering wave vectors for different α, confirms this. However, $\mathbf{Q}$ does not depend strongly on the single-ion anisotropy: The difference in K between a system without single-ion anisotropy and a system with seven times the anisotropy of table (3.1) is 0.03. $\mathbf{Q}$ is doubled for the face-centered cubic lattice, so this leaves us with a difference of 0.06. This variation in K is roughly what we observe in figure (1.1), but the change in the single-ion anisotropy is much larger than the change Jensen proposes in table (3.2).

Appendix D

Frustration and ordering wave vectors in the face-centered cubic lattice

Frustration occurs when the couplings of a system favours different configurations, forcing the system to find some middle ground between the options. The frustration can be due to for instance competing couplings, boundary conditions or the lattice structure. An example of the latter is illustrated in figure (D.1), where antiferromagnetic bonds in a triangular structure conflicts. The nearest neighbours in the face-centered cubic lattice make such structures, so we should be alert.

Indeed, triangular structures will often cause frustration, and they will appear in our simulations through the nearest-neighbour bonds in the face-centered cubic lattice. Frustration will not occur in a purely ferromagnetic system, but may still appear with a mix of ferro- and antiferromagnetic bonds in the fcc. This will be demonstrated in the following section. If we have antiferromagnetic bonds in every direction in the face-centered cubic lattice, the system will obviously be frustrated.

Having three nearest neighbour couplings J_{xy}, J_{xz} and J_{yz}, there are three ways to obtain a frustration-free system

1. We set all of the interaction strengths J_{xy}, J_{xz}, J_{yz} to be negative.
2. We set only two of the interaction strengths J_{xy}, J_{xz}, J_{yz} to be positive.
3. We set only one of the interaction strengths J_{xy}, J_{xz}, J_{yz} to be positive.

Figure (D.2) shows the two possible configurations of two half planes for J_{xy} when the bottom left spin points upward. Setting one of the other couplings to be non-zero would determine the configurations uniquely. Turning on a third coupling, however, introduces triangular structures, and frustration might occur. Table (D.1) lists all combinations of couplings and states whether they are frustrated or not. We note that the nearest neighbour couplings of our reference models do not cause frustration on their own.

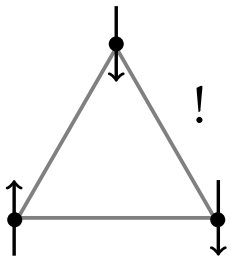

Figure D.1: An illustration of frustration: If we have three spins in a triangular structure, each interacting with each other antiferromagnetically, the antiparallel ordering of spin neighbours is no longer possible. The system must find some other configuration to minimize the energy and is then said to be frustrated. If we remove one of the bonds, however, the frustration would disappear.

Table D.1: An overview of when the system is frustated. 'Yes' informs us that the system is frustrated, while 'No' means that it is frustration free. Since the specific assignment of directions do not matter (if $J_{xy} = 1$,$J_{xz} = -1$ and $J_{xy} = 1$ is frustration-free, so is if $J_{xy} = 1$,$J_{xz} = 1$ and $J_{xy} = -1$), we have only indicated the type. 'AF' stands for antiferromagnetic, $J > 0$, 'F' stands for ferromagnetic, $J < 0$, and 'NO' stands for no interaction, $J = 0$.

Interactions			Frustration
AF	AF	AF	Yes
AF	AF	F	No
AF	AF	NO	No
AF	F	F	Yes
AF	F	NO	No
AF	NO	NO	No

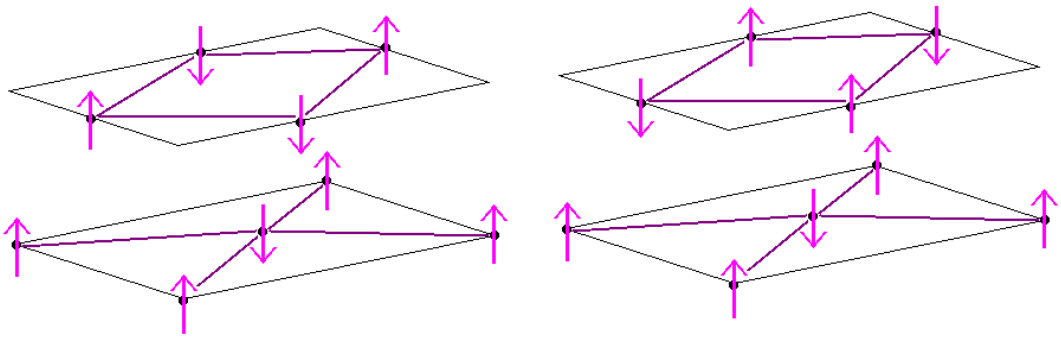

Figure D.2: The interactions between spins in different half planes when $J_{xy} = 1$, $J_{yz} = J_{xz} = 0$. The purple bonds are the antiferromagnetic couplings. There is no frustration in this case. The planes are decoupled, so if one spin in the lower plane is given, there is two possible configurations of these two half-planes.

D.1 The ordering wave vector in the face-centered cubic lattice

We want to find the ordering wave vector for the face-centered cubic lattice with antiferromagnetic couplings. As the pure fcc antiferromagnet is frustrated, we cannot expect an easy analytic expression in that case. Rather, we will study the case of coupled and uncoupled antiferromagnetic layers.

We obtain decoupled antiferromagnetic layers by setting $J = 1$ in one direction and keep the others zero. For an unfrustrated coupling of the layers, we set one of the other J's to be one as well, and keep the last one zero. In this chapter, we have neglected single-ion anisotropy and DM terms.

A Decoupled antiferromagnetic layers

For simplicity, we study $J_{xy} = 1$, $J_{xz} = J_{yz} = 0$. The other cases are analogous as they are related by rotations in an isotropic system.

Figure (D.3) shows two uncoupled antiferromagnetic planes. As mentioned, the ordering wave vector is the vector $\mathbf{q}$ that maximizes $m^2(\mathbf{q})$ or the spin correlation function

$$\langle S^z_{-\mathbf{q}} S^z_{\mathbf{q}} \rangle = \frac{1}{N^2} \sum_{\mathbf{r}} \sum_{\mathbf{r}'} S^z_{\mathbf{r}'} S^z_{\mathbf{r}} e^{i\mathbf{q}\cdot(\mathbf{r}'-\mathbf{r})} \tag{D.1}$$

where N is the number of particles. We can split this expression into three terms:

$$\langle S^z_{-\mathbf{q}} S^z_{\mathbf{q}} \rangle = \langle S^z_{-\mathbf{q}} S^z_{\mathbf{q}} \rangle_{\text{Plane 1}} + \langle S^z_{-\mathbf{q}} S^z_{\mathbf{q}} \rangle_{\text{Plane 2}} + \langle S^z_{-\mathbf{q}} S^z_{\mathbf{q}} \rangle_{\text{Between planes}}$$

Looking at a few terms in $\langle S^z_{-\mathbf{q}} S^z_{\mathbf{q}} \rangle_{\text{Plane 1}}$ should be sufficient to find $\mathbf{q}$. Inserting for the dot products of the spins

$$\langle S^z_{-\mathbf{q}} S^z_{\mathbf{q}} \rangle_{\text{Plane 1}} = 1 + e^{-ai\mathbf{q}\cdot(1,0,0)} + e^{-ai\mathbf{q}\cdot(2,0,0)} - e^{-ai\mathbf{q}\cdot(1/2,1/2,0)} - e^{-ai\mathbf{q}\cdot(1/2,3/2,0)} + e^{-ai\mathbf{q}\cdot(0,1,0)}$$
$$+ e^{-ai\mathbf{q}\cdot(1,1,0)} + e^{-ai\mathbf{q}\cdot(2,1,0)} - e^{-ai\mathbf{q}\cdot(1/2,3/2,0)} - e^{-ai\mathbf{q}\cdot(3/2,3/2,0)}$$
$$+ e^{-ai\mathbf{q}\cdot(0,2,0)} + e^{-ai\mathbf{q}\cdot(1,2,0)} + e^{-ai\mathbf{q}\cdot(2,2,0)} + \dots$$

$\langle S^z_{-\mathbf{q}} S^z_{\mathbf{q}} \rangle$ is maximized if every term is one. This is achieved if the exponents are $2\pi n$ for spins pointing in the same direction and πn with $n =$ odd for spins pointing in opposite direction. Two vectors fullfil this

$$-i\mathbf{q} \cdot a(1,0,0) = -i\frac{2\pi}{a}(1,0,0) \cdot a(1,0,0) = -2\pi i$$

$$-i\mathbf{q} \cdot a(1,0,0) = -i\frac{2\pi}{a}(0,1,0) \cdot a(1,0,0) = 0$$

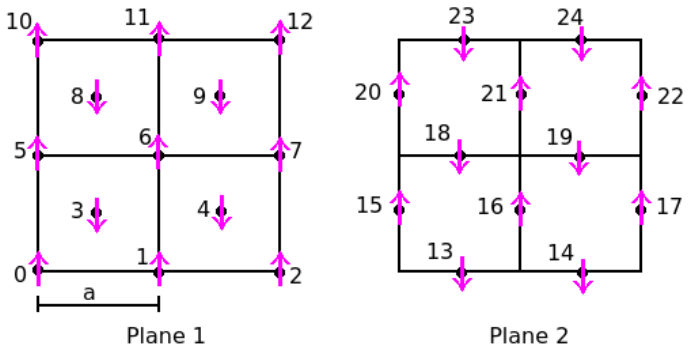

Figure D.3: Antiferromagnetic half planes in the fcc. As the planes are uncoupled, all the spins in one plane could just as well be flipped and result in a valid configuration. Two planes and Ising spins are shown for a better intuitive understanding.

Both of these yield a positive sign in total, as do applying them to one of the terms with negative sign:

$$-i\mathbf{q}\cdot a(1/2,3/2,0) = -i\frac{2\pi}{a}(1,0,0)\cdot a(1/2,3/2,0) = -\pi i$$

$$-i\mathbf{q}\cdot a(1/2,3/2,0) = -i\frac{2\pi}{a}(0,1,0)\cdot a(1/2,3/2,0) = -3\pi i$$

All antiparallel spins in a layer are separated by half-integer coordinates and all parallel spins are separated by integer coordinates, so this generalizes to all half planes.

So for an antiferromagnetic plane, the two order vectors are $\frac{2\pi}{a}(1,0,0)$ and $\frac{2\pi}{a}(0,1,0)$. However, as the spins are decoupled and randomness from layer to layer ensues, the magnitude will not be quite as large as one could expect. Due to this randomness, a component in the last direction will not affect the result that much. We can thus expect order vectors on the form:

$$\frac{2\pi}{a}(1,0,\tilde{q}_z)$$

$$\frac{2\pi}{a}(0,1,\tilde{q}_z)$$

Similar results will hold for $J_{xy}=0$, $J_{yz}=1$, $J_{xz}=0$, and $J_{xy}=J_{yz}=0$, $J_{xz}=1$. The results of this section are tested in Appendix D.

B Coupled antiferromagnetic layers

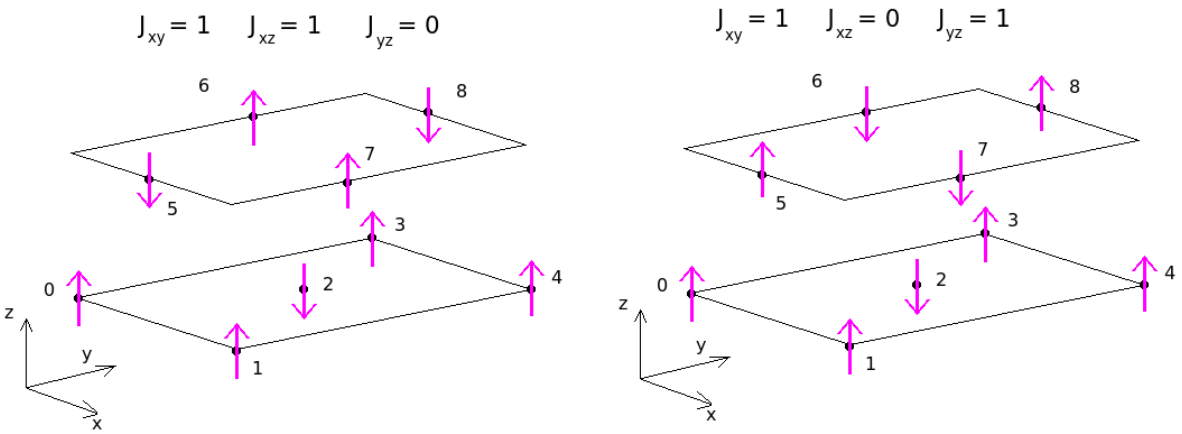

Figure D.4: Antiferromagnetic half planes diagonal to the xy-plane in the fcc, coupled by $J_{xz} = 1$ (left) and $J_{yz} = 1$ (right).

Table D.2: The positions of the spins in the two half planes. a is the grid length.

Index	(x,y,z)	Index	(x,y,z)	Index	(x,y,z)
0	(0,0,0)	3	a(0,1,0)	6	$a(0, \frac{1}{2}, \frac{1}{2})$
1	a(1,0,0)	4	a(1,1,0)	7	$a(1, \frac{1}{2}, \frac{1}{2})$
2	$a(\frac{1}{2}, \frac{1}{2}, 0)$	5	$a(\frac{1}{2}, 0, \frac{1}{2})$	8	$a(\frac{1}{2}, 1, \frac{1}{2})$

Due to the system's isotropy, we consider two cases, $J_{xy} = 1$, $J_{yz} = 1$, $J_{xz} = 0$, and $J_{xy} = 1$, $J_{yz} = 0$, $J_{xz} = 1$. As we have already found the order vectors for the separate layers, we only need to consider terms containing spins from both planes, i.e. $\mathbf{S}_0\mathbf{S}_5 e^{i\mathbf{q}\cdot(\mathbf{r}_0-\mathbf{r}_5)}$. Referring to table (D.2) and inserting:

$$\langle S^z_{-\mathbf{q}} S^z_{\mathbf{q}} \rangle_{\text{Between planes}} = \mathbf{S}_0\mathbf{S}_5 e^{-ai\mathbf{q}\cdot\left(\frac{1}{2},0,\frac{1}{2}\right)} + \mathbf{S}_0\mathbf{S}_6 e^{-ai\mathbf{q}\cdot\left(0,\frac{1}{2},\frac{1}{2}\right)}$$

$$+\mathbf{S}_0\mathbf{S}_7 e^{-ai\mathbf{q}\cdot\left(1,\frac{1}{2},\frac{1}{2}\right)} + \mathbf{S}_0\mathbf{S}_8 e^{i\mathbf{q}\cdot\left(\frac{1}{2},1,\frac{1}{2}\right)}$$

Again, we want the exponent to be $\pm 2\pi n i$ if the spins point in the same direction, and $\pm(2n-1)\pi i$ if they are oppositely directed. In the case of $J_{xy} = 1 = J_{xz} = 1$, $J_{yz} = 0$, $\mathbf{S}_0 \cdot \mathbf{S}_5 = -1$ and $\mathbf{S}_0 \cdot \mathbf{S}_6 = 1$.

$$\mathbf{S}_0\mathbf{S}_5 \exp\left[-i\mathbf{q}\cdot a\left(\frac{1}{2},0,\frac{1}{2}\right)\right] = -\exp\left[-i\frac{2\pi}{a}(1,0,0)\cdot a\left(\frac{1}{2},0,\frac{1}{2}\right)\right] = -\exp\left[-i\pi\right] = +1$$

$$\mathbf{S}_0\mathbf{S}_6 e^{-i\mathbf{q}\cdot a\left(0,\frac{1}{2},\frac{1}{2}\right)} = \exp\left[-i\frac{2\pi}{a}(1,0,0)\cdot a\left(0,\frac{1}{2},\frac{1}{2}\right)\right] = +1$$

Luckily, this vector agrees with one of those for the antiferromagnetic decoupled xy-planes. So $J_{xy} = J_{xz} = 1$, $J_{yz} = 0$ has the order vector $\frac{2\pi}{a}(1,0,0)$. With no freedom in the spin orientation from plane to plane, this is the only $\mathbf{q}$-vector for which we expect to see a significant value of the spin correlation function.

For $J_{xy} = 1$, $J_{xz} = 0$, $J_{yz} = 1$, the signs are opposite:

$$\mathbf{S}_0\mathbf{S}_5 \exp\left[-i\mathbf{q}\cdot a\left(\frac{1}{2},0,\frac{1}{2}\right)\right] = \exp\left[-i\frac{2\pi}{a}(0,1,0)\cdot a\left(\frac{1}{2},0,\frac{1}{2}\right)\right] = +1$$

$$\mathbf{S}_0\mathbf{S}_6 e^{-i\mathbf{q}\cdot a\left(0,\frac{1}{2},\frac{1}{2}\right)} = -\exp\left[-i\frac{2\pi}{a}(0,1,0)\cdot a\left(0,\frac{1}{2},\frac{1}{2}\right)\right] = -\exp\left[-i\pi\right] = +1$$

So the order vector for $J_{xy} = 1$, $J_{xz} = 0$, $J_{yz} = 1$ is $\mathbf{q} = \frac{2\pi}{a}(0,1,0)$.

Due to the symmetry of the system, we realize that the order vector for $J_{xy} = 0$, $J_{xz} = 1$, $J_{yz} = 1$ is $\mathbf{q} = \frac{2\pi}{a}(0,0,1)$. This should be easy to show following the procedure above.

D.2 Numerical results, fcc, configuration and ordering wave vector

The systems tested are 6x6x6 fcc. The simulations were run for $\beta = 10$, a very low temperature, with 10000 equilibration sweeps and 100 bins with 1000 Monte Carlo sweeps in each.

Table D.3: The number of spins not antiparallel for different planes using two different seeds, which are referenced by '59' and '79' in the second row. We have antiferromagnetic couplings in one plane, and no coupling in the others. The AF coupling is given in the upper left corner of each subtable (separated by double lines). By 'not antiparallel' we refer to neighbouring spins with with dot product > 0. There are 2592 pairs of neighbours in total.

$J_{xy} = 1$			$J_{xz} = 1$			$J_{yz} = 1$		
	59	79		59	79		59	79
yz	716	372	yz	370	224	yz	0	0
xz	24	372	xz	0	0	xz	238	302
xy	0	0	xy	372	534	xy	500	460

A One antiferromagnetic coupling

A test of the configuration

Looking at the spin configuration after a simulation at low temperature, we are interested in finding out whether neighbouring spins are antiparallel, as they should be if our system is antiferromagnetic. In this chapter, we have used simulations with $\beta = 50$.

We define the xy-planes as those in which $z_i = z_j$ for any two points i, j in the plane. If their dot product is larger than zero, we say that they are 'not antiparallel'. We do the same for xz- and yz-planes as well. Since the test is crude and we are interested in ratios and rough estimates, we have not bothered compensating for double counting in the procedure.

Table (D.3) contains the number of not antiparallel spins in all the Carthesian planes for an antiferromagnetic coupling in different planes. It is evident that if we have an antiferromagnetic coupling in one plane, then there are no 'not antiparallel' spins in that plane. This is exactly what we expected, since a system with antiferromagnetic couplings should consist of antiparallel spins at very low temperatures. The other planes have some spins that are 'not antiparallel', which is to be expected as there is no interaction between their pairs, and thus no favoured configurations.

Furthermore, it is of interest to look at the magnitude of the dot product in each plane in our three cases. Expecting antiferromagnetism, we hope that the dot products are all close to -1, and indeed they are, the least negative ones being:

1. $J_{xy} = J_{xz} = 0$, $J_{yz} = 1$: yz-planes: $\max(\mathbf{S}_i \cdot \mathbf{S}_j) < -0.95$
2. $J_{xy} = J_{yz} = 0$, $J_{xz} = 1$: xz-planes: $\max(\mathbf{S}_i \cdot \mathbf{S}_j) < -0.93$
3. $J_{xz} = J_{yz} = 0$, $J_{xy} = 1$: xy-planes: $\max(\mathbf{S}_i \cdot \mathbf{S}_j) < -0.93$

with i, j being neighbours in the plane. The ordering in the plane of the coupling is indeed antiferromagnetic.

Table D.4: The order vectors for $J_{xy} = 1$, $J_{xz} = J_{yz} = 0$. The simulation was run for $\beta = 10$, 10000 equilibration sweeps and 100 bins with 1000 Monte Carlo sweeps in each.

n	q_x	q_y	q_z	$\langle \mathbf{S_q S_{-q}} \rangle$
126	0	2π	0	0.23007
111	2π	0	0	0.15662
118	2π	0	$2\pi/3$	0.15662
140	0	2π	$4\pi/3$	0.13469
125	2π	0	$4\pi/3$	0.12734
133	0	2π	$2\pi/3$	0.12734

Table D.5: The order vectors for $J_{xz} = 1$, $J_{xy} = J_{yz} = 0$. The simulation was run for $\beta = 10$, 10000 equilibration sweeps and 100 bins with 1000 lattice sweeps in each.

n	q_x	q_y	q_z	$\langle \mathbf{S_q S_{-q}} \rangle$
63	0	$2\pi/3$	2π	0.18141
195	2π	$4\pi/3$	0	0.18141
111	2π	0	0	0.173135
21	0	0	2π	0.14068
105	0	$4\pi/3$	2π	0.14068
153	2π	$2\pi/3$	0	0.11730

The order vector

Due to the decoupling of the plane in this instance, we expect our order vector to be somewhat muddy. Indeed, the spin correlation function takes a somewhat large value for several **q**'s, as seen in tables (D.4), (D.5) and (D.6). The six vectors listed in each table are the ones corresponding to the largest values of the spin correlation function, the next in line being approximately 0.001 in all three cases. The results are consistent with those outlined in the theory section.

B Two antiferromagnetic couplings

Table D.6: The order vectors for $J_{yz} = 1$, $J_{xy} = J_{xz} = 0$. The simulation was run for $\beta = 10$, 10000 equilibration sweeps and 100 bins with 1000 Monte Carlo sweeps in each.

n	q_x	q_y	q_z	$\langle \mathbf{S_q S_{-q}} \rangle$
126	0	2π	0	0.22010
58	$2\pi/3$	0	2π	0.17781
200	$4\pi/3$	2π	0	0.17781
21	0	0	2π	0.12012
95	$4\pi/3$	0	2π	0.11853
163	$2\pi/3$	2π	0	0.11853

Table D.7: The order vectors with antiferromagnetic couplings in two directions, and no interaction in the last direction. Note that the spin correlation function is large in all cases, more so for the cases where the antiferromagnetism is equally strong in both directions.

J_{xy}	J_{xz}	J_{yz}	n	q_x	q_y	q_z	$\langle \mathbf{S_q S_{-q}} \rangle$
1	1	0	111	2π	0	0	0.96974
1	0.1	0	111	2π	0	0	0.93049
0	1	1	21	0	0	2π	0.96983
1	0	1	126	0	2π	0	0.96977

Table (D.7) shows that with two antiferromagnetic couplings, the order vector points along one of the q-axes. The spin correlation function is large in all cases. The second largest value of the spin correlation function was about $5 \cdot 10^{-4}$ for both J's being one and 0.004 for $J_{xy} = 1$, $J_{xz} = 0.1$, $J_{yz} = 0$, i.e. the second line in the table. We see that the order vector for $J_{xy} = J_{xz} = 1$, $J_{yz} = 0$ is that common to both $J_{xy} = 1$, $J_{xz} = J_{yz} = 0$ and $J_{xz} = 1$, $J_{xy} = J_{yz} = 0$, and similarly for the other choices of J's. The results are consistent with those outlined in the theory section.

Appendix E

Fcc: The incommensurate ordering is the minima

We want to confirm that Eq. (6.3) indeed gives the minima:

$$\frac{\partial^2 E}{\partial Q_y^2} = -a^2 \left(\frac{1}{4} \left(J_{xy} N_{xy} + J_{yz} N_{yz} \right) \cos\left(\frac{Q_y a}{2} \right) + J_y N_y \left(2\cos^2\left(\frac{Q_y a}{2} \right) - 1 \right) \right)$$

Inserted for $Q_y a = 2\pi n$

$$\begin{aligned} \left. \frac{\partial^2 E}{\partial Q_y^2} \right|_{Q_y = \frac{2\pi n}{N}} &= -a^2 \left(\frac{1}{4} \left(J_{xy} N_{xy} + J_{yz} N_{yz} \right) (-1)^n + J_y N_y \right) \\ &= -a^2 N \left(\frac{1}{2} \left(J_{xy} + J_{yz} \right) (-1)^n + J_y \right) \end{aligned} \tag{E.1}$$

where the last equality holds for periodic boundary conditions or in the limit of $N_{xy} = N_{yz} = 2N$, $N_y = N$. We restrict ourselves to $J_{xy}, J_{yz}, J_y > 0$, in accordance with our reference models. For even n, Eq. (E.1) is always negative, so ferromagnetic ordering in the y-direction yields a maxima of the energy. Antiferromagnetic ordering, on the other hand

$$\left. \frac{\partial^2 E}{\partial Q_y^2} \right|_{Q_y = \frac{2\pi n}{N},\ \text{n odd}} = -a^2 N \left(J_y - \frac{1}{2} (J_{xy} + J_{yz}) \right) \tag{E.2}$$

yields a minima if

$$J_y < \frac{1}{2} \left(J_{xy} + J_{yz} \right) \tag{E.3}$$

For which the incommensurate solution is no longer available. The value of the energy for this extremal point is

$$E = A + J_y N_y - \left(J_{xy} N_{xy} + J_{yz} N_{yz}\right) \tag{E.4}$$

Inserting for the incommensurate angle (Eq. (6.3)) into the double derivative gives

$$\frac{\partial^2 E}{\partial Q_y^2} = a^2 J_y N_y \left[1 - \left(\frac{J_{xy} N_{xy} + J_{yz} N_{yz}}{4 J_y N_y}\right)^2\right] = \begin{cases} > 0 & \text{if } J_y > 0: \quad \text{Minima} \\ < 0 & \text{if } J_y < 0: \quad \text{Maxima} \end{cases}$$

So just as for the chain, (6.3) yields a minima if $J_y > 0$. The energy is

$$E = A - \frac{(J_{xy} N_{xy} + J_{yz} N_{yz})^2}{8 J_y N_y} - J_y N_y \tag{E.5}$$

Appendix F

Finite size scaling of crossing points

For large system sizes L, the value of a quantity A, depending on the size of the system and the distance δ from the critical point scales as [10]

$$A(\delta, L) = L^{-\kappa/\nu} f\left(\delta L^{1/\nu}, L^{-\omega}\right) \tag{F.1}$$

where κ determines the behaviour of A by $A \propto |\delta|^{\kappa}$ in the thermodynamic limit. This expression can be Taylor expanded to [10]

$$A(\delta, L) = L^{-\kappa/\nu}\left(a_0 + a_1 \delta L^{1/\nu} + b_1 L^{-\omega} + \cdots\right) \tag{F.2}$$

The crossing of the Binder cumulants approach the critical temperature as the system sizes tends to infinity. In order to extrapolate our data it is advantageous to know how the crossing depends on L. To achieve this, we need to equate Eq. (F.2) for two different system sizes. In the spirit of our analysis, we investigate the crossing points between $L_1 = L$ and $L_2 = L + \Delta L$, keeping in mind that L is large, so $\frac{\Delta L}{L}$ should be a small quantity. We assume L is sufficiently large to neglect the higher-order terms in A. The two sides of the equation becomes

$$A(\delta, L_1) = a_0 L^{-\kappa/\nu} + a_1 \delta L^{(1-\kappa)/\nu} + b_1 L^{-\omega-\kappa/\nu}$$

$$A(\delta, L_2) = (L + \Delta L)^{-\kappa/\nu}\left(a_0 + a_1 \delta \left(L + \Delta L\right)^{1/\nu} + b_1 \left(L + \Delta L\right)^{-\omega}\right)$$

$$= L^{-\kappa/\nu}\left(1 + \frac{\Delta L}{L}\right)^{-\kappa/\nu}\left(a_0 + a_1 \delta L^{1/\nu}\left(1 + \frac{\Delta L}{L}\right)^{1/\nu} + b_1 L^{-\omega}\left(1 + \frac{\Delta L}{L}\right)^{-\omega}\right)$$

We find the general Taylor expansion

$$\left(1 + \frac{\Delta L}{L}\right)^{\alpha} = 1 + \alpha \frac{\Delta L}{L} + \cdots \tag{F.3}$$

for which we keep only the first two terms. Using Eq. (F.3) to simplify $A(\delta, L_2)$ and denoting the location of the crossing by δ^*, we find where the two graphs intersect.

$$A(\delta^*, L_1) - A(\delta^*, L_2) = -a_1\delta^*\frac{1}{\nu}\frac{\Delta L}{L}L^{(1-\kappa)/\nu} + b_1\omega\frac{\Delta L}{L}L^{-\omega-\kappa/\nu}$$
$$+a_0\frac{\kappa}{\nu}\frac{\Delta L}{L}L^{-\kappa/\nu} + a_1\delta^*\frac{\kappa}{\nu}\frac{\Delta L}{L}L^{(1-\kappa)/\nu} + b_1\frac{\kappa}{\nu}\frac{\Delta L}{L}L^{-\omega-\kappa/\nu}$$
$$= a_1\delta^*\frac{\Delta L}{L}\left(\frac{\kappa-1}{\nu}\right)L^{(1-\kappa)/\nu} + b_1\frac{\Delta L}{L}\left(\omega+\frac{\kappa}{\nu}\right)L^{-\omega-\kappa/\nu} + a_0\frac{\Delta L}{L}\frac{\kappa}{\nu}L^{-\kappa/\nu} = 0$$

Rearranging

$$\delta^* = \frac{a_0}{a_1}\frac{\kappa/\nu}{(1-\kappa)/\nu}L^{-1/\nu} + \frac{b_1}{a_1}\frac{\omega+\kappa/\nu}{(1-\kappa)/\nu}L^{-\omega-1/\nu}$$

From section 2.9, we know that $\kappa = 0$ for the Binder cumulant, so the first term vanishes

$$\delta^* = \frac{b_1}{a_1}\omega\nu L^{-\omega-1/\nu} \propto L^{-\omega-1/\nu} \tag{F.4}$$

F.1 Keeping second order terms in A

The previous results were found by Taylor-expanding Eq. (F.1) to first order, yielding Eq. (F.2) as a starting point for our calculations. Assuming L is large enough to render $\frac{\Delta L}{L}$ a small quantity, but small enough to merit a second-order Taylor expansion of Eq. (F.1), we obtain

$$A(\delta, L) = L^{-\kappa/\nu}\left(a_0 + a_1\delta L^{1/\nu} + a_2\delta^2 L^{2/\nu} + b_1L^{-\omega} + b_2L^{-2\omega} + c_1\delta L^{1/\nu-\omega} + \cdots\right) \tag{F.5}$$

Since $L^{-\omega}$ is a small quantity, we neglect the b_2-term as it contains $L^{-\omega}$. Our terms become:

$$A(\delta, L_1) = a_0L^{-\kappa/\nu} + a_1\delta L^{(1-\kappa)/\nu} + a_2\delta^2L^{(2-\kappa)/\nu} + b_1L^{-\kappa/\nu-\omega} + c_1\delta L^{(1-\kappa)/\nu-\omega}$$

$$A(\delta, L_2) = L^{-\kappa/\nu}\left(1+\frac{\Delta L}{L}\right)^{-\kappa/\nu}\left[a_0 + a_1\delta L^{1/\nu}\left(1+\frac{\Delta L}{L}\right)^{1/\nu} + a_2\delta^2L^{2/\nu}\left(1+\frac{\Delta L}{L}\right)^{2/\nu}\right.$$
$$\left.+b_1L^{-\omega}\left(1+\frac{\Delta L}{L}\right)^{-\omega} + c_1\delta L^{1/\nu-\omega}\left(1+\frac{\Delta L}{L}\right)^{1/\nu-\omega}\right]$$

Keeping only terms up to first order

$$A(\delta, L_2) = a_0 L^{-\kappa/\nu} + a_1 \delta L^{(1-\kappa)/\nu} + a_2 \delta^2 L^{(2-\kappa)/\nu} + b_1 L^{-\kappa/\nu-\omega} + c_1 \delta L^{(1-\kappa)/\nu-\omega}$$
$$+a_1\delta\frac{1}{\nu}\frac{\Delta L}{L}L^{(1-\kappa)/\nu} - b_1\omega\frac{\Delta L}{L}L^{-\omega-\kappa/\nu} - a_0\frac{\kappa}{\nu}\frac{\Delta L}{L}L^{-\kappa/\nu} - a_1\delta\frac{\kappa}{\nu}\frac{\Delta L}{L}L^{(1-\kappa)/\nu} - b_1\frac{\kappa}{\nu}\frac{\Delta L}{L}L^{-\omega-\kappa/\nu}$$
$$-a_2\delta^2\frac{\kappa}{\nu}\frac{\Delta L}{L}L^{(2-\kappa)/\nu} - c_1\delta\frac{\kappa}{\nu}\frac{\Delta L}{L}L^{(1-\kappa)/\nu-\omega} + a_2\delta^2\frac{2}{\nu}\frac{\Delta L}{L}L^{(2-\kappa)/\nu} + c_1\delta(1/\nu-\omega)\frac{\Delta L}{L}L^{(1-\kappa)/\nu-\omega}$$

The difference then becomes

$$A(\delta^*, L_2) - A(\delta^*, L_1) = (\delta^*)^2 a_2 \frac{2-\kappa}{\nu}\frac{\Delta L}{L}L^{(2-\kappa)/\nu} + \delta^*\left[a_1 L^{(1-\kappa)/\nu}\frac{1-\kappa}{\nu}\frac{\Delta L}{L}\right.$$
$$\left.+c_1 L^{(1-\kappa)/\nu-\omega}\left(\frac{1-\kappa}{\nu}-\omega\right)\frac{\Delta L}{L}\right] - b_1 L^{-\omega-\kappa/\nu}\left(\omega+\frac{\kappa}{\nu}\right)\frac{\Delta L}{L} - a_0 L^{-\kappa/\nu}\frac{\kappa}{\nu}\frac{\Delta L}{L} = 0$$

Solving the second order equation

$$\delta^* = \frac{1}{2a_2\frac{2-\kappa}{\nu}\frac{\Delta L}{L}L^{(2-\kappa)/\nu}}\left[-a_1 L^{(1-\kappa)/\nu}\frac{1-\kappa}{\nu}\frac{\Delta L}{L} - c_1 L^{(1-\kappa)/\nu-\omega}\left(\frac{1-\kappa}{\nu}-\omega\right)\frac{\Delta L}{L}\right.$$
$$\pm\left(a_1^2 L^{2(1-\kappa)/\nu}\left(\frac{1-\kappa}{\nu}\right)^2\left(\frac{\Delta L}{L}\right)^2 + 2a_1c_1 L^{2(1-\kappa)/\nu-\omega}\frac{1-\kappa}{\nu}\left(\frac{1-\kappa}{\nu}-\omega\right)\left(\frac{\Delta L}{L}\right)^2\right.$$
$$+c_1^2 L^{2(1-\kappa)/\nu-2\omega}\left(\frac{1-\kappa}{\nu}-\omega\right)^2\left(\frac{\Delta L}{L}\right)^2 + 4a_2b_1 L^{2(1-\kappa)/\nu-\omega}\frac{2-\kappa}{\nu}\left(\omega+\frac{\kappa}{\nu}\right)\left(\frac{\Delta L}{L}\right)^2$$
$$\left.\left.+4a_0a_2 L^{2(1-\kappa)/\nu}\frac{2-\kappa}{\nu}\frac{\kappa}{\nu}\left(\frac{\Delta L}{L}\right)^2\right)^{1/2}\right]$$

We can extract a factor $L^{2/\nu}\left(\frac{\Delta L}{L}\right)^2$ from the expression under the square root. This allows us to separate a factor of $L^{1/\nu}\frac{\Delta L}{L}$ from the square bracket, which in turn will cancel some of the factors in the denominator. The expression simplifies to

$$\delta^* = -\frac{a_1}{a_2}\frac{1-\kappa}{4-2\kappa}L^{-(1+\kappa)/\nu} - \frac{c_1}{a_2}\frac{1-\kappa-\omega\nu}{4-2\kappa}L^{-(1+\kappa)/\nu-\omega}$$
$$\pm\frac{\nu L^{-1/\nu}}{2a_2(2-\kappa)}\left(a_1^2 L^{-2\kappa/\nu}\left(\frac{1-\kappa}{\nu}\right)^2 + 2a_1c_1 L^{-2\kappa/\nu-\omega}\frac{1-\kappa}{\nu}\left(\frac{1-\kappa}{\nu}-\omega\right)\right.$$
$$\left.+c_1^2 L^{-2\omega-2\kappa/\nu}\left(\frac{1-\kappa}{\nu}-\omega\right)^2\right.$$

$$+4a_2b_1L^{-2\kappa/\nu-\omega}\frac{2-\kappa}{\nu}\left(\omega+\frac{\kappa}{\nu}\right)+4a_0a_2L^{-2\kappa/\nu}\frac{2-\kappa}{\nu}\frac{\kappa}{\nu}\Bigg)^{1/2}$$

Setting $\kappa = 0$, as is the case for the Binder cumulant

$$\delta^* = -\frac{a_1}{4a_2}L^{-1/\nu} - \frac{c_1}{a_2}\frac{1-\omega\nu}{4}L^{-1/\nu-\omega}$$

$$\pm\frac{\nu L^{-1/\nu}}{4a_2}\left(\frac{a_1^2}{\nu^2}+\left[2a_1c_1\frac{1}{\nu}\left(\frac{1}{\nu}-\omega\right)+4a_2b_1\frac{2\omega}{\nu}\right]L^{-\omega}+c_1^2\left(\frac{1}{\nu}-\omega\right)^2L^{-2\omega}\right)^{1/2}$$

This expression is not easy to analyse due to the square root. We might however assume that a_2 and c_1 are small and Taylor-expand.

$$\delta^* = -\frac{a_1}{4a_2}L^{-1/\nu} - \frac{c_1}{a_2}\frac{1-\omega\nu}{4}L^{-1/\nu-\omega}$$

$$\pm\frac{\nu L^{-1/\nu}}{4a_2}\sqrt{\frac{a_1^2}{\nu^2}}\left(1+\frac{\nu^2}{a_1^2}\left[\left(2a_1c_1\frac{1}{\nu}\left(\frac{1}{\nu}-\omega\right)+4a_2b_1\frac{2\omega}{\nu}\right)L^{-\omega}+c_1^2\left(\frac{1}{\nu}-\omega\right)^2L^{-2\omega}\right]\right)^{1/2}$$

As a_2 and c_1 enter as a factor in each term of the square bracket, we assume that quantity to be small. Applying Eq. (F.3) to the root, the expression simplifies to

$$\delta^* = -\frac{a_1}{4a_2}L^{-1/\nu} - \frac{c_1}{a_2}\frac{1-\omega\nu}{4}L^{-1/\nu-\omega}$$

$$\pm\frac{L^{-1/\nu}|a_1|}{4a_2}\left(1+\frac{\nu^2}{2a_1^2}\left[\left(2a_1c_1\frac{1}{\nu}\left(\frac{1}{\nu}-\omega\right)+4a_2b_1\frac{2\omega}{\nu}\right)L^{-\omega}+c_1^2\left(\frac{1}{\nu}-\omega\right)^2L^{-2\omega}\right]\right)$$

Gathering the terms

$$\delta^* = \left(-a_1 \pm |a_1|\right)\frac{L^{-1/\nu}}{4a_2}$$

$$+\left(-\frac{c_1}{a_2}\frac{1-\omega\nu}{4}\pm\frac{|a_1|}{4a_2}\left(\frac{c_1}{a_1\nu}\left(\frac{1}{\nu}-\omega\right)+\frac{4a_2b_1\nu\omega}{a_1^2}\right)\right)L^{-1/\nu-\omega}$$

$$\pm\frac{|a_1|c_1^2\nu^2}{8a_2a_1^2}\left(\frac{1}{\nu}-\omega\right)^2L^{-1/\nu-2\omega}$$

Where $2L^{-1/\nu-2\omega}$ is so small that the last term can be omitted. While we in the previous section approximated the Binder cumulants by lines, this δ^* was found by solving a quadratic equation and consequently offers two solutions. Since the aim is to obtain a better approximation of the same crossing, we want to study the answer that is closest to Eq. (F.4), the intersection between the lines. Whether we find that answer by choosing the plus sign or the minus sign depends on the sign of a_1, which we do not

know. In any case, the solution where the $L^{-1/\nu}$-term vanishes is obviously closer to Eq. (F.4) than the solution where it does not. If it $a_1 < 0$, our expression for δ^* is

$$\delta^* = -\left(\frac{c_1}{a_2}\frac{1-\omega\nu}{4} + \frac{|a_1|}{4a_2}\left(\frac{c_1}{a_1\nu^2} - \frac{c_1\omega}{a_1\nu} + \frac{4a_2b_1\nu\omega}{a_1^2}\right)\right)L^{-1/\nu-\omega}$$

while if $a_1 > 0$

$$\delta^* = \left(-\frac{c_1}{a_2}\frac{1-\omega\nu}{4} + \frac{|a_1|}{4a_2}\left(\frac{c_1}{a_1\nu^2} - \frac{c_1\omega}{a_1\nu} + \frac{4a_2b_1\nu\omega}{a_1^2}\right)\right)L^{-1/\nu-\omega}$$

So even when taking into account the small second-order corrections to A, the Binder cumulant crossings still depend on the system size L as

$$\delta^* \propto L^{-1/\nu-\omega} \tag{F.6}$$

The only difference brought by the extra terms being a change in the prefactor, which is of no interest to us.

F.2 The value of $A(\delta, L)$ at δ^*

For both cases, $\delta^* \propto L^{-1/\nu-\omega}$. We insert into A, remembering that $\kappa = 0$. For the first-order expansion in δ

$$A(\delta^*, L) = a_0 + \bar{a}_1 L^{-\omega} + b_1 L^{-\omega} + \cdots = a + bL^{-\omega} + \cdots$$

where we have renamed prefactors like there were no tomorrow.

Insertion into the second-order expansion yields the same result

$$A(\delta^*, L) = a_0 + \tilde{a}_1 L^{-\omega} + b_1 L^{-\omega} + \tilde{c}_1 L^{-2\omega} + \tilde{a}_2 L^{-2\omega} + \cdots = a + bL^{-\omega} + \cdots \tag{F.7}$$

as we neglect terms of $L^{-2\omega}$.

F.3 The derivative of A

For further analysis, we may take the derivative of A.

$$s(\delta, L) = \frac{dA(\delta, L)}{d\delta} = a_1 L^{(1-\kappa)/\nu} + c_1 L^{(1-\kappa)/\nu-\omega} + a_2\delta L^{(2-\kappa)/\nu} + \cdots \tag{F.8}$$

We have renamed $2a_2 \to a_2$ since a_2 is an unknown constant anyway. We are interested in the crossing, which we found to scale with L as $\delta^* \propto L^{-1/\nu-\omega}$. Inserting into Eq. (F.8)

$$s\left(\delta^*, L\right) = a_1 L^{(1-\kappa)/\nu} + c_1 L^{(1-\kappa)-\omega} + \tilde{a}_2 L^{(1-\kappa)/\nu-\omega} + \cdots$$
$$= a_1 L^{(1-\kappa)/\nu}\left(1 + \tilde{b}_1 L^{-\omega} + \cdots\right)$$

Which is what [10] also found. We compare systems of size $L_1 = L$ and $L_2 = L + \Delta L$. Enforcing $\kappa = 0$, the derivatives take the form

$$s\left(\delta^*, L_1\right) = a_1 L^{1/\nu}\left(1 + \tilde{b}_1 L^{-\omega} + \cdots\right)$$

$$s\left(\delta^*, L_2\right) = a_1 L^{1/\nu}\left(1 + \frac{\Delta L}{L}\right)^{1/\nu}\left(1 + \tilde{b}_1 L^{-\omega}\left(1 + \frac{\Delta L}{L}\right)^{-\omega} + \cdots\right)$$

Taking the logarithm

$$\ln\left[s\left(\delta^*, L_1\right)\right] = \ln a_1 + \frac{1}{\nu}\ln L + \ln\left(1 + \tilde{b}_1 L^{-\omega} + \cdots\right)$$

$$\ln\left[s\left(\delta^*, L_2\right)\right] = \ln a_1 + \frac{1}{\nu}\ln L + \frac{1}{\nu}\ln\left(1 + \frac{\Delta L}{L}\right) + \ln\left(1 + \tilde{b}_1 L^{-\omega}\left(1 + \frac{\Delta L}{L}\right)^{-\omega} + \cdots\right)$$

Working with large L, both $\tilde{b}_1 L^{-\omega}$ and $\tilde{b}_1 L^{-\omega}\left(1 + \frac{\Delta L}{L}\right)^{-\omega}$ are small quantities, as well as $\frac{\Delta L}{L}$. If we Taylor expand the logarithms to the first order, we find that $f(x) = \ln(1 + x) \simeq x$.

$$\ln\left[s\left(\delta^*, L_2\right)\right] - \ln\left[s\left(\delta^*, L_1\right)\right] = \frac{1}{\nu}\ln\left(1 + \frac{\Delta L}{L}\right) + \tilde{b}_1 L^{-\omega}\left(1 - \omega\frac{\Delta L}{L}\right) - \tilde{b}_1 L^{-\omega}$$
$$= \frac{1}{\nu}\ln\left(1 + \frac{\Delta L}{L}\right) - \omega\tilde{b}_1 L^{-\omega}\frac{\Delta L}{L}$$

where we used Eq. (F.3) in the first step. Rearranging, we can obtain an estimate of the critical exponent $\nu \simeq \nu^*$ by neglecting the last term

$$\frac{1}{\nu^*(L)} = \frac{1}{\ln\left(1 + \frac{\Delta L}{L}\right)}\ln\left(\frac{s\left(\delta^*, L + \Delta L\right)}{s\left(\delta^*, L\right)}\right) \tag{F.9}$$

Appendix G

The modification of the model of Jensen et. al.

We want to modify the model of Jensen et. al. a bit to get an incommensurate-paramagnetic phase at 21.8 K. This process is two-fold. First, we must find how T_c scales with the couplings. Second, we must find a model who exhibits an incommensurate phase. Rescaling the couplings of this model would yield the desired modification of Jensen et. al.

G.1 The fit of T_c

The critical temperature should depend on the size of the couplings. Since the single-ion anisotropy is an on-site interaction, it should not affect the relative orientation of the spins too much (it just sets constraints on the direction of each spin separately). It is the couplings that order the system overall, so the phase transition should depend on J_{xy}, J_{yz} and J_y. The other couplings do not couple spins in the y-direction, which is the direction of the ordering. Since the nearest- and next-nearest neighbours are in competition, we set a minus sign between them, just as we argued in Chapter 8.1. Of course, if there are no couplings, there will be no ordering, and hence no phase transition. We therefore propose that

$$T_c = \alpha \left(2\left(J_{xy} + J_{yz}\right) - J_y\right)^p \tag{G.1}$$

where p is some real number. The factor of two in front of the nearest neigbour couplings reflects the fact that there are twice as many nearest neighbour bonds as next-nearest neighbour bonds in the fcc. Strictly speaking, this only applies to periodic boundary conditions, but this treatment is sort of rough anyway.

Figure (G.1) shows a few fits to the data of Chapter 8. Since it can be kind of hard to pick the best fit from a plot, we have included root mean squares for different p's in table (G.1). Out of the exponents we have tested, $p = 1.2$ yields the best fit. This agrees well with the visualization of figure (G.1).

Table G.1: The root mean squares of different fits to the data set. p is the exponent in the power law.

p	1.0	1.1	1.15	1.2	1.25	1.3	1.4
R.M.S.	0.393	0.237	0.178	0.155	0.183	0.245	0.406

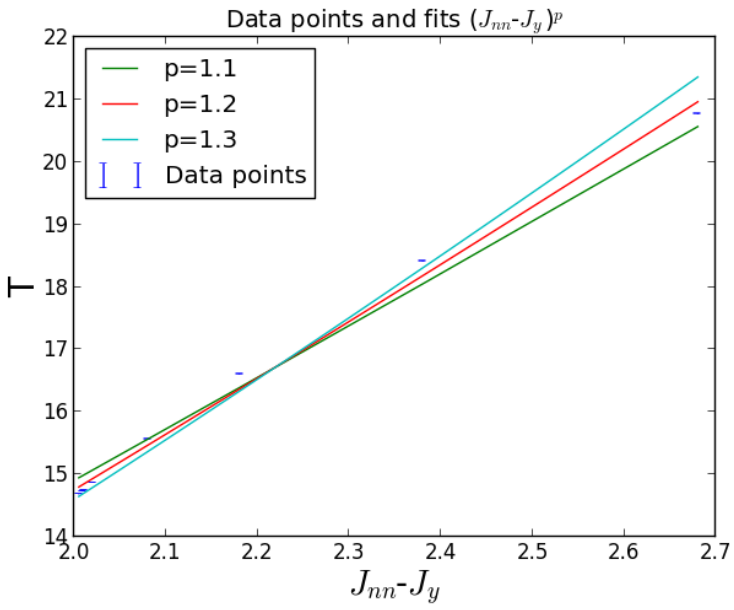

Figure G.1: Different fits $T^* = \left(2\left(J_{xy} + J_{yz}\right) - J_y\right)^p$ to the points found by the Binder cumulant crossings from $L = 12$ and $L = 14$. Jensen's model was used, but J_y was varied.

We argued that the crossing temperature T^* of L$=$ 12 and L$=$ 14 is close to the critical temperature T_c. The curve fit approach of table (7.3) gives $T_c = 14.7436 \pm 0.0017$, while $T^* = 14.7457 \pm 0.0014$ for T^*. These results are the same within their standard deviations, so $T^* \approx T_c$. We cannot textitguarantee that this holds for general J_y, but it was the best option we had with our limited time, and there is no obvious reason why it should not hold.

G.2 Modifying the couplings

So the critical temperature should depend on the couplings as roughly

$$T_c = \alpha \left(2\left(J_{xy} + J_{yz}\right) - J_y\right)^{1.2}$$

We know that for the couplings of Jensen et. al., $T_c = 14.7$ K, and use this together with the couplings to find that $\alpha \approx 0.34$ K$^{-0.2}$.

Considering the new couplings, $J_{xy} = 1.04$ meV,$J_{yz} = 0.3$ meV, $J_y = 0.74$ meV, we obtain a critical temperature of 14.3 K. To have the incommensurate-paramagnetic phase transition at 21.8 K, we need to multiply all the couplings with a factor η such that

$$T_c = \eta\alpha \left(2(J_{xy} + J_{yz}) - J_y\right)^{1.2} = 21.8 \text{ K}$$

which is realized when $\eta \approx 1.53$. The couplings for our modification to the Jensen et. al. model are then

$$J_{xy} = 0.46 \text{ meV}, \quad J_{yz} = 1.59 \text{ meV}, \quad J_y = 1.03 \text{ meV}$$

We will let the single-ion anisotropies remain as they are.

Appendix H

Technical details

H.1 Spherical coordinates and the spherical uniform distribution

We can express our spin components by spherical coordinates by

$$S_i^x = \sin\theta_i \cos\phi_i; \qquad S_i^y = \sin\theta_i \sin\phi_i; \qquad S_i^z = \cos\theta_i \tag{H.1}$$

Since the spins are normalized, we only need two variables to set the three-component spins.

We want every spin orientation to be equally likely, meaning that we want to draw our random spins from a spherical uniform distribution. We should not be more likely to draw spins from some specific area of the unit sphere; all areas of equal size should be equally likely. Naively, we might think picking two angles $\theta \in [0, \pi]$ and $\phi \in [0, 2\pi]$ from a random uniform distribution would realize that. However, the area element of the unit sphere, or the solid angle, is a function of θ: $d\Omega = \sin\theta d\theta d\phi$. This will skew the distribution if θ is drawn uniformly. Obviously, we must pick some other variables and relate them to the angles somehow. We rewrite the solid angle and obtain

$$d\Omega = -d\cos\theta d\phi; \qquad \cos\theta \in [-1, 1], \;\; \phi \in [0, 2\pi]$$

So it is the variables $\cos\theta$ and ϕ that should be drawn uniformly. Our random number generator of choice gives floating point numbers in the interval $[0, 1]$, so if we draw two numbers u and v, the angles can be found by

$$\theta = \arccos(1 - 2u); \quad \phi = 2\pi v$$

The former follows as $1 - 2u$ is uniform on the interval $[-1, 1]$, just as we require $\cos\theta$ to be.

The spin components are found by insertion of these angles into Eq. (H.1).

H.2 Finding the (0,K,0) line

The interesting properties of $LiNiPO_4$ occur in the y-direction, so we want a way to extract $\mathbf{q} = \frac{2\pi}{a}(0, K, 0)$.

Finding the $\mathbf{q}$-vectors is straightforward using Eq.s (2.36) to (2.38). Extracting the (0,K,0)-line is then readily achieved by applying an if-test on the x- and z-components of the $\mathbf{q}$s. Though not the most elegant solution to our problem, this approach is fast and simple.

A The FFTW (The Fastest Fourier Transform in the West)

FFTW, or "The Fastest Fourier Transform in the West" (FFTW) was created by Matteo Frigo and Steven G. Johnson. To obtain the results needed for the spin correlation function, a multi-dimensional transform were computed by FFTW for the two- and three-dimensional lattices. In such cases, FFTW computes the one-dimensional transform along each dimension of the array, and takes the separable product. The one-dimensional product takes input array X and computes the forward transform Y in the following manner[9]:

$$Y_k = \sum_{j=0}^{N-1} X_j e^{-2\pi jki/N} \tag{H.2}$$

where $i = \sqrt{-1}$ as usual. Y is periodic, meaning that $Y_N = Y_0$. Furthermore, the symmetry $Y_k = Y^*_{N-k}$ leaves half the output redundant. The output array is therefore shortened to the first $n/2 + 1$ elements of Y, i.e. elements $0, \cdots n/2$. $n/2$ is here rounded down. To compensate for the short length of the output array, the returned data will have to be patched together. To recap, what we expect the following from the forward Fourier transform executed by FFTW:

1. $\tilde{S}^z_0$ is purely real
2. If N is even, $\tilde{S}^z_{N/2}$ is purely real as well
3. $\tilde{S}^z_k$=$(\tilde{S}^z_{N-k})^*$

One thing to be aware of is that the transforms are unnormalized. If we use FFTW to do the transforms $X \to Y \to X$, the final result will be multiplied by N, the number of elements in the input array[9].

The Fourier transform as used by FFTW

The three-dimensional version of Eq. (H.2) is

$$F_n = \frac{1}{N} \sum_{k=0}^{L_1-1} \sum_{l=0}^{L_2-1} \sum_{m=0}^{L_3-1} f_k e^{-\frac{2\pi ink}{L_1} - \frac{2\pi inl}{L_2} - \frac{2\pi inm}{L_3}} \tag{H.3}$$

where F_n is the Fourier transform, N is the number of discrete data points and f_k is the real space values, which will be the spins in our implementation. The above expression is optimal when feeding to a FFTW.

To see that Eq. (2.39) fits with Eq. (H.3), we recall Eq. (2.32)

$$\mathbf{q} = \frac{k_1}{L_1}\mathbf{b}_1 + \frac{k_2}{L_2}\mathbf{b}_2 + \frac{k_3}{L_3}\mathbf{b}_3$$

We can now write $\mathbf{q}\cdot\mathbf{r} = 2\pi\left(\frac{k_1 n_1}{L_1} + \frac{k_2 n_2}{L_2} + \frac{k_3 n_3}{L_3}\right)$ using Eq. (2.29), getting (2.39) on the multidimensional form of (H.3):

$$S^\alpha_{\mathbf{q}} = \sum_{\mathbf{r}} S^\alpha_{\mathbf{r}} e^{-2\pi i\left(\frac{k_1 n_1}{L_1} + \frac{k_2 n_2}{L_2} + \frac{k_3 n_3}{L_3}\right)}$$

$$S^\alpha_{\mathbf{q}} = \sum_{n_1}^{L_1-1}\sum_{n_2}^{L_2-1}\sum_{n_3}^{L_3-1} S^\alpha_{n_1,n_2,n_3} e^{-2\pi i\left(\frac{k_1 n_1}{L_1} + \frac{k_2 n_2}{L_2} + \frac{k_3 n_3}{L_3}\right)} \tag{H.4}$$

with $n_j, i_j \in [0, L_j - 1]$.

H.3 Indices

When doing simulations on multidimensional systems we often have d indices, with d being the dimensionality of the lattice. A three-dimensional system will then have three indices, usually denoted by i, j, k. An alternative to this is having one index that traverses the lattice. To take an easy example, the simple cubic lattice will then be traversed row by row for each layer of the system. Computationally, this is more effective than using d indices [17]. However, peculiarities concerning the periodic boundary conditions forced us to convert back to three indices i, j, k to find the neighbours, but hopefully, some computation time is saved nonetheless. Regardless, the code is more readable as we only need one loop over indices and not three.

The lattice is traversed in row-major ordering to match the output of FFTW.

A The modulo operator

The modulo operator % gives the remainder of an integer division. Mathematically, with the backslash $\backslash$ denoting integer division, it can be formulated as

$$x\%y = x - (x\backslash y)\cdot y \tag{H.5}$$

B Two dimensions

In the two-dimensional case and for a $L_1 \times L_2$ lattice, the indices n and i, j will be related by:

$$i = n\backslash L_2; \;\; j = n\%L_2 \tag{H.6}$$

Table H.1: The change in indices from **b** to each neighbour.

	Δi	Δj	Δk
$\pm\mathbf{a}_1$	± 1	0	0
$\pm\mathbf{a}_2$	0	± 1	0
$\pm\mathbf{a}_3$	0	0	± 1
$\pm\mathbf{a}_4$	± 1	∓ 1	0
$\pm\mathbf{a}_5$	0	± 1	∓ 1
$\pm\mathbf{a}_6$	± 1	0	∓ 1

this can easily be verified by drawing and comparing.

C Three dimensions

Using the same notation as above, the standard indices i, j, k of a $L_1 \times L_2 \times L_3$ lattice can be found by:

$$i = n \backslash (L_2 \cdot L_3); \quad j = n \backslash L_3 - n \backslash (L_2 \cdot L_3) \cdot L_2; \quad k = n \% L_3 \tag{H.7}$$

For a primitive cubic lattice, these indices will be in the x, y, z-directions, respectively, while for the face-centered cubic lattice, they will be in the direction of the primitive vectors $\mathbf{a}_1$, $\mathbf{a}_2$, $\mathbf{a}_3$ given by Eq. (2.33). The position can then be found by Eq. (2.26).

For the three-dimensional lattices, we have the relation

$$n = iL_2L_3 + jL_3 + k \tag{H.8}$$

converting from standard indices i, j, k to the one running index n.

D How to find the neighbours of a site

If we operate with one running index, we need to use (H.7) to find the i, j, k-indices of our site. When that is done, we consider the neighbours $\mathbf{b} \pm \mathbf{a}_1$, $\mathbf{b} \pm \mathbf{a}_2$, $\mathbf{b} \pm \mathbf{a}_3$, $\mathbf{b} \pm \mathbf{a}_4$, $\mathbf{b} \pm \mathbf{a}_5$, $\mathbf{b} \pm \mathbf{a}_6$, where

$$\mathbf{a}_4 = \mathbf{a}_1 - \mathbf{a}_2$$
$$\mathbf{a}_5 = \mathbf{a}_2 - \mathbf{a}_3$$
$$\mathbf{a}_6 = \mathbf{a}_3 - \mathbf{a}_1$$

and $\mathbf{a}_1$, $\mathbf{a}_2$ and $\mathbf{a}_3$ are defined by Eq. (2.33). Using this notation, it is easy to see how the indices i, j, k changes from **b** to each neighbour, as listed in table (H.1).

To convert back to the running index, we use Eq. (H.8). Referring back to table (H.1) and enforcing periodic boundary conditions in $\mathbf{a}_1$, $\mathbf{a}_2$ and $\mathbf{a}_3$, we obtain the formula for the neighbour n_{nb} of n

$$n_{nb} = \Big((L_1 + i + \Delta i)\%L_1\Big)L_2L_3 + \Big((L_2 + j + \Delta j)\%L_2\Big)L_3 + (L_3 + k + \Delta k)\%L_3 \tag{H.9}$$

Patching the spin correlation function

Due to the symmetry of the problem, FFTW returns an array of half the size of the input array when doing the real to complex Fourier transform, as seen in list (3). As a consequence, the last index will be of size $L_D \backslash 2 + 1$, where L_D is the size of the last dimension in the input data. Thus, sites with $i_D > L_D - (L_D \backslash 2 + 1)$ will be omitted. Considering the symmetries in list (3), we can still access the value by finding the location of its complex conjugate. For the 3D case, compensating from the omitted terms by replacing $L_D \to L_D \backslash 2 + 1$, we find it at index

$$n = L_2(L_3 \backslash 2 + 1)(L_1 - n_1)\%L_1 + (L_3 \backslash 2 + 1)(L_2 - n_2)\%L_2 + (L_3 - n_3)\%L_3 \quad \text{(H.10)}$$

where n_1, n_2 and n_3 are the indices in the $\mathbf{b}_1$, $\mathbf{b}_2$ and $\mathbf{b}_3$-directions, respectively. Since we are only interested in the absolute value of $\tilde{S}_n$, there is no need to take the complex conjugate.

The 2D case is even simpler

$$n = (L2 \backslash 2 + 1) * ((L1 - n1)\%L1) + (L2 - n2)\%L2 \quad \text{(H.11)}$$

Appendix I

Code listings

This sections lists important parts of the code. The entire code is available at
https://github.com/KineOdegardHanssen/Master
Repetitive commands, like declaring or resetting a lot of different variables, are not written out in full.

I.1 One lattice sweep

```
void MonteCarlo::mcstepf_metropolis(double beta)
{
    double changes = 0;
    for(int n=0; n<N; n++)
    {
        int k = distribution_n(generator_n);    // Draw a random site

        double sx = mylattice.sites[k].spinx;
        double sy = mylattice.sites[k].spiny;
        double sz = mylattice.sites[k].spinz;

        // Drawing random spins
        double u = ran2(&seed1);
        double v = ran2(&seed1);

        double theta = acos(1.0-2.0*u);
        double phi = 2.0*M_PI*v;

        double sintheta = sin(theta);
        double sx_t = sintheta*cos(phi);
        double sy_t = sintheta*sin(phi);
        double sz_t = cos(theta);

        // Energy contribution after spin change
```

```
double energy_diff = 0; // Resetting the energy difference
    for every n
if(sianisotropy)
{
    double Dix = mylattice.Dix;
    double Diy = mylattice.Diy;
    double Diz = mylattice.Diz;
    energy_diff += (Dix*(sx_t*sx_t -sx*sx) +
        Diy*(sy_t*sy_t-sy*sy)+ Diz*(sz_t*sz_t -sz*sz));
}
if(magfield)
{
    double hx = mylattice.hx;
    double hy = mylattice.hy;
    double hz = mylattice.hz;
    energy_diff += hx*(sx-sx_t) + hy*(sy-sy_t) + hz*(sz-sz_t);
}
if(isotropic)
{
    double partnerspinx = 0;
    double partnerspiny = 0;
    double partnerspinz = 0;

    // Determining the number of neighbours
    int nneighbours;
    if(notperiodic)    nneighbours =
        mylattice.sites[k].no_of_neighbours_site;
    else               nneighbours = no_of_neighbours;

    for(int j=0; j<nneighbours; j++) // nneighbours
        forskjellig fra E til Y
    {
        // Picking out the neighbour
        int l = mylattice.sites[k].bonds[j].siteindex2;

        // Picking out the J each time (may vary depending on
            bond type)
        double J = mylattice.sites[k].bonds[j].J;

        if(J!=0)
        {
            double sxk = mylattice.sites[l].spinx;  // The
                neighbours do not change
            double syk = mylattice.sites[l].spiny;
            double szk = mylattice.sites[l].spinz;
            partnerspinx += J*sxk;
            partnerspiny += J*syk;
            partnerspinz += J*szk;
        }
    }
```

```
            energy_diff += partnerspinx*(sx_t-sx) +
                partnerspiny*(sy_t-sy) + partnerspinz*(sz_t-sz);
        }
        if(dm)
        {
            // Determining the number of neighbours
            double detsign;
            int nneighbours;
            if(notperiodic)    nneighbours =
                mylattice.sites[k].no_of_neighbours_site;
            else               nneighbours = no_of_neighbours;
            for(int j=0; j<nneighbours; j++)
            {
                int l = mylattice.sites[k].bonds[j].siteindex2;
                bool increasing =
                    mylattice.sites[k].bonds[j].increasing;
                if(increasing)          detsign = 1.0;
                else                    detsign = -1.0;

                double Dx = mylattice.Dx;
                double Dy = mylattice.Dy;
                double Dz = mylattice.Dz;

                if(dmdiffdirs)
                {
                    if(mylattice.sites[k].bonds[j].direction!="yz")
                    {
                        Dx = 0; Dy = 0; Dz = 0;
                    }
                }

                double sxk = mylattice.sites[l].spinx;
                double syk = mylattice.sites[l].spiny;
                double szk = mylattice.sites[l].spinz;

                energy_diff +=
                    detsign*(Dx*((sy_t-sy)*szk-syk*(sz_t-sz))
                +Dy*((sz_t-sz)*sxk-szk*(sx_t-sx))
                +Dz*((sx_t-sx)*syk-(sy_t-sy)*sxk));
            }
        }
        if(nextnearest)
        {
            double partnerspinx = 0;
            double partnerspiny = 0;
            double partnerspinz = 0;

            // Different for diferent lattices, but we include one
                here
            if(type_lattice=='Y')
            {
```

```
            double Jy = mylattice.sites[k].nextnearesty[0].J;
            double Jz = mylattice.sites[k].nextnearestz[0].J;

            double nnyspinx, nnyspiny, nnyspinz;
            double nnzspinx, nnzspiny, nnzspinz;
            int nneighbours =
                mylattice.sites[k].no_of_nneighbours_site;
            for(int i=0; i<nneighbours; i++) // Having
                contributions in the + and - directions, open BC
            {
                int yneigh =
                    mylattice.sites[k].nextnearesty[i].siteindex2;

                // Spin components of next nearest neighbours in
                    the y-direction
                nnyspinx = mylattice.sites[yneigh].spinx;
                nnyspiny = mylattice.sites[yneigh].spiny;
                nnyspinz = mylattice.sites[yneigh].spinz;

                partnerspinx += Jy*nnyspinx;
                partnerspiny += Jy*nnyspiny;
                partnerspinz += Jy*nnyspinz;
            }
            for(int i=0; i<2; i++) // Having contributions in the
                + and - directions
            {
                int zneigh =
                    mylattice.sites[k].nextnearestz[i].siteindex2;

                // Spin components of next nearest neighbours in
                    the z-direction
                nnzspinx = mylattice.sites[zneigh].spinx;
                nnzspiny = mylattice.sites[zneigh].spiny;
                nnzspinz = mylattice.sites[zneigh].spinz;

                partnerspinx += Jz*nnzspinx;
                partnerspiny += Jz*nnzspiny;
                partnerspinz += Jz*nnzspinz;
            }
            energy_diff += (sx_t-sx)*partnerspinx +
                (sy_t-sy)*partnerspiny + (sz_t-sz)*partnerspinz;
        }
    }

    double energy_new = energy_old + energy_diff;

    // Updating the energy and the state according to Metropolis
    if(energy_new <= energy_old)
    {
        // Updating the spin
        mylattice.sites[k].spinx = sx_t;
```

```
                mylattice.sites[k].spiny = sy_t;
                mylattice.sites[k].spinz = sz_t;

                // Updating the energy
                energy_old = energy_new;

                // Updating changes to get the acceptance rate
                changes+=1;
            }
            else
            {
                double prob = exp(-beta*(energy_diff));
                double drawn = distribution_prob(generator_prob);
                if(drawn<prob)
                {
                    // Updating the spin
                    mylattice.sites[k].spinx = sx_t;
                    mylattice.sites[k].spiny = sy_t;
                    mylattice.sites[k].spinz = sz_t;

                    // Updating the energy
                    energy_old = energy_new;

                    // Updating changes to get the acceptance rate
                    changes+=1;
                }
            }
        } // End loop over n. Lattice sweep done
        acceptancerate = changes/N;
}
```

I.2 Retrieving the variables

```
void MonteCarlo::runmetropolis(double beta)
{
    // Initializing the energy
    initialize_energy();

    // Equilibration steps
    // Added option of cooling the system gradually
    double eqbeta = beta;
    bool slowcool = true;
    if(beta<0.01)    slowcool = false; // Should not increase the
       temperature
    double deltabeta = (beta-0.01)/(int(eqsteps/2)-1);
    double starttime = clock();
    for(int i=0; i<eqsteps; i++)
```

```
{
    if(slowcool)
    {
        if(i<int(eqsteps/2))    eqbeta = 0.01+deltabeta*i;
        else                    eqbeta = beta; // As a safeguard
    }
    mcstepf_metropolis(eqbeta);
}

// Setting arrays for measurable quantities
std::vector<double> acceptancerates    =
   std::vector<double>(no_of_bins);
std::vector<double> energies = std::vector<double>(no_of_bins);
// Etc.

// For the correlation function
// The spins
std::vector<double> spins_in_x = std::vector<double>(N);
std::vector<double> spins_in_y = std::vector<double>(N);
std::vector<double> spins_in_z = std::vector<double>(N);
// Declare qconf and set the plan
vector< complex<double> > qconfx(N);  // Output array
vector< complex<double> > qconfy(N);  // Output array
vector< complex<double> > qconfz(N);  // Output array
givexplanforFFT(spins_in_x, qconfx);
giveyplanforFFT(spins_in_y, qconfy);
givezplanforFFT(spins_in_z, qconfz);

// Array for the results
// Determining the length of the array
int dim = mylattice.dim;
int qlimit = 1; // To be multiplied;
for(int l=0; l<(dim-1); l++)
{    // Looping over all dimensions but the last
    qlimit *= mylattice.dimlengths[l];
}
qlimit *= mylattice.dimlengths[dim-1]/2+1;

// declaring arrays for fftw

// Resetting quantities
double ar_av        = 0;
double energy_av    = 0;
double energy_sq_av = 0;
// etc.

for(int i=0; i<no_of_bins; i++)  // Loop over the bins
{   // For every bin

    // Reset quantities
    energies[i]    = 0;
```

```
        energies_sq[i] = 0;
        // etc

        // Resetting the correlation function bin average for every
           bin
        for(int k=0; k<N; k++) correlation_functionx_av_bin[k] = 0;
        // etc

        for(int j=0; j<mcsteps_inbin; j++)    // Loop over number of
           sweeps in bin
        {   // For each sweep in bin

            mcstepf_metropolis(beta);

            // acceptancerate
            acceptancerates[i] += acceptancerate;
            ar_av += acceptancerate;
            // energy
            energies[i]    += energy_old;    // Storing to get the
               standard deviation
            energies_sq[i] += energy_old*energy_old;

            // declare
            double mx = 0;
            double my = 0;
            // etc.

            for(int k=0; k<N; k++)
            {
                mx+= mylattice.sites[k].spinx;
                my+= mylattice.sites[k].spiny;
                mz+= mylattice.sites[k].spinz;
                // For the correlation function
                if(calculatespincorrelationfunction)
                {
                    spins_in_x[k] = mylattice.sites[k].spinx;
                    spins_in_y[k] = mylattice.sites[k].spiny;
                    spins_in_z[k] = mylattice.sites[k].spinz;
                }
            }
            // Gathering
            mx = mx/N;
            mx_abs = abs(mx);
            mxsq = mx*mx;
            mxquad = mxsq*mxsq;
            // etc.

            // Add to average
            mx_av += mx;
            // etc
```

```
            // Store for each bin to find std.dev.
            mxs[i] += mx;
            // etc.

            // Possibly find m(q). Call another function to do that

            // FFT steps
            if(calculatespincorrelationfunction)
            {
                fftw_execute(px);
                // Do this for py and pz tool

                // Looping over particles
                // for(...){
                    // Get right index. Depends on dim
                    cx =
                        (qconfx[index]*conj(qconfx[index])).real()/(N*N);
                    // and cy and cz
                    correlation_functionx_av_bin[n] += cx;
                    // and cy and cz
                //}
            }
         }        // Done
        // Find average
        mxs[i] = mxs[i]/mcsteps_inbin;
        // etc.
    }
    energy_av = 0; // May choose to set this here. Then I need to
        prefix with double

    // Average energy // Don't want overflow
    for(int I=0; I<no_of_bins; I++)    energy_av += energies[I];
    energy_av = energy_av/no_of_bins;
    // etc
    // Std.dev. in the energy //
    double E_stdv = 0;
    for(int I=0; I<no_of_bins; I++)    E_stdv +=
        (energies[I]-energy_av)*(energies[I]-energy_av);
    E_stdv = sqrt(E_stdv/(no_of_bins*(no_of_bins-1)));
    // etc.
    // Print to file
}
```

I.3 The Bootstrap procedure

This analysis was done in python. This is the code segment that applies the Bootstrap method to find the peak of the magnetic susceptibility. The procedure will be a bit different when applied to finding the crossing-points of the Binder cumulant graphs

```
def max_temp(LA, filenameA, quadraticnotcubicfit, toplotornot,
    usegaussian, cutit, cutlower, cutupper): # Extract the beta
    value of the crossing between two graphs
  N = LA*LA*LA
  infileA = open(filenameA, "r")
  # Getting lists ready to store the data

  # Sorting arrays
  betasA                = []          # List of beta values
  binofbeta_firstindexA = []          #
  binofbeta_lastindexA  = []          #

  # Other quantities
  mzssqc_bavsA      = []          # Index 14
  mzsquadc_bavsA    = []          # Index 15
  # Etc.

  # Read the rest of the lines
  lines = infileA.readlines()

  i = 0 # Counter to get the indices right
  betabefore = 0 # Test the betas so we can gather the bins.
  binofbeta_firstindexA.append(0)

  # Getting data from the file
  for line in lines:
      words = line.split()
      if len(words) != 0:
          # Betas
          beta = float(words[0])
          if beta != betabefore:
              betasA.append(beta)
              betabefore = beta
              if i != 0:
                  binofbeta_firstindexA.append(i)
                  binofbeta_lastindexA.append(i-1)
          en = float(words[14])
          mzssqc_bavsA.append(en)          # Index 14
          # <m^4_z(q)>
          en = float(words[15])
          mzsquadc_bavsA.append(en)        # Index 15
          # etc.
      i += 1 # Increasing the counter

  binofbeta_lastindexA.append(i-1)  # The index has been updated
     one time too many

  # Remember to close the file
  infileA.close()
```

```
nbinsA = zeros(len(betasA))
for i in range(0,len(betasA)):
    nbinsA[i] = binofbeta_lastindexA[i]-binofbeta_firstindexA[i]+1

no_of_bins_each_betaA = binofbeta_lastindexA[0]+1
no_of_betasA          = len(betasA)               # The number of
   different temperatures
no_of_BootstraprunsA  = 300

betasA = array(betasA)

if cutit==1:   # If we have simulations for a larger temperature
   interval than we wish
    # ... details

if toplotornot==0: # May want to look at the graphs underway
    plotter = 1
else:
    plotter = 0
warning = 0
betaatmax_av = 0
betas_at_max = zeros(no_of_BootstraprunsA)
maxtemp_av = 0
maxtemps = zeros(no_of_BootstraprunsA)
tempatmax_K_av = 0
temp_at_max = zeros(no_of_BootstraprunsA)
for k in range(0, no_of_BootstraprunsA): # Want to repeat the
   random selection of bins a number of times
    magnsuscsx = []; magnsuscsy = []; magnsuscsz = []
    heatcaps = []
    for i in range(0, no_of_betasA): # For doing it for every
       temperature
        nbins = int(nbinsA[i])
        ### Reset all quantities I want to find by bootstrap
        mx = 0; mxabs = 0; mx2 = 0; mx4 = 0; my = 0; myabs = 0;
           my2 = 0; my4 = 0; mz = 0; mzabs = 0; mz2 = 0; mz4 = 0;
        eav = 0; esqav = 0; hcav = 0;
        for j in range(0, nbins): # For finding the averages
            ###Draw a random integer in
                [binofbeta_firstindexA[i],
                binofbeta_lastindexA[i]].
            n = randint(binofbeta_firstindexA[i],
                binofbeta_lastindexA[i])  # Draw a random number n
                times
            ###Extract O(n), add to average function
            mz += mzsc_bavsA[n]; mzabs += mzsc_abs_bavsA[n]; mz2
               += mzssqc_bavsA[n]; mz4 += mzsquadc_bavsA[n];
            # etc.
        ### Divide the average of O(n) by no_of_bins_each_beta to
           ACTUALLY make the average
        mz = mz/nbins; mzabs = mzabs/nbins; mz2 = mz2/nbins; mz4
```

```
                = mz4/nbins;
            # etc.
            ### Magnetic susceptibility per spin
            magnsuscz_this = betasA[i]*(mz2-(mzabs*mzabs))*N
            ### Total heat capacity
            heatcap_this = betasA[i]**2*(esqav-(eav*eav))/N
            ### Feed into lists
            magnsuscsz.append(magnsuscz_this)
            heatcaps.append(heatcap_this)
        ### Do a fitting of the results.
        if quadraticnotcubicfit==0:
            magnsuscsz = array(magnsuscsz)
            fitvectorzcompA = polyfit(betasA, magnsuscsz, 1) # Fits
                the function points to a quadratic polynomial
            azA = fitvectorzcompA[0]; bzA = fitvectorzcompA[1];

            nfbetas = 1000
            fbetas = linspace(betasA[0], betasA[len(betasA)-1],
                nfbetas)

            fA = giveline(azA, bzA, fbetas)
        # etc.

        betaatmax, maxtemp = findmaxima(fbetas, fA, warning)
        betaatmax_av += betaatmax
        betas_at_max[k] = betaatmax
        maxtemp_av += maxtemp
        maxtemps[k] = maxtemp
        tmK = converttemp(betaatmax)
        tempatmax_K_av += tmK
        temp_at_max[k] = tmK
        if warning<3:
            warning += 1

        if plotter==0:
            # Plot a few times if I want to.

    betaatmax_av = betaatmax_av/no_of_BootstraprunsA
    betaatmax_stddev = 0
    for i in range(0, no_of_BootstraprunsA):
        betaatmax_stddev +=
            (betaatmax_av-betas_at_max[i])*(betaatmax_av-betas_at_max[i])
    betaatmax_stddev = sqrt(betaatmax_stddev/(no_of_BootstraprunsA-1))
    # Etc.

    return betaatmax_av, betaatmax_stddev, maxtemp_av,
        maxtemp_stddev, tempatmax_K_av, tempatmax_K_stddev
```

Bibliography

[1] F. A. Kassan-Ogly A. K. Murtazaev, M. K. Ramazanov and D. R. Kurbanova. Phase transitions in the antiferromagnetic Ising model on a body-centered cubic lattice with interactions between next-to-nearest neighbors. *Journal of Experimental and Theoretical Physics*, 120(1):110–114, 6 2015.

[2] N. G. Fytas A. Malakis and G. Gülpinar. Critical Binder Cumulant and universailty: Fortuin-Kasteleyn clusters and order-parameter fluctuations. *Physical Review E*, 89(4):623–628, 4 2014. DOI: 10.1103/PhysRevE.89.042103.

[3] P. Bak. Commensurate phases, incommensurate phases and the devil's staircase. *Reports on Progress in Physics*, 45(20):43, 5 1982. http://stacks.iop.org/0034-4885/45/i=6/a=001.

[4] K. Binder. Finite size scaling analysis of Ising model Block distribution funcitons. *Zeitschrift für Physik B - Condensed Matter*, 43(2):119–140, 6 1981. DOI: https://doi.org/10.1007/BF01293604.

[5] K. Binder and D.W. Heermann. *Monte Carlo Simulation in Statistical Physics: An Introduction*. Springer-Verlag, Berlin, 2 edition, 1992.

[6] P. W. Chaikin and T. C. Lubensky. *Principles of Condensed Matter Physics*. Cambridge University Press, Cambridge, 5 edition, 2010.

[7] J.-P. Rivera D. Vaknin, J. L. Zarestky and H. Schmid. Commensurate-incommensurate magnetic phase transition in magnetoelectric single crystal $LiNiPO_4$. *Physical Review Letters*, 92(20):739–744, 5 2004. DOI: 10.1103/PhysRevLett.92.207201.

[8] E. Fogh. Unpublished note. .

[9] M. Frigo. FFTW, October 2017. FFTW Manual, version 3.3.7 http://www.fftw.org/fftw3_doc/The-1d-Real_002ddata-DFT.html#The-1d-Real_002ddata-DFT.

[10] W. Guo H. Shao and A. W. Sandvik. Supplementary materials for Quantum criticality with two length scales. *Science*, Mar 2013. http://science.sciencemag.org/content/suppl/2016/03/16/science.aad5007.DC1.

[11] P. C. Hemmer. *Faste Stoffers Fysikk*. Tapir forlag, Trondheim, 1 edition, 1987.

[12] T. B. S. Jensen. *Magnetic Structures, Phase Diagram and Spin Waves of Magneto-electric $LiNiPO_4$*. PhD thesis, Technical University of Denmark, 2007. Corrected version, July 2008.

[13] T. B. S. Jensen, N. B. Christensen, M. Kenzelmann, H. M. Rønnow, C. Niedermayer, N. H. Andersen, K. Lefmann, M. Jiménez-Ruiz, F. Demmel, J. Li, J. L. Zarestky, and D. Vaknin. Anomalous spin waves and the commensurate-incommensurate magnetic phase transition in $LiNiPO_4$. *Physical Review B*, 79:092413, Mar 2009.

[14] D. P. Landau and K. Binder. *A guide to Monte Carlo Simulations in Statistical Physics*. Cambridge University Press, Cambridge, 4 edition, 2015.

[15] J. Li, T. B. S. Jensen, N. H. Andersen, J. L. Zarestky, R. W. McCallum, J.-H. Chung, J. W. Lynn, and D. Vaknin. Tweaking the spin-wave dispersion and suppressing the incommensurate phase in $LiNiPO_4$ by iron substitution. *Phys. Rev. B*, 79:174435, May 2009. DOI: 10.1103/PhysRevB.79.174435.

[16] T. Nagamiya. Helical spin ordering-1 theory of helical spin configurations. In D. Turnbull F. Seitz and H. Ehrenreich, editors, *Solid State Physics - Advances in Research and Applications*, volume 20 of *5*, chapter 5, pages 306–411. Academic Press Inc., New York, 1 edition, 1967.

[17] M.E.J. Newman and G.T. Barkema. *Monte Carlo Methods in Statistical Physics*. Oxford University Press, Oxford, 1999.

[18] F. Ravndal and E. G. Flekköy. Statistical physics - a second course, Jan 2014. Lecture notes, available at http://www.uio.no/studier/emner/matnat/fys/FYS4130/v16/pensumliste/index.html.

[19] Wolfram Research. Modified bessel function of the first kind: Differentiation, March 2017. From MathWorld–A Wolfram Web Resource http://functions.wolfram.com/Bessel-TypeFunctions/BesselI/20/01/02/.

[20] D. V. Schroeder. *An Introduction to Thermal Physics*. Addison Wesley Longman, 4 edition, 2000.

[21] W. Selke. Spatially modulated structures in systems with competing interactions. In C. Domb and J. L. Lebowitz, editors, *Phase Transitions and Critical Phenomena*, volume 15, chapter 1, pages 2–72. Academic Press Inc., New York, 1 edition, 1992.

[22] W. Selke and L. N. Schur. Critical Binder Cumulant in two-dimensional anisotropic Ising models. *Journal of Physics A: Mathematical and General*, 38(44):739–744, 10 2005. DOI: 10.1088/0305-4470/38/44/L03.

[23] W. Selke and L. N. Schur. Critical Binder Cumulant in a two-dimensional anisotropic Ising model with competing interactions. *Physical Review E*, 80(4):119–140, 10 2009. DOI: 10.1103/PhysRevE.80.042104.

[24] G. L. Squires. *Practical Physics*. Cambridge University Press, Cambridge, 4 edition, 2001.

[25] R. Toft-Petersen, J. Jensen, T. B. S. Jensen, N. H. Andersen, N. B. Christensen, C. Niedermayer, M. Kenzelmann, M. Skoulatos, M. D. Le, K. Lefmann, S. R. Hansen, J. Li, J. L. Zarestky, and D. Vaknin. High-field magnetic phase transitions and spin excitations in magnetoelectric $LiNiPO_4$. *Physical Review B*, 84:054408, Aug 2011.

[26] R. Toft-Petersen, M. Reehuis, T. B. S. Jensen, N. H. Andersen, J. Li, M. D. Le, M. Laver, C. Niedermayer, B. Klemke, K. Lefmann, and D. Vaknin. Anomalous magnetic structure and spin dynamics in magnetoelectric $LiFePO_4$. *Phys. Rev. B*, 92:024404, Jul 2015. DOI: 10.1103/PhysRevB.92.024404.

[27] Roser Valentí. Phase transitions, Nov 2013. Lecture notes, available at https://itp.uni-frankfurt.de/~valenti/WS13-14/all_1314_chap6.pdf.

[28] E. W. Weisstein. Modified bessel function of the first kind., March 2017. From MathWorld–A Wolfram Web Resource http://mathworld.wolfram.com/ModifiedBesselFunctionoftheFirstKind.html.

[29] E. W. Weisstein. Trigonometry angles–pi/5., May 2017. From MathWorld–A Wolfram Web Resource http://mathworld.wolfram.com/TrigonometryAnglesPi5.html. Read 10.05.17.